Mahdi Darab

Dispersion, Performance and Durability of Pt Nanoparticles on Carbon for PEM Fuel Cell Catalysis

Thesis for the degree of Philosophiae Doctor

Trondheim, October 2014

Norwegian University of Science and Technology
Faculty of Natural Sciences and Technology
Department of Materials Science and Engineering

NTNU – Trondheim
Norwegian University of
Science and Technology

NTNU
Norwegian University of Science and Technology

Thesis for the degree of Philosophiae Doctor

Faculty of Natural Sciences and Technology
Department of Materials Science and Engineering

© Mahdi Darab

ISBN 978-82-326-0508-8 (printed ver.)
ISBN 978-82-326-0509-5 (electronic ver.)
ISSN 1503-8181

Doctoral theses at NTNU, 2014:298
IMT-Report 2014:212

Printed by NTNU-trykk

به نام آنکه ستایش را سزد

ای عزیز

چگونه می‌توان نعمتت را سپاس گفت آنگاه که ما را همقدم کاروان مشتاقانی قرار دادی که در میان انبوه سؤال‌ها و چراها به دنبال نیم‌نگاهی از کمال کبریایی تو می‌گردند و آتش اشتیاق به دانستن و سوز نیاز به شناختن تو را با اشک قلم فرو می‌نشانند.

و تو

آنقدر بزرگی که بر هر بضاعت اندک که از وجود بنده‌ای ناچیز به سوی تو جهت می‌گیرد، نظر می‌کنی و ما حیرت‌زده عظمت تو و شرمسار کوچکی گامهایمان، قدم در راهی نهاده‌ایم که آرزو داریم در هر منزلش حجم حضورت را احساس کنیم. چرا که تو آن غایت بی‌نهایتی که از رگ گردن نزدیکتر است و هر زمان دست یافتنی‌تر می‌نماید.

بی‌نهایت نزدیک

حرکت ما را بپذیر و آنچنان کن که نظر لطف آن عزیزی که گیتی، قائم به وجود اوست، بدرقه راهمان باشد و همراهی مرکبش، نقطه اوج سفرمان؛ که اگر آنچه می‌کاویم و می‌آموزیم با تأیید آسمانیش متبرک نگردد، پرسه‌زدنی است بی‌حاصل و ما به تو پناه می‌بریم از بی‌حاصلی و بیهودگی.

Sammendrag

Hovedformålet i dette PhD arbeidet har vært å utvikle en forståelse av hvilken effekt fordelingen av platinapartikler på en karbonbærer har på den generelle aktiviteten og holdbarheten til disse elektrokatalysatorene. For å kunne studere dette nærmere og få en forståelse av en eventuell effekt ble det utført en omfattende in-situ og ex-situ testing av disse elektrokatalysatorene, framstilt med kontrollert varierende struktur.
Det første trinnet bestod i å syntetisere en Pt elektrokatalysator med ønsket strukturelle, og dermed også elektrokjemiske, egenskaper. Våtimpregnering samt tre ulike typer polyolsyntese ble brukt for å gi Pt elektrokatalysatorer med isolerte og sammenslåtte partikler, og samtidig kunne gi fleksibilitet til å velge den dominerende orienteringen. Syntetiserte Pt nanopartikler som enten var isolerte, aggregerte eller filmbelagt ble lagt på en finfordelt karbonbærer i form av partikler (carbon black), nanofiber eller nanorør og karakterisert ved ex-situ fysiokjemiske og elektrokjemiske metoder. Deretter ble tre av katalysatorprøvene med de ulike Pt strukturene testet som katodekatalysator i en PEM brenselcelle før og etter en akselerert nedbrytningstest (ADT) med N_2/harmix i tillegg til eksponering for CO(g).
Isolerte katalysatorpartikler gav en høyere aktivitet for oksygen reduksjonsreaksjonen (ORR) etterfulgt av filmbelegg og til slutt aggregerte partikler. På den andre siden så hadde den relative holdbarheten (det prosentvise ytelsestapet ved ADT) en motsatt tendens.
CO toleransen for katalysatorer med isolerte katalysatorpartikler var høyere enn for de med aggregerte partikler, mens gjenopprettingen av ytelsen til brenselcellen etter å ha blitt utsatt for CO var noe høyere for katalysatorer med aggregerte partikler enn tilfellet var for de med isolerte partikler.
To ulike eksperimentelle målinger ble ikke utført på alle formene for Pt fordeling. Dynamisk elektrokjemisk impedansspektroskop (dEIS) ble kun utført på katalysatorer med aggregerte Pt-partikler på karbonpartikler, mens ytelsen og holdbartheten som funksjon av tykkelsen til katodekatalysatorsjiktet ble studert for katalystatorer bestående av isolerte partikler. dEIS viste seg å være en særdeles sensitiv metode, og gjorde det mulig å observere små endringer i elektrodeytelse som ikke enkelt lot seg detektere ved syklisk voltammetri, CO stripping.
Katoder med ulik tykkelse på det elektrokatalytiske sjiktet (CCL) som følge av ulik platinamengde på karbonbærer, henholdsvis 10 wt%, 20 wt% og 30 wt%, ble testet i en $H_2|O_2$ brenselcelle før og etter en akselerert nedbrytningstest. Pt partiklene bestod av kun isolerte Pt-partikler i alle tilfellene. Den initielle elektrokjemiske aktiviteten ble funnet å være uavhenging av CCL tykkelse, men i fortynnet oksygen var aktiviteten sterkt avhengig av CCL tykkelse eller Pt/karbon forhold. Reduksjonen i cellespenningen for prøven med 10 wt% Pt på karbon var mye større enn tilfellet var for de to andre prøvene, noe som ble tilskrevet den lokale strømtettheten. Vi foreslår at den lokale strømtettheten for denne prøven krysser en grense mellom to Tafelregimer ved ADT,

mens den forble i samme Tafelregime for 20 wt% og 30 wt% prøvene både før og etter nedbrytning.

Preface

The work has been performed at the Department of Materials Science and Engineering, NTNU, Trondheim. It has been a part of the N-INNER project "Nanoduramea – synthesis and durability of CNT-based MEAs for PEMFC" and financially supported by the Research Council of Norway and the Department of Materials Science and Engineering, NTNU. The Nanoduramea project consisted of partners from Finland (Aalto University and VTT), Sweden (KTH), Denmark (SDU) and Norway (NTNU and SINTEF).

In the first years the work focused on synthesis of Pt/C catalysts with controlled structural properties. The main task in the remaining time was then to study fuel cell performance of different catalysts with various Pt dispersion regimes and in several atmospheres.

The thesis consists of eight chapters; the first two ones are introduction and methodology of the experimental studies. The subsequent five chapters are written as paper manuscripts, two of these were already published and the other three are intended for publication. Some other papers published in peer-reviewed journals and a number of conference papers were also published in the course of the PhD work that are not included in the thesis.

The papers are co-authored. The author of the thesis was the main contributor of the papers together with contribution from the colleagues:

Paper I: Architecture design for nanostructured Pt/C electrocatalysts via optimizing synthesis conditions

I performed the synthesis and characterization of the samples with contribution from Navaneethan Muthuswamy and assistance from José Luis Gómez de la Fuente. I interpreted the data and wrote the paper.

Paper II: The influence of catalyst layer thickness on the performance and degradation of PEM fuel cell cathodes

I performed the synthesis, ex-situ physicochemical characterizations and wrote the paper with contribution from Alejandro Oyarce Barnett. I performed the ex-situ electrochemical characterizations and the in-situ electrochemical characterizations and data interpretation were carried out mainly by Alejandro Oyarce Barnett with my contribution.

Paper III: Pt nanoparticles dispersion influence on fuel cell performance

I performed the synthesis; physical and electrochemical characterizations and wrote the paper.

Paper IV: CO-dependent fuel cell performance of isolated and aggregated platinum nanoparticles supported on carbon black

I performed the synthesis, physical and electrochemical characterizations and wrote the paper.

Paper V: Dynamic EIS study of Pt/C-based MEAs subjected to cycling protocols

I performed the synthesis and physicochemical characterizations and wrote the paper with contribution from Per Kristian Dahlstrøm. I also performed the ex-situ electrochemical characterization and the in-situ electrochemical characterization and interpretation were performed mainly by Per Kristian Dahlstrøm with my contribution.

Acknowledgements

Reviewing the memories of the past few years in the course of my PhD program at NTNU in Trondheim, I feel indebted to many people for being so supportive and helpful. The successful completion of this PhD project would have not been possible without them.

First, I wish to thank my supervisor Prof. Svein Sunde for all his scientific and everyday life advice and support. I have been privileged to be working at Electrochemical Energy Group under his supervision and I am thankful for this valuable opportunity. I am also very grateful to Dr. Frode Seland who has always been a source of energy and inspiration.

I would like to thank Dr. José Luis Gómez de la Fuente and Dr. Navaneethan Muthuswamy for their excellent help and collaboration to establish the synthesis techniques. I also thank the friendly help and collaboration offered by the researchers at SINTEF especially Dr. Magnus S. Thomassen, Dr. Anders Ødegård and Dr. Edel Sheridan. I am grateful to Prof. Magnus Rønning and Prof. De Chen from the Department of Chemical Engineering for the scientific input. Dr. Virginia Ruiz from Aalto University deserves special recognition for providing the nanostructured samples.

I am very thankful to Prof. Göran Lindbergh and especially Dr. Alejandro Oyarce Barnett who hosted me during my useful visiting period at KTH Division of Applied Electrochemistry in 2010.

For the characterization tasks of the thesis I received a lot of help and encouragement from so many and I am truly thankful to them all: Dr. Yingda Yu and Dr. Per Erik Vullum for TEM imaging, Dr. Per Kristian Dahlstrøm for dEIS experiments and memorable collaboration and Dr. Julian Tolchard not only for SEM and XRD measurements but also fruitful scientific advices.

I would also like to thank those who offered administrative and practical support in the course of my PhD studies especially Dr. Ehsan Houshfar, Amin H. Zavieh, Elin Synnøve Isaksen Kaasen and Ola-Marius Langelo Røyset.

The PhD work has been funded by the Research Council of Norway through the Nanoduramea project. The funds for the scientific travelling were partly provided by the Faculty of Natural Sciences and Technology and UNIFOR and I am grateful for that.

Last but not least, I wish to thank my whole family especially my lovely wife for their unconditional love and endless support.

Mahdi Darab

Bergen, October 2014

Summary

The main objective of this work has been to develop the understanding of the effect of Pt particle dispersion on activity and durability of the Pt/C electrocatalysts. In order to have such understanding, extensive testing of the electrocatalysts with different structure ex-situ and in-situ was needed.

The first step was to synthesize the electrocatalysts with desired structural and thus electrochemical features. Wet impregnation and three forms of polyol techniques were used and Pt/C catalysts with isolated and aggregated particles with the flexibility to choose the dominant phase were synthesized. The isolated, aggregated and film-coat Pt nanoparticles on carbon black, carbon nanofiber and carbon nanotube were studied physico-chemically and ex-situ electrochemically. Then three samples, the catalysts with aggregated, with only isolated and with film-coat Pt nanoparticles were tested in a fuel cell before and after an accelerated degradation test (ADT) with N_2/harmix and also the exposure to CO.

Isolated particles presented higher ORR activity followed by film-coat and finally aggregated particles. However, the relative durability (the percentage in performance loss upon ADT) had an opposite trend.

The CO tolerance of catalysts with isolated particles was higher than for those with aggregated particles, but recovery of the fuel cell performance after being exposed to CO was slightly higher for catalysts with aggregated particles than for those with isolated particles.

Two types of experiments were not applied to all types of Pt dispersion. Dynamic electrochemical impedance spectroscopy (dEIS) was only applied to catalysts with aggregated particles, and performance and degradation as a function of cathode catalyst layer (CCL) thickness was only studied for catalysts containing isolated particles only. dEIS proved to be a convenient tool for investigation of small changes in the electrode, and it was possible to detect changes in electrode performance that would go practically un-detected by cyclic voltammetry, CO stripping and transmission electron microscopy.

Electrodes with different thickness based on cathode electrodes with Pt loadings of 10 wt%, 20 wt%, and 30 wt% (containing only isolated Pt particles), were tested in a $H_2|O_2$ fuel cell before and after an ADT. The initial electrochemical activity was found to be independent of CCL thickness but in diluted oxygen, the activity was strongly dependent on the CCL thickness or Pt-to-carbon ratio. There was a much larger reduction in cell voltage for the sample with 10 wt% Pt loading comparing with the other two samples that was attributed to the local current density. We suggest that the local current density for this sample crosses a border between two Tafel regimes upon ADT while the 20% and 30% sample remained in the same Tafel regime also after the degradation.

Table of Contents

List of Figures

List of Tables

Symbols and Nomenclature

Roman letters

A	Area
a	Specific surface area
A_g	Geometric area
a_i	Activity of specie i
b_T	Tafel slope
$E_{equilibrium}$	Equilibrium potential
ΔE^0	Change in standard potential
ESA_{CO}	Electrochemically active Surface Area
F	Faraday constant
ΔG	Gibbs free energy change
ΔG^o	Gibbs free energy change at standard conditions
$\Delta \bar{g}_f^{\,0}$	Change in molar Gibbs free energy of formation at standard conditions
ΔH	Enthalpy of reaction
I	Current
i	Current density
$i_{critical}$	Critical current density
n	number of electrons involved in overall electrode reaction
P	Pressure
P_0	Standard pressure
P_{O_2}	Oxygen partial pressure
Q_{CO}	Transferred charge in CO oxidation region
Q_H	Transferred charge in hydrogen region
R	Resistance
Ri	CCL ionomer resistance
R_{pol}	Polarization resistance
ΔR_{pol}	Change in polarization resistance
ΔS	Change in entropy
T	Temperature
t	Time
T_1	High temperature level in thermal process

T_2	Low temperature level in thermal process
T_{cell}	Temperature of the cell
T_{hum}	Humidification temperature
T_{pipes}	Temperature of the pipes in fuel cell
V	Volume
W_{Pt}	Platinum mass used in the catalyst

Greek letters

ε_r^{cell}	Hydrogen fuel cell efficiency
$\varepsilon_r^{thermal}$	Heat engine efficiency
ε_V	Electrochemical efficiency
$\eta_a(i)$	Anodic overpotential
$\eta_c(i)$	Cathodic overpotential
ν	Sweep rate

Abbreviations

ADT	Accelerated degradation test
AFC	Alkaline fuel cell
CCL	Cathode catalyst layer
CE	Counter electrode
CHP	Combined heat and power
CPA	Chloroplatinic acid
CV	Cyclic voltammetry
dEIS	Dynamic electrochemical impedance spectroscopy
DMFC	Direct methanol fuel cell
EDX	Energy-dispersive X-ray spectroscopy
EG	Ethylene glycol
EIS	Electrochemical impedance spectroscopy
ESA	Electrochemically active surface area
FC	Fuel cell

FFT	Fast Fourier transform
GDE	Gas diffusion electrode
GDL	Gas diffusion layer
GNF	Graphitized carbon nanofiber
HFR	High frequency resistance
HOR	Hydrogen oxidation reaction
IEP	Isoelectric point
MCFC	Molten carbonate fuel cell
MEA	Membrane electrode assembly
NGL	Natural gas liquids
NHE	Normal hydrogen electrode
OCP	Open circuit potential
OPEC	Organization of the petroleum exporting countries
ORR	Oxygen reduction reaction
PAFC	Phosphoric acid fuel cell
PEM	Proton exchange membrane
PEMFC	Proton exchange membrane fuel cell
PZC	Point of zero charge
RE	Reference electrode
RH	Relative humidity
RHE	Reversible hydrogen electrode
SAED	Selected area electron diffraction
SEM	Scanning electron microscopy
SOFC	Solid oxide fuel cell
TGA	Thermogravimetric analysis
TEM	Transmission electron microscopy
TPO	Temperature programmed oxidation
WE	Working electrode
XRD	X-ray diffraction

Chapter 1

Introduction

This chapter provides an introduction to the research work presented in this thesis. It starts with a description of the research background and explains the motivation for performing this work. It also provides an overview of the approach taken as well as the results obtained. Finally, it introduces the structure of the thesis and the list of publications it includes.

1.1 Background

The human beings in today's world need energy more than ever. Primary energy demand is expected to increase by 41% between 2012 and 2035 with growth averaging 1.5% per annum in the world [1]. Global primary energy consumption increased by 2.3% in 2013, as an acceleration over 2012 (+1.8%)[2]. So far the cornerstone of energy supply has been fossil fuels in the world even though its market share decreases gradually [2].
However, the resources of fossil fuels and specifically crude oil reserves are being depleted globally. As an example, Norway, one of the largest non-OPEC oil producers, produced in average 2.27 million barrels of hydrocarbon liquid (crude oil, NGL and gas condensate) per day in June 2008 [3] which decreased to a daily average of 1.84 million barrels of liquid hydrocarbons in August 2014 [4]. Given all the geopolitical considerations and

environmental issues associated with oil, the tendency to find an alternative high-efficiency power source appears more attractive than ever today.

The reliability on nuclear energy was also undermined to a large extent as a consequence of 2011 Tōhoku earthquake and tsunami in Japan, reminiscent of the Chernobyl disaster in 1986. The global aftermath of the earthquake resulted in the largest decline on record in nuclear output, -44% in Japan, -23% in Germany and -4.3% worldwide [5].

Hitting a record of 2.7% of global energy consumption[2], renewable energy conversion systems are a natural choice vowing for a clean and sustainable energy supply should the practical and economic challenges be addressed.

Alternative renewable energy sources such as geothermal heat, sunlight and wind require that large-scale energy storage is available. Storage is important since renewable energy sources are frequently intermittent in nature, and the energy surpluses provided by for example solar cells during day-time need to be transferred to night-time so that energy is available at all times. Flexibility with respect to the primary energy source would be a distinct advantage of any proposed storage technology, so that it can operate with equal facility for wind, solar, and other renewable sources so as to utilize available energy sources with maximum efficiency.

There are several options for energy storage available, such as pumped hydropower storage, compressed gas in rock cavities, flywheels and storage in the grid itself. These technologies are of limited utility, however, in transportation and mobile applications and may also be subject to geographical constraints.

Hydrogen, however, is a serious contender for the energy carrier for renewable energy systems with energy density as high as 120 MJ/kg and appropriate possibilities for storage and transport. Hydrogen is believed to play an important role in future energy scenarios based on renewable energy, should the question of how to store hydrogen in a safe and effective manner be answered satisfactorily [6].

There appears to be a wide range of possibilities when it comes to the hydrogen storage such as high pressures, cryogenics liquefaction and chemical compounds that absorb and release hydrogen reversibly upon temperature alteration and the technology in this area is still progressing [7].

To provide hydrogen, hydrocarbon resources are the most straightforward choice but as it depletes fossil resources and generates large amounts of CO_2, this option is not viable. State-of-the-art water electrolyzers, on the other hand, are popular candidates for hydrogen production. If coupled with fuel cells, they can present a closed loop of realized renewable energy source with hydrogen as energy carrier. Even though the overall efficiency is not an issue, the environmental considerations and availability lying behind the hydrogen-economy idea are strong driving forces for the attention that the hydrogen cycle has received since its conception in the late 1960's.

Fuel cells are electrochemical devices that convert chemical energy to electricity through electrochemical reactions at two electrodes. The oxidation reaction occurs at anode side and the reduction reaction takes place at the cathode side and the overall spontaneous electrochemical reaction proceeds while releasing electricity and heat.

Fuel cells are one of types of devices that would naturally be included in renewable energy systems due to their high efficiency. Fuel cells are straightforward to maintain mainly since they have no major mechanical parts. Fuel cells are also excellent devices when it comes to being environmentally friendly. Their operation is silent, which can be a significant advantage in some applications. Fuel cells have a wide range of potential applications in different areas, from automotive and aerospace technologies to mobile and even bio-system applications.

1.2 **Fuel cell and PEMFC principles**

Table 1-1 shows the different types of fuel cell systems reviewing the operating conditions, components and applications.

It seems that among the fuel cell types, PEMFCs are very attractive from the market viewpoint mainly due to their large range of applications [8][9].

The design of a PEM fuel cell is schematically shown in Figure 1-1.

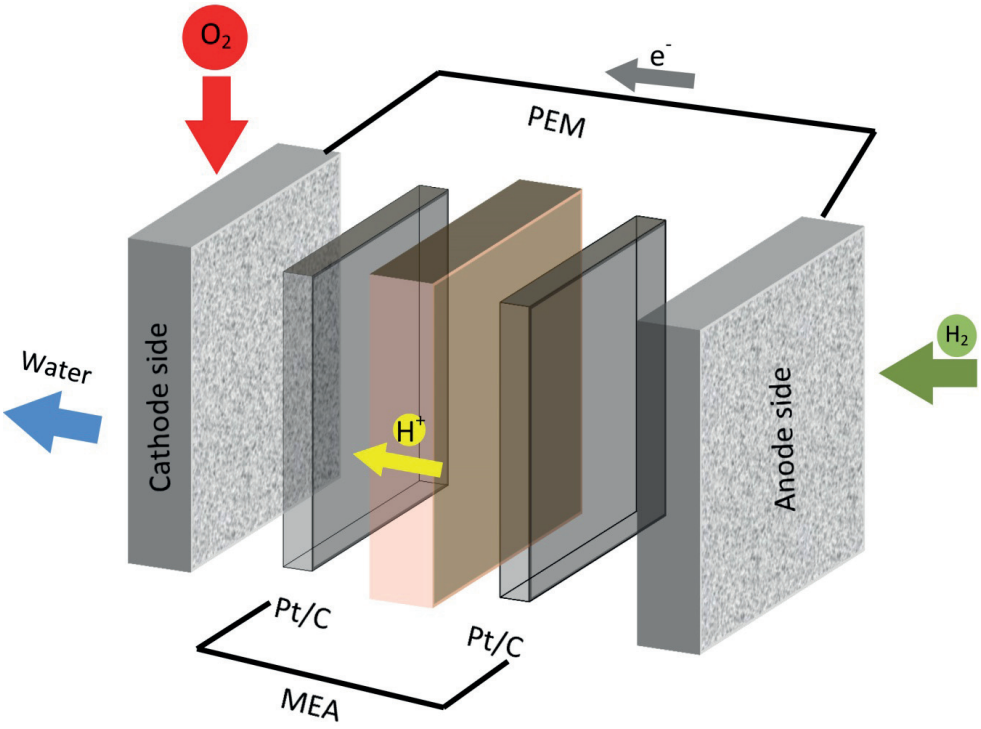

FIGURE 1-1: Schematic representation of PEM fuel cell components.

Table 1-1: Common fuel cell types and their characteristics [10].

Type	Charge carrier	Electrolyte	Catalyst	Reaction	Operating temperature	Fuel	Electrical Efficiency	Application
PEMFC	H^+	Polymer membrane	Platinum	Anode: $H_2 \rightarrow 2H^+ + 2e^-$ Cathode: $½O_2 + 2H^+ + 2e^- \rightarrow H_2O$	50-120 °C	H_2	50-60%	Transportation, military, space. electrical portable devices
AFC	OH^-	KOH	a variety of non-precious metal catalysts	Anode: $H_2 + 2OH^- \rightarrow 2H_2O + 2e^-$ Cathode: $½O_2 + H_2O + 2e- \rightarrow 2OH^-$	<100 °C	H_2	50-60%	Space, military, transportation
DMFC	H^+	Polymer membrane	Platinum	Anode: $CH_3OH + H_2O \rightarrow CO_2 + 6H^+ + 6e^-$ Cathode: $½O_2 + 2H^+ + 2e^- \rightarrow H_2O$	50-120 °C	CH_3OH	<40%	Transportation, electrical portable devices
SOFC	O^{2-}	ZrO_2/Y_2O_3	low-cost non-platinum catalysts	Anode: $H_2 + O^{2-} \rightarrow H_2O + 2e^-$ Cathode: $½O_2 + 2e^- \rightarrow O^{2-}$	500-1000 °C	H_2, CH_4, CO	55-65%	CHP for stationary decentralized systems, transportation for heavy vehicles
MCFC	CO_3^{2-}	Li_2CO_3/Na_2CO_3	low-cost non-platinum catalysts	Anode: $H_2 + CO_3^{2-} \rightarrow H_2O + CO_2 + 2e^-$ Cathode: $½O_2 + CO^2 + 2e^- \rightarrow CO_3^-$	600-800 °C	H_2, CH_4	60-65%	
PAFC	H^+	H_3PO_4	Platinum	Anode: $H_2 \rightarrow 2H^+ + 2e^-$ Cathode: $½O_2 + 2H^+ + 2e^- \rightarrow H_2O$	160-220 °C	H_2	50-55%	Electrical devices, transportation, stationary

In PEM fuel cell anode is fed with pure hydrogen and cathode with pure oxygen. The reactions on both electrodes are presented in Eq. (1-1) - (1-3).

Anode: $H_2 \rightarrow 2H^+ + 2e^-$ $E^0 = 0\ V_{NHE}$ *(1-1)*

Cathode: $\frac{1}{2}O_2 + 2H^+ + 2e^- \rightarrow H_2O$ $E^0 = 1.23\ V_{NHE}$ *(1-2)*

Overall: $H_2 + \frac{1}{2}O_2^- \rightarrow H_2O$ $E^0 = 1.23\ V_{NHE}$ *(1-3)*

The PEM is responsible for proton transport, and the product of the electrochemical reaction, water, is the exhaust substance from the PEM fuel cell. The produced electricity is relayed through an external circuit between the anode and cathode. In addition to water and electricity, heat is also an outcome of the cell.

Eq. (1-2) is called oxygen reduction reaction (ORR) and is associated with sluggish kinetics which is usually considered a major loss in fuel cell operation.

1.2.1 Fuel cell efficiency

The efficiency for heat engines such as an internal combustion engines or steam and gas turbines is limited by the Carnot efficiency. Carnot showed that for a heat engine with the maximum temperature T_1 and the heated fluid released at temperature T_2 then the maximum possible efficiency is[11][12]:

$$\varepsilon_r^{\ thermal} = \frac{T_1 - T_2}{T_1} \tag{1-4}$$

In hydrogen fuel cells, which operate at constant pressure and temperature, the efficiency is defined as the change in Gibbs free energy over the change in enthalpy:

$$\varepsilon_r^{\ cell} = \frac{\Delta G}{\Delta H} = 1 - \frac{T\Delta S}{\Delta H} \tag{1-5}$$

In Eq. (1-5), T is temperature and S is entropy.

For low temperature operation the theoretical efficiency of the heat engine is lower than that of the fuel cell. In practice, overpotentials and ohmic losses affect the efficiency for fuel cells significantly. The effects of these losses are embedded in what is known as the electrochemical efficiency, ε_v:

$$\varepsilon_V = \frac{\Delta E_{cell}}{\Delta E^0} = 1 - \frac{\left(|\eta_a(i)| + |\eta_c(i)| + Ri\right)}{\Delta E^0} \tag{1-6}$$

where $\eta_a(i)$ and $\eta_c(i)$ are the anodic and cathodic overpotential respectively, and the term Ri represents ohmic losses in the membrane and elsewhere. The thermodynamic potential can be linked to the standard change in electrical potential through

$$\Delta G^o = -nF\Delta E^0 \tag{1-7}$$

where ΔG^o is change in Gibbs free energy at standard temperature and pressure, and with pure reactants, n is the number of electrons transferred in the reaction, F=96485 As/mol is the Faraday constant and ΔE^0 is the change in standard potential of the cathode and anode reactions.

For the overall reaction in oxygen-hydrogen fuel cell in Eq. (1-3), we have:

$$\Delta G^o = -237\text{kJ/mol} \tag{1-8}$$

For a general reaction of:

$$aA + bB \rightarrow cC \tag{1-9}$$

where a moles of A react with b moles of B to produce c moles of C, each of the reactants and the products, has an associated 'activity'. For ideal gases we define the activity a_i to be:

$$a_i = \frac{P_i}{P_0} \tag{1-10}$$

In this equation P_i is the partial pressure of species I and P_O is the standard pressure.

For a general reaction like Eq. (1-9), we have[13]:

$$\Delta\bar{g}_f = \Delta\bar{g}_f^{\,0} - RT\ln\left(\frac{a_A{}^a a_B{}^b}{a_C{}^c}\right) \tag{1-11}$$

where $\Delta\bar{g}_f^{\,0}$ is the change in molar Gibbs free energy of formation at standard pressure. In the case of fuel cell considering overall reaction Eq. (1-3), it becomes:

$$\Delta\bar{g}_f = \Delta\bar{g}_f^{\,0} - RT\ln\left(\frac{a_{H_2} a_{O_2}{}^{0.5}}{a_{H_2O}}\right) \tag{1-12}$$

Substituting this equation in Eq. (1-7), we obtain:

$$E = \frac{\Delta \bar{g}_f^{\,0}}{2F} + \frac{RT}{2F}\ln\left(\frac{a_{H_2} a_{O_2}^{\,0.5}}{a_{H_2O}}\right) = E^0 + \frac{RT}{2F}\ln\left(\frac{a_{H_2} a_{O_2}^{\,0.5}}{a_{H_2O}}\right) \quad (1\text{-}13)$$

It can be also written as:

$$E_{equilibrium} = E^0 + \frac{RT}{2F}\ln\left(\frac{P_{H_2} P_{O_2}^{\,0.5}}{P_{H_2O}}\right) \quad (1\text{-}14)$$

With Eq. (1-14) which is the Nernst equation for the reaction, we can predict how the reactant and product partial pressures affect the voltage in a fuel cell.

The Nernst equation gives the reversible open circuit potential of a PEMFC in certain conditions but in reality the potential of a fuel cell is less than the theoretical potential as discussed in efficiency definition. In general one expects the kinetics to improve with activities of the reactants, such as the oxygen partial pressure for the ORR.

1.2.2 Fuel cell components

Catalysts and membranes in a typical PEM fuel cell configuration are usually integrated in what is referred to an electrode membrane assembly (MEA), and which may be considered the heart of the fuel cell and where the chemical reactions take place. The membrane serves the purpose of proton exchange from the anode side to the cathode side while relegating the electrons to the outer circuit. Nafion® is the most used and commercially available material for PEM fuel cells, and was also used in this work. Nafion conduct protons through sulfonic acid groups attached to the side-chain of a grafted perfluorinated (Teflon-like) polymer. For the conduction process to be efficient the polymer needs to be kept sufficiently humid during operation.

The MEA is usually connected with porous gas diffusion layers (GDLs) on either side of the cell. These GDLs, are usually made of carbon and allow gases through to the MEA to participate in the electrochemical reaction. A carbon plate with gas channels (bipolar plate) is, in turn, usually attached to the GDL for current collection and gas supply.

Among the practical considerations associated with PEMFC operation, water management is an important issue affecting the performance and durability of the cell [14]. Water management is a complex process where on one hand there is a need to have sufficient humidity (normally from incoming gases) to maintain the proton conductivity of the PEM, and on the other hand excess water must be removed from the cell in order to avoid water flooding in the catalyst layer and/or GDL. If surplus water, which may come from condensation of water in the humidified gas stream and water production at the cathode, cannot be removed efficiently there is a significant risk that the gas transport pathways in the electrodes, GDLs and gas channels get blocked and a significant mass transport loss be imposed [15]. It has been shown that flooding is likely

to occur at low temperatures, high humidification, and high current densities where the gases in the fuel cell become supersaturated with water vapor [16]. However, it can also take place even at low current densities under specific circumstances, such as low gas flow rates and very low temperature where saturation of the gas phase by water-vapor occurs with greater facility [17].

To understand the mechanisms for flooding and eventually mitigate the water management issues, studies are focused on the effect of flooding on catalyst layer, GDL and membrane. Modeling studies [18] suggest that cathode catalyst layer (CCL) acts like a watershed in the fuel cell and adapts the balancing between the reverse water fluxes towards the membrane and the cathode outlet. They also highlighted the role of CCL as critical component in view of the fuel cell performance loss due to excessive flooding. Developing a novel fluorescence microscopy technique to study the flooding effects in GDLs, Litster et al. suggested that the water is not transported through a converging capillary tree but rather via fingering and channeling phenomena [19]. Sinha et al. studied the effect of GDL hydrophilic fraction distribution to mass transport limitations caused by water transport in fuel cell and suggested a wettability-tailored GDL model to minimize the flooding-associated mass transport issues [20]. Lu et al. studied the water management in fuel cell through understanding the two-phase flow of water and reactant gases in the gas distribution channels of proton exchange membrane fuel cells [15]. They investigated the flow regimes in different circumstances and discovered that the two-phase flow at low superficial air velocities is dominated by slugs or semi-slugs flow patterns, leading to unsatisfactory flow distribution and large fluctuations in the pressure drop. These are few examples of the studies on water management in PEMFCs and there are still several research works going on to better understand the flooding mechanisms and to limit the damages caused by excess water in the fuel cell while attempting not to compromise on the humidity content in the polymer membrane.

Electrodes are the electrochemical reaction sites and therefore the heart of the fuel cell and are also the focus of this thesis. Simple redox or outer-sphere reactions comprise electron exchange without involving to adsorption process and then the electrode plays the role of electron source only. In fuel cell electrode reactions, however, the adsorption of intermediates at the electrocatalyst surface plays an important role in the reaction. In fuel cell, chemical composition, structure and architecture of the electrocatalysts can significantly influence the overpotential of the reactions.

For fuel cells in general and for PEMFCs working at temperatures less than 100 °C in particular, the role of electrocatalyst to increase the rate of the reactions especially ORR, is vital. A catalyst should possess above all a high intrinsic activity for the electrochemical oxidation of hydrogen at anode side as well as for oxygen reduction at cathode side. Furthermore the catalyst material should be a proper electron conductor. It is also important to have a chemically stable catalyst material that can have a reasonable durability over the life of fuel cell.

Normally an active noble metal such as Pt or its alloys is used to catalyze the fuel cell reactions. To effectively utilize the active metal, that is normally quite expensive, it is dispersed and supported on a high-surface-area substrate. Carbon materials are popular candidates due to low cost and high electrical conductivity and also chemical stability in fuel cell working conditions and Pt supported on high surface area carbon was also the electrocatalyst of choice in this project.

The main drawback of Pt-based catalysts i.e. the limited availability and high cost [21] make researchers to seek for possibilities to use them more efficiently. Here is the improvement offered by nanoscience where Pt nanoparticles can be finely dispersed and efficiently used in PEMFCs. Nanostructuring Pt/C electrocatalysts that increases the surface-to-volume ratio, reported to be one of the alternatives to enhance activity and durability of Pt/C electrocatalysts [22][23] and this was the approach in the current work as well.

1.3 Pt/C performance and affecting factors

Although new electrocatalysts with less costly materials are emerging [24][25][26][27][28], platinum nanoparticles and related alloys deposited on various carbon structures (Pt/C) having the highest ORR activity [29][30] still appear to receive much attention in the electrochemical community [31][32][33][34].

Pt nanoparticles supported on high surface area carbon (like Vulcan XC-72 in this work) are in principle able to meet the performance requirements for commercial fuel cell applications. However, in addition to cost issues the durability of currently known electrocatalysts materials still need to be improved especially for use under the harsh operating conditions of a PEM fuel cell [35].

The performance and durability of a Pt catalyst dispersed on carbon is among other things affected by

- Particle size
- Particle shape
- Dispersion and agglomeration
- Metal loading
- Carbon type
- Presence of CO
- CCL thickness

1.3.1 Particle size

Particle size effect is well-established [36][37][38][39] and for instance it is now known that there is an optimum for Pt particle size with respect to the mass activity for ORR around 3.5 nm [40]. The durability of a cathode subject to aging cycles, increases with increasing Pt particle size [41].

1.3.2 Particle shape

In addition to the particle size, the catalytic performance of Pt/C can also be optimized via the shape of nanoparticles which determines surface atomic configuration and coordination [42][43][44]. For example with respect to ORR, Tian et al. [45] reported that high-index facets of platinum nanoparticles such as {730} present a higher density of reactive sites than the most typical platinum nanoparticles such as {100}, {110} and {111}. The reason is that the high-index planes possess a higher density of atomic terraces, steps and kinks as active sites for the chemical breaking reactions [46].

1.3.3 Dispersion and agglomeration

In terms of particle dispersion, it is natural to think that isolated Pt particles have higher surface area available for electrochemical reactions such as ORR if compared with agglomeration-containing electrocatalysts where a lot of reactive sites are already blocked by particle lumping and remained inaccessible for electrochemical reactions.

The durability of well-dispersed Pt nanoparticles and the affecting parameters are also well-documented now. For example it has been shown that the gas atmosphere and the upper potential limit in accelerated stress protocols play an important role in dictating the degradation mechanisms [47]. There has, however, been little work performed to understand the durability of agglomeration-containing Pt/C electrocatalysts.

1.3.4 Metal loading

One of the most costly parts of PEMFCs is precious metals used as the active catalyst materials in the fuel cell and the efforts in this area has been focused to decrease the metal loading without compromising catalytic activity. As a result of these efforts, the total required Pt loading in fuel cells decreased from 4 mg cm^{-2} in 1990s [48] to less than 0.4 mg cm^{-2} to date [49] which is still far from the suggested target of 0.125 $mg_{Pt}cm^{-2}$ for 2020 [50]. The main breakthrough in the Pt catalysis for PEM fuel cells was to use carbon-supported Pt nanoparticles instead of unsupported Pt black.

In most cases of the new catalyst with very low Pt loadings, the required loading have been obtained with formulations of no more than 20 wt% Pt on carbon in today's state-of-the-art catalysts [49]. The decrease in Pt loading, however, should be performed with caution since the total surface area of Pt in the electrode falls with reducing Pt loadings and that in turn negatively affects the activity of the fuel cell [51].

1.3.5 Carbon type

Carbon materials have been used for a long time as supports for Pt/C catalysts due to their high electrical conductivity, chemical stability and low cost [52]. Different types of carbon material have been suggested to be used as support to Pt particles in PEMFCs, including but not limited to activated carbon [53], high-surface area carbon black [35], graphitized carbon nanofibers (GNFs) [32] and carbon nanotubes (CNTs) [54]. It is almost always the case for carbon supports that the more surface defects lead to higher catalytic activity but at the same time, the carbon corrosion initiates from the defects on the surfaces and that necessitates the restriction of such defects from durability view point. On the other hand, low amount of surface defects means there is a need for surface pretreatments before the support can obtain the minimum quantity of sites for Pt nanoparticles to be anchored. Therefore choosing the best support material candidate is engaged with considerations of activity, requirements for surface modification and functionalization, and durability [55].

Carbon black with high surface area (~250 m^2g^{-1} for Vulcan XC-72, consisting of spherical graphite particles with less than 50 nm in diameter), low cost and high availability [56] fulfill the main criteria mentioned above as support for Pt and Pt-alloy electrocatalysts in PEMFCs and that is the reason that carbon black is the most used support material for Pt nanoparticles in PEM fuel cells [56][57] and was also the choice of support for most of the electrocatalysts used in this thesis.

GNFs as catalyst support have shown high thermal stability and corrosion resistance in PEM fuel cell environment over carbon black and CNTs [32]. However, they have an inert surface with very limited amount of surface defects for the anchorage of Pt nanoparticles. Sophisticated modifications of the fiber surface are required to address this issue.

CNTs are typically two dimensional nanostructure tubes, formed by rolled up single sheets of hexagonally arranged carbon atoms [58]. If compared with carbon black, they seem to present a comparable or less initial catalytic activity towards ORR but slightly higher resistance against oxidation [59] and higher durability which is attributed to the specific interaction between Pt particles and carbon nanotubes [60]. In a similar manner to GNFs, the main challenge associated with CNTs is the fact that the pristine CNTs are chemically inert and it is difficult to attach Pt particles on them without intensive pretreatment. Metallic impurities leftover from the CNTs preparation and catalytic formation steps are also always a hurdle to disperse them effectively in colloidal solutions [56].

Although not in the scope of this thesis, it is worth pointing that in addition to the carbon supports mentioned, there are novel carbon materials like carbon nanocages emerging recently with claimed remarkable durability characteristics [61].

1.3.6 Presence of CO

The ability of catalysts to oxidize CO is important for PEMFC catalyst due to the fact that a number of fuels will contain CO. CO, in turn, tends to poison (reversibly) Pt catalyst, for instance. The interaction of CO with Pt catalysts in the literature is typically referred as CO poisoning [62]. It is now established that the electrooxidation of uncontaminated hydrogen on the anode Pt electrocatalyst takes place according to the following two-step reaction [63]:

$$H_2 + 2(\mathrm{P}t) \Leftrightarrow 2(Pt-H) \qquad (1\text{-}15)$$

$$2(Pt-H) \Leftrightarrow 2(Pt) + 2H^+ + 2e^- \qquad (1\text{-}16)$$

Then in a CO-contaminated stream of hydrogen fed to anode, CO molecules have the possibility to either adsorb on a bare Pt site or a Pt-H site [62]:

$$CO + (\mathrm{P}t) \rightarrow (Pt=CO) \qquad (1\text{-}17)$$

$$2CO + 2(Pt-H) \rightarrow 2(Pt=CO) + 2H^+ + 2e^- \qquad (1\text{-}18)$$

The adsorbed CO blocks active platinum sites in the anode as schematically presented in Figure 1-2.

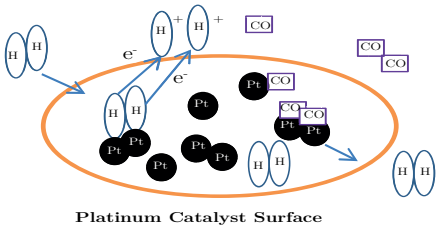

FIGURE 1-2: Schematic representation of the CO adsorption theory on the platinum catalyst. Redrawn from [62].

It is well-established that the extent of poisoning by CO is dependent on the CO concentration, operating conditions, exposure duration and the type of the anode catalyst [64].

CO electrooxidation has been also well investigated in terms of the effect of particle size, and it has been shown that the rate of the reaction decreases with decreasing particle size [65]. Results indicate that individual Pt nanoparticles are less active in terms of CO monolayer oxidation compared to Pt aggregated nanoparticles. This is related to aggregates including large amounts of grain boundaries interconnecting the catalyst crystallites, and defect sites which seem to be more active to the reaction appear in the

catalyst [66][67]. It has been also well-established that CO monolayer oxidation may occur at multiple potentials in samples with aggregated particles [68][69] as a tool to judge the Pt particle dispersion and this method was widely employed in the current research.

The CO poisoning issue for isolated Pt particles (samples with well dispersed Pt nanoparticles) is well studied and it has thus been shown that Pt catalysts are simply poisoned by even trace amounts of carbon monoxide in the feed. This is still challenging in terms of commercialization of PEMFCs [70]. However, it seems that more insight into the CO-dependent performance of electrocatalysts with aggregated Pt particles is needed.

1.3.7 CCL thickness

Other influential structural properties of cathode catalyst layers (CCLs) have also been the topic of many studies over past few years to successfully simulate and optimize CL in terms of porosity, loading, and CCL thickness. For example Suzuki et al. attempted to understand the link between the CCL's particulars such as pore networks and the polarization characteristics predicting that with the same catalyst loading an MEA with 40% porosity has better electrochemical performance than an MEA with 50% porosity [71].

While there is research related to the effect of the thickness of the Nafion® electrolyte on fuel cell performance [21], there appears to be little experimental work on the effect of CCL thickness. This could be potentially another area of structure-dependent PEMFC performance with regards to electrodes.

As a conclusion, Pt/C still appears to be the preferred electrocatalyst for PEMFCs. The Pt particle size is desired to be between 2 nm and 5 nm and the carbon material is required to have a very high surface area. Structural properties and structure-dependent PEMFC performance such as CCL thickness deserve a study, and there seems to be a lack of information in the literature in this context. Pt particle dispersion on the support is determinant on the performance of the electrocatalyst, and it is vital to understand the effect of particle agglomeration and the (changing) structure of electrocatalyst on the electrochemical activity towards ORR and CO oxidation and also CO tolerance.

The ability to tailor the structure of the electrocatalyst is then significant to such a study. Major efforts in this area are thus dedicated to synthesize more durable and also electrochemically better performing catalysts while restraining the platinum content. The capability to precisely tailor the architecture of the electrocatalyst through optimized synthesis routes may thus serve as a path to reduce the cost of current Pt/C electrocatalysts, and thus to optimize Pt dispersion and significantly reduce the required Pt loading while maintaining high performance [72][73][74].

1.4 Degradation of Pt/C catalysts

Degradation of the electrocatalyst is the phenomena where the structure of the catalyst is permanently damaged due to active material loss and/or active material or support deformation. These phenomena lead to impaired catalytic activity and thus the fuel cell performance. It is naturally important to understand the root causes for the degradations in order to find the solutions for more durable fuel cells. Degradation of Pt/C catalysts may thus be associated with either the Pt nanoparticles themselves or with the carbon support. The degradation may be related to operational conditions, impurities or contamination as outlined below.

1.4.1 Degradation related to operational conditions

The low-pH, relatively high temperature and dynamic loads together with an oxidizing or reducing environment pave the way for different degradation mechanisms in the PEMFCs. Critical operational situations include subfreezing conditions, potential cycling, fuel starvation, start/stop cycling, and changes in temperature and relative humidity [75]. In connection with Pt nanoparticles, there are important factors that affect durability, including sintering and migration of Pt particles on the carbon support, dissolution and detachment of Pt particles into electrolyte, and carbon support corrosion [35][76]. Coarsening in catalyst particles were suggested to be controlled by different mechanisms. Watanabe et al. [77] suggested that the coarsening mechanism for Pt and Pt alloy might be Ostwald ripening where small Pt nanoparticles may dissolve in the ionomer phase and subsequently redeposit on the surface of large particles' surface and finally leading to growth in particle size. Akita et al. [78] also suggested in an interesting analytical TEM study of degraded Pt catalysts that the dissolved Pt species may diffuse into the ionomer phase and then precipitate in the membrane while the reduction of Pt ions causes by the crossover hydrogen from the anode side, which dramatically decreases membrane stability. It is also suggested that a typical distribution of particles sizes with a maximum at small particles and a tail towards the large particles as a result of random cluster-cluster collisions can lead to agglomeration of platinum particles [79]. The minimization of the Gibbs free energy for Pt clusters was also suggested to cause the particle growth [80]. In contrast with the previous mechanism, here the particle size distribution is characterized by a tail towards the small particles and a maximum at large particles. Coarsening of the catalyst as a result of particle movement and coalescence on the carbon support can cause the reduction of electrochemically active surface area (ESA) [81][82]. The formation of metal oxide at the electrodes was also suggested to cause an increase in particle size and a decrease in catalytic activity and durability [83]. There is still no consensus on what mechanism is dominant in different operational conditions and it is an open research area [84].

Another vital issue concerning the durability of electrocatalyst and catalyst layer is carbon corrosion [85]. Carbon corrosion generally occurs according to the following process:

$$C + 2H_2O \rightarrow CO_2 + 4H^+ + 4e^- \quad E^0 = 0.207\ V_{RHE} \qquad (1\text{-}19)$$

The process is thermodynamically feasible only above 0.2 V at standard condition, however the carbon oxidation at lower potentials (less than 0.55 V vs RHE) is negligible in fuel cell operational conditions [86]. The corrosion has been shown to significantly increase during start-up and shut-down processes in PEMFC [87]. There are different mitigation strategies suggested in literature as remedy to such corrosion. Anode, the source of creating high potentials leading to carbon corrosion on the cathode side, was recommended to be purged during shut-down/start-up. Ofstad et al. suggested that degradation associated with shut-down/start-up may be limited to certain extent by air-purging anode with maximal purge rate and minimal relative humidity [88].

Fuel starvation was also addressed in the literature as a major carbon corrosion source. Taniguchi et al. reported that even temporary fuel starvation causes severe and irreversible impairment to the PEMFC's electrocatalyst [89].

1.4.2 Degradation related to impurities

According to Cheng et al. [90] the degradation of Pt catalysts may be exacerbated in the presence of impurities. Typical impurities found in the fuel include CO that is explained above, CO_2, NH_3 and H_2S and CH_4 that come mainly from the reformate hydrogen. In addition to these contaminations, chloride also has been studied in terms of the link of its presence to fuel cell catalyst stability. For example Briskeby [91] et al. reported that the activity towards oxygen reduction may be reduced by a factor of seven when chloride was present at concentrations up to only 140 ppm. Platinum corrosion in their study was severe at high potential, presumably accelerated by potential cycling and greatly enhanced by mass transport.

It is important to note that the degradation process containing both catalyst metal (Pt or Pt alloys) and carbon support aspects is a complex process and the affecting factors in each part may affect the others. For instance it has been shown that Pt catalyzes carbon corrosion [92][93] and also the oxidation of carbon speeds up the Pt sintering [59]. This is also the case for the degradation protocol used in this thesis consisted of 100 cycles of the cathode potential between 0.6-1.5 V vs. RHE, where in many cases both degradation aspects are involved.

1.5 Motivation for the thesis

The dispersion of Pt nanoparticles is expected to influence the activity and durability of electrodes in PEMFCs. A main objective of this work has then been to develop the understanding of the effect of Pt particle dispersion on activity and durability of the Pt/C electrocatalysts. In view of the importance of the issue of degradation for PEM fuel cells and the state of the art understanding at the time the work commenced, investigations into how different catalyst structures act electrochemically in different simulated practical scenarios such as degradation protocol and CO exposure appeared appropriate. Our emphasis has been on factors such as the durability of isolated, aggregated and film-coat Pt nanoparticles on carbon against degradation, the CO-tolerance of aggregated and isolated Pt particles, and the effect of catalyst layer thickness on fuel cell activity and durability.

1.6 Thesis organization

- An introduction to the subject is given in Chapter 1.
- Methodology and a brief introduction to the experimental work is presented in Chapter 2.
- The synthesis techniques used in the study and tailoring the electrocatalyst architecture are formulated in Chapter 3.
- In Chapter 4 the effect of catalyst later thickness in performance and durability of a fuel cell equipped with individual Pt particle electrocatalyst is studied.
- Chapter 5 deals with three types of Pt nanoparticle dispersion of the electrocatalyst and their influence on fuel cell performance.
- Chapter 6 presents the results for CO-dependent fuel cell performance of both isolated and aggregated platinum nanoparticles supported on carbon black.
- In Chapter 7 a dynamic EIS study of Pt/C-based MEAs with aggregated Pt particles subjected to cycling protocols are presented.
- Conclusions and recommendations for future work are given in Chapter 8.

1.7 Publications

Peer reviewed publications and intended manuscripts for publication in peer reviewed journals in the area of fuel cell and with NTNU affiliation are listed here. The publications in section 1.7.1 were used in this thesis.

1.7.1 Publications used in the thesis

- **Mahdi Darab**, José Luis Gómez de la Fuente, Navaneethan Muthuswamy, De Chen, Magnus Rønning, Magnus Skinlo Thomassen and Svein Sunde, "Architecture design for nanostructured Pt/C electrocatalysts via optimizing synthesis conditions", manuscript intended for publication.
- **Mahdi Darab**, Alejandro Oyarce, Magnus Skinlo Thomassen, Göran Lindbergh and Svein Sunde, "The influence of catalyst layer thickness on the performance and degradation of PEM fuel cell cathodes", manuscript intended for publication.
- **Mahdi Darab**, José Luis Gómez de la Fuente, Magnus Skinlo Thomassen and Svein Sunde, "Pt nanoparticles dispersion influence on fuel cell performance," ECS Transactions., vol. 50, no. 2, pp. 1353–1367, 2012.
- **Mahdi Darab**, Magnus Skinlo Thomassen and Svein Sunde, "CO-dependent fuel cell performance of isolated and aggregated platinum nanoparticles supported on carbon black", manuscript intended for publication.
- **Mahdi Darab**, Per Kristian Dahlstrøm, Magnus Skinlo Thomassen, Frode Seland and Svein Sunde, "Dynamic electrochemical impedance spectroscopy of Pt/C-based membrane-electrode assemblies subjected to cycling protocols", Journal of Power Sources, vol. 242, pp. 447–454, 2013.

1.7.2 Publications not included

- "Graphitised carbon nanofibres as catalyst support for PEMFC," Fuel Cells, vol. 11, no. 6, pp. 715–725, 2011.
- "The Effect of synthesis methods on the electrochemical activity and durability of carbon supported platinum nanoparticles as electrocatalysts for PEMFC", ECS Transactions, vol. 41, no. 1, pp. 1067–1078, 2011.

Chapter 2

Methodology

In this chapter the procedure for synthesizing electrocatalysts, the physicochemical characterization, making electrodes and ex-situ electrochemical testing, fabricating MEAs, in-situ electrochemical and fuel cell testing with some of the details of the following steps are presented.

2.1 Experimental approach

In this PhD project it was aimed to fabricate active and highly durable electrocatalysts for PEMFCs and to understand the role of particle dispersion in catalysts on fuel cell performance and durability. This naturally includes synthesizing the Pt/C electrocatalyst and the relevant physicochemical and ex-situ electrochemical characterizations, preparation of catalyst ink, fabrication of MEA, and testing MEAs inside a fuel cell (in-situ).

Figure 2-1 shows an overview of the steps taken in the experimental part of the project.

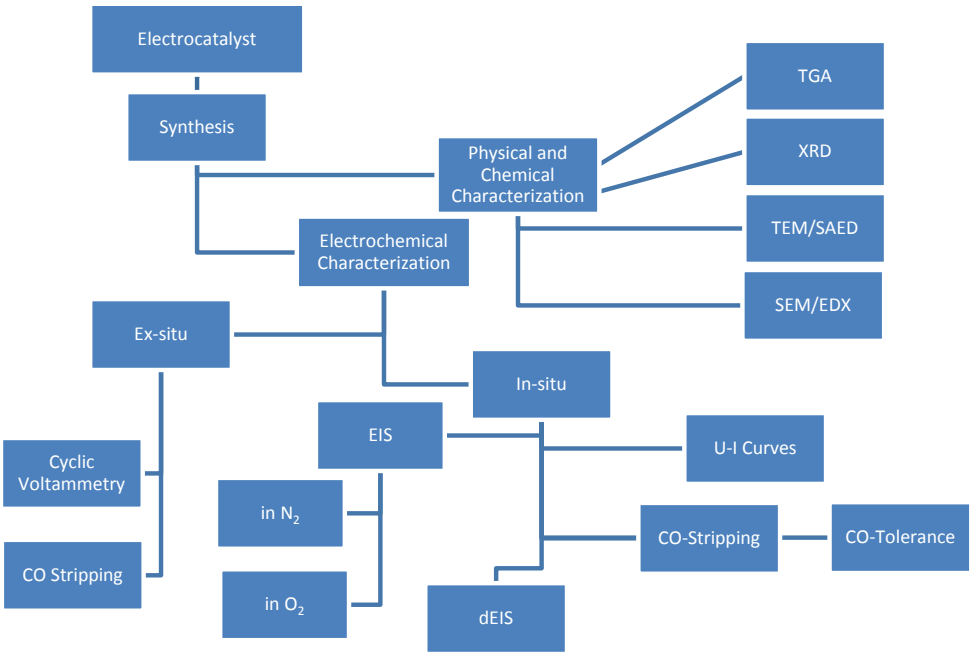

FIGURE 2-1: Overview of the experimental approach in the project

2.2 Synthesis and preparation of carbon-supported Pt catalysts

The first step in this thesis was to synthesize heterogeneous catalysts for fuel cell applications, aiming to attach the active phase (platinum) onto the support (carbon). Preparation techniques developed for fuel cell catalysts include methods based on ultrasound [94], micro dispersion [95], co-precipitation [96], and ion exchange and chemical methods [97][98]. The polyol method has also received a special attention and been extensively studied as a proper choice of synthesis technique for Pt/C catalysts [99][100][101][102][103].

In this thesis there were basically three varieties of the polyol method examined and an impregnation technique was also applied as a benchmark as outlined below.

2.2.1 Wet impregnation (WI)

Impregnation is a synthesis technique for preparing heterogeneous catalysts including Pt/C based on ion-exchange and adsorption of precursors and the interaction of the precursor with the support material is dominant. In this method a porous support is exposed to a solution containing the metal precursors, and the support material thus gets "impregnated" by the metallic particles.

Impregnation comes in two varieties. In the dry impregnation technique an exact amount of the solution required to fill in the pore volumes of the support material is provided. In the wet impregnation method an excess amount of the solution containing the metal precursor is used, and it is only the solubility of the metal that decides the amount of the solution applied and not the pore volume of the support as in dry impregnation. In this technique, reducing agents can also be used to facilitate reduction of the metal precursors on the support surface. The impregnation method used in this study was wet type.

In the wet impregnation technique in this study the support material without pretreatment was dissolved in a mixture of isopropanol/water and was heated under reflux. The solution was stirred and the platinic acid added drop-wise. Aqueous sodium borohydride in isopropanol was then added and the final pH became detectably basic. Sodium borohydride acts as a strong reducing agent in this method to reduce platinum particles from the platinic acid.

2.2.2 Polyol (P)

Polyol is the synthesis of metal-containing compounds in ethylene glycol (EG). The EG in this technique acts simultaneously as both the solvent and reducing agent [104]. The attraction of the polyol technique includes the good command over the particle size of the resulting materials. The fact that polyol technique does not require additional stabilizers also contributed to their popularity. High metal loadings can be reached with high purity, but at the cost of being a time consuming and sensitive preparation technique [105]. In this method synthesis conditions are very important in order to achieve the structure-tailored catalysts. For example it was found that lower pH values at the final step of the synthesis play a central role in forming small isolated Pt particles. This is related to the structure of ethylene glycol and the fact that while Pt salt is reduced, EG in turn is oxidized to mainly glycolic acid or in a certain pH range, its onion, glycolate. It was shown that the low pH in synthesis solution is in favor of EG oxidation to glycolic acid and therefore strong reduction of metal precursor while high pH favors glycolate formation and thus stabilization effect in the solution. It was also found that the optimum pH for the reduction of metals in desired form and size is somewhere in between the high and low pH limit, for example in the pH range of 2-6 in the reference [104].

In the polyol method applied in this thesis, NaOH was dissolved in EG and then the non-pretreated support materials were added. Platinic acid dissolved in EG was then added to the solution while keeping the nitrogen atmosphere to the mixture. The temperature was increased for a while after which the solution was allowed to cool down and the catalyst was dried.

2.2.3 Modified polyol (MP)

The modified polyol employed was similar to the polyol method described above. However, the processing temperature, the amount of reducing agent and the duration of reduction were modified. Some of the washing steps at the end of the synthesis were also skipped.

2.2.4 Adsorption polyol (AP)

The adsorption polyol method shares the principle with conventional polyol in terms of having EG as the solvent and reducing media at the same time. However, the in the adsorption polyol technique the metallic particle are produced in a separate stage prior to the addition of the support. Thus, particle shape and size are expected to be controlled primarily by the polyol chemistry per se and be less influenced by the properties of the the support material. The method assumes that the pre-formed colloidal particles can efficiently be adsorbed on to the support in a final stage. The control of synthesis parameters especially pH is of high importance in the stage where the metallic deposition takes place. The acidity of the solution at the final stage of anchorage decides the particle dispersion on the support. In the AP technique used in this thesis, platinum nanoparticles were prepared first with the precursor dissolved in EG followed by addition of NaOH already dissolved in EG to maintain the pH slightly basic. The mixture was subsequently heated under N_2 flow.

In the next step the Pt nanoparticles were deposited on carbon supports in accordance to [105][106]. The carbon support was pretreated by adding the carbon support material to EG and ultrasonicating the mixture. So the main difference here was that the metal colloidal solution was added to the carbon-EG suspension separately. The pH of the mixture was monitored constantly and adjusted to be highly acidic.

2.3 Physicochemical characterization

A set of physicochemical characterization was performed on the synthesized catalysts mainly in order to assess the architecture and chemical composition of the samples.

2.3.1 TGA

Thermogravimetric analysis (TGA) is a thermal analysis technique where changes in the mass of the sample are measured as a function of temperature, typically with constant heating rate under a controlled atmosphere. TGA can be performed with constant-temperature mode in which the mass or other parameters are monitored as a function of time.

In this thesis TGA was used to determine changes in the mass of the synthesized electrocatalysts as a function of temperature under a controlled atmosphere. The analyzer consisted of a precise balance with a pan loaded with the sample undergoing the programmed heating.

TGA was primarily used to estimate the amount of metal (loading) in the synthesized electrocatalysts by weighting the residue after burning the carbon content. The estimated value would then be compared to the target loading according to synthesis reaction stoichiometry.

A secondary purpose of TGA was also to determine the resistivity of the Pt/C catalysts against oxidation and studying catalytic oxidation of each sample and investigating whether the platinum content could be of assistance in such reaction.

Figure 2-2 shows an example of TGA results for selected electrocatalysts used in this thesis with different metal loading.

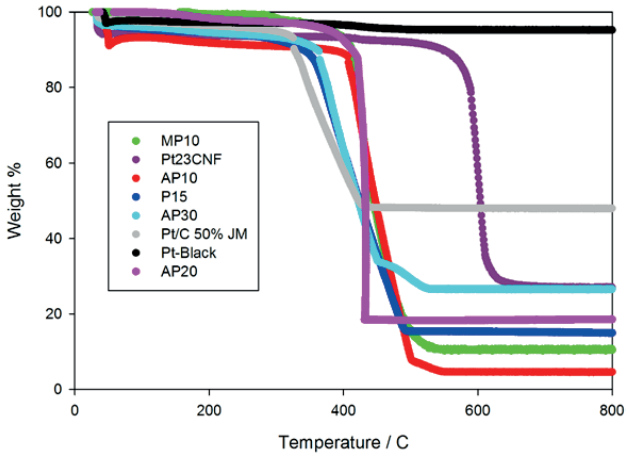

FIGURE 2-2: TGA results for some of the synthesized electrocatalysts, ranging from 10 to 30% Pt on carbon support, Pt black (unsupported) and commercial 50% Pt supported on carbon. Conditions: atmosphere: air, flow rate: 100 $mlmin^{-1}$, T range: room temperature to 800 °C, heating ramp: 10 $Cmin^{-1}$

2.3.2 XRD

X-ray powder diffraction (XRD) is a phase identification of a crystalline material. The method is based on exposing a solid powdered sample to X-rays of wavelengths of the order of angstroms, i.e. of the same order of magnitude as interatomic distances in solids, and measuring the intensity of the X-rays as they emerge from the sample as a function of the exit angle. Due to diffraction between X-rays scattered from different lattice planes in the solid the intensity as a function of exit angle will show large variations from close to zero intensity to very high intensities. For large crystallites and the high intensity regions take the shape of high narrow peaks separated by the close-to-zero intensity regions. The most important information is the exit (diffraction) angles at which the X-rays emerge from the powder sample, from which an identification of the crystal structure is frequently possible. Additional information may be found from the intensity of the peaks (peak heights) and their widths (usually the full width at half maximum, FWHM).

The technique is executed with an instrument called diffractometer. Normally X-ray diffractometers consist of three parts: an X-ray tube, an X-ray detector and a sample holder. Heating a filament in the cathode ray tube, electrons are produced and accelerated toward a target by applying a voltage, and are bombarded on the target material, such as copper. As a result of high-energy collision of the electrons and crystalline materials, characteristic X-rays are produced. The monochromatic X-rays will then be collimated and directed onto the sample which is rotating and the intensity of the reflected X-rays from the sample is recorded. At this point, if the parameters of the incident X-rays satisfy the Bragg equation, a constructive interference takes place and a jump in intensity (peak) is recorded.

Eq. (2-1) is known as Bragg's equation:

$$2d\sin\theta = n\lambda \qquad (2\text{-}1)$$

where d is the spacing between the planes in the atomic lattice, n is an integer, λ is the wavelength of incident wave, and θ is the angle between the incident ray and the scattering planes.

XRD as a fast-response, non-destructive and affordable technique was occasionally utilized in this work to first verify the crystalline structure of the electrocatalysts and then to estimate the crystallite size of the samples using Scherrer equation:

$$Lp = \frac{K\lambda}{\beta_{1/2}\cos\theta} \qquad (2\text{-}2)$$

Here Lp is the mean crystallite length (which may be equal to or less than the grain size), K is dimensionless shape factor with values in the range of $0.89<K<1$, λ is the

wavelength of the incident X-ray, $\beta_{1/2}$ is the width of the peak at half maximum intensity of a specific phase and θ is the angle between the incident ray and the scattering planes as seen in Eq. (2-1).

Figure 2-3 presents a typical XRD pattern for a synthesized Pt/C electrocatalyst.

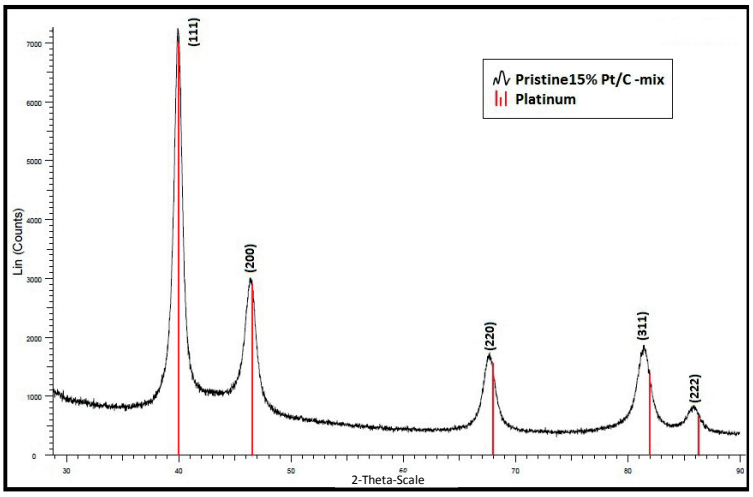

FIGURE 2-3: A typical XRD pattern of a synthesized Pt/C with the assigned Pt-indices as indicated in the figure.

2.3.3 SEM/EDX

Scanning electron microscopy (SEM) is one of electron microscopic techniques in which a focused beam of high-energy electrons is used to scan and image solid samples.

A typical SEM apparatus consists of a source of electrons, a top-down column to direct electrons with electromagnetic lenses, an electron detector, a sample chamber, and a display to see the images. The produced electrons at the source are accelerated top-down through the column and go through electromagnetic lenses to become an extremely focused beam of electrons. The beam will then collide with the sample's surface at the sample chamber. The chamber is usually in vacuum state using a fine pumping system. The scan coil controls the location of the focused electron beam on the surface of the sample and it lets the beam be scanned over the surface. As a result of this bombardment and the consequent interaction between electrons and the sample, a number of signals are generated that are carrying information about the surface and will be analyzed and converted to 2D images by the detector.

SEM systems frequently include an in-built Energy-dispersive X-ray spectroscopy (EDX) apparatus with which it is a possible to obtain compositional information of selected spots in addition to topography and images of the surface. X-rays are one type of signals

emitted as a result of electron bombardment on the sample. In the EDX system, the energy of these X-rays is analyzed for element determination. The electron beam that hits the surface causes ejection of electrons, leaving the surface in an excited state. These emerging vacancies are then filled with higher state electrons, and an X-ray is emitted to compensate for the difference in energy between the two electron states. The detector in the EDX system thus measures the intensity of the X-rays versus their energy. EDX is typically equipped with solid state detectors typically made of Si(Li) or Ge(Li). When the emitted X-ray collides with the detector, a charge pulse proportional to the energy of the X-ray is generated. Using a charge-sensitive amplifier, the charge pulse is converted to a potential pulse and the proportionality of the X-ray energy is still maintained. The pulse is then sorted by their potentials through a multichannel analyzer. Now the energy for each emitted X-ray is determined based on the potential measurement and it will be presented as a function of abundance which is further used for elemental analysis of the selected spots.

SEM and EDX were used often in the early stage of this research where the synthesized materials were examined to locate Pt particles and carbon materials. SEM is a fairly low cost microscopy method and could be very useful in micro-structural studies, but since the resolution required for molecular-size investigation on synthesized catalysts was difficult to gain by SEM, it was replaced by more suitable techniques in the later stages. EDX was of assistance to check the compositional homogeny on selected spots on the catalysts. In-built EDX features were also utilized in high resolution transmission electron microscopy tasks to ensure that the right spot is taken for imaging.

In addition to studying on the catalyst material, SEM was also employed in the studies on the thickness of CCL in Chapter 4. The SEM images before and after the accelerated degradation protocol provided valuable structural information of the degradation process.

Figure 2-4 presents a set of typical low and high magnification SEM pictures of catalysts materials.

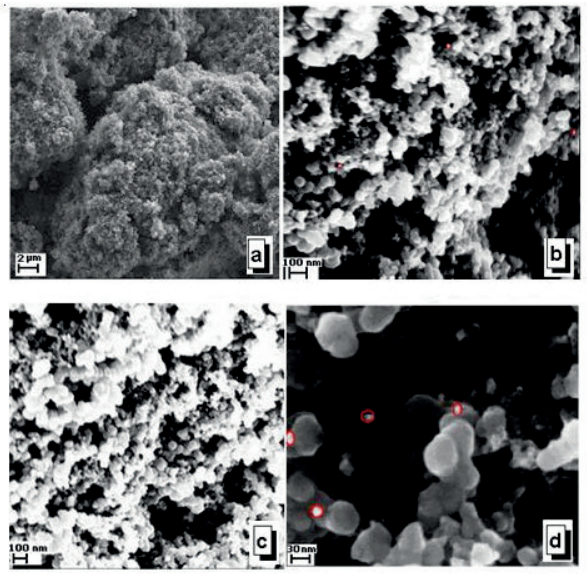

FIGURE 2-4: a) low magnification and b) high magnification SEM images of 10% Pt/C sample synthesized by wet impregnation and c) low and d) high magnification SEM images of 20% Pt/C sample synthesized by polyol.

2.3.4 TEM/SAED

Transmission electron microscopy (TEM) is similar to optical microscopy with the difference that electrons are used instead of visible light beams. With much lower wavelength in electrons comparing to visible light, the limitations for resolving small features is drastically improved in TEM comparing to light microscopy.

TEM is capable of projecting images with 1k to 1000k magnification and less than 1 nm resolution. In a typical TEM system, an electron gun (source of electron) produces high-energy electrons that will travel down the microscope column in vacuum. The electrons are then focused into a very thin beam using electromagnetic lenses. The beam will then be transmitted through the thin sample. When the beam hits the sample, some of the electrons will be scattered from the beam, but the electrons that are not scattered will collide with a fluorescent screen at the bottom of the microscope and form the "bright-field" TEM images which are the most common type. The scattered electrons will be also collected to obtain "dark-field" images. The beam of scattered electrons has heavily interacted with the sample and contains useful information such as crystal defects, stacking faults and particle size that can be achieved from the dark-field images.

TEM images, either bright or dark field, with different level of brightness in different spots are then sent to the image analysis part of the microspore that is coupled with a

computer. The darker spots in the bright-field TEM image is the more dense parts of the material where the electron transmission was hindered, likewise, the lighter sections are corresponding to less dense areas.

Sample preparation is a vital and sensitive task for TEM imaging. One needs to make the sample as "thin" as practically achievable, allowing the electrons to transmit through. For example in case of Pt/C electrocatalysts, a very dilute solution of the catalysts dissolved in alcohol and poured as a droplet on a metallic grid can be used for TEM imaging.

TEM was the cornerstone of physical characterization of the catalysts where we had the possibility to visually validate the proposed structure, Pt particle size and especially particle dispersion over the carbon support. TEM imaging is used for the data reported in Chapter 3, Chapter 4, Chapter 5, Chapter 6 and Chapter 7. Figure 2-5 shows a typical bright-field TEM image for a Pt supported on carbon black.

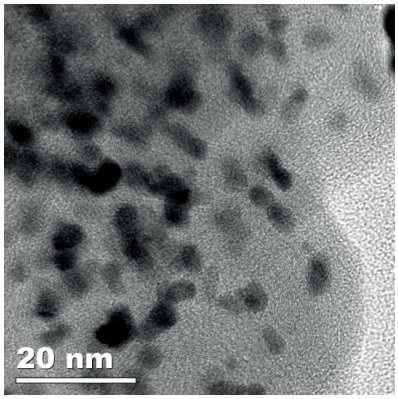

FIGURE 2-5: A typical bright-field TEM image of Pt nanoparticles supported on carbon black.

Secondary X-ray emerging from the sample as a result of the collision with the sample's surface can be collected and analyzed inside the transmission electron microscope with the module of SAED (selected area electron diffraction). In this work SAED was performed while taking TEM images of degraded electrocatalyst samples. The robust and on-site crystallographic experimental technique was informative for studying the crystalline structure of the samples subjected to degradation protocol.

2.4 Ex-situ electrochemical characterization

2.4.1 Cyclic voltammetry and CO stripping

Cyclic voltammetry (CV) is probably the most used primarily mechanistic investigations to determine kinetic parameters in electrochemical reactions [107]. In this technique, a potential is applied to the working electrode and the output current is recorded as a function of applied potential. Then the direction of the potential sweep is revered at the end of the scan and it will return to the initial potential again. The sweep rates employed in typical CV experiments are ranged from a few mVs^{-1} to a few hundred Vs^{-1}.

CO stripping voltammetry is a method to study the surface properties of electrode. In this method the electrolyte is sparged with CO resulting in its adsorption at the electrode surface. The CO is subsequently removed from the bulk solution by sparging inert gas such as Ar in the next step. This way there is very little dissolved CO remaining and the majority of CO content in the system is the CO adsorbed on electrode. The CO can be then oxidized electrochemically at a certain potential and be stripped off. Such potential is a finger print for that special sample and the CO electrooxidation peak shape, position and intensity contain valuable information of surface properties.

CV and CO stripping were important parts of the characterization tasks in this thesis and were used in Chapter 3, Chapter 5 and Chapter 7. CO is believed to be one of the appropriate choices of adsorbates [69][108] for the determination of the electrochemically active surface area (ESA) of Pt/C PEM fuel cell electrodes, the CO stripping voltammetry was used in this work to both estimate the ESA and detect the aggregations.

To estimate the ESA the process of CO oxidation to CO_2 is usually considered to involve two electrons as shown here:

$$CO_{ads} + H_2O \rightarrow CO_2 + 2H^+ + 2e^- \qquad (2\text{-}3)$$

Assuming that CO is linearly bound to the catalyst surface as one CO molecule per Pt atom (Pt-CO_{ads}), the charge required to strip the entire CO layer off the electrode is equal to 420 $\mu C\ cm^{-2}$. The ESA can then be calculated from Eq. (2-4) using the total charge transferred during the CO electrooxidation process [109][110].

$$ESA_{CO}(cm^2 g^{-1}) = \frac{Q_{CO}(mC)}{0.420(mC cm^{-2}) \times W_{Pt}(g)} \qquad (2\text{-}4)$$

Here Q_{CO} is the CO stripping charge and W_{Pt} is the mass of the catalyst [111].

2.5 In-situ electrochemical characterization

The samples that were shown promising in the ex-situ electrochemical characterization were used to fabricate MEAs and were consequently tested in a fuel cell set-up.

2.5.1 Preparation

2.5.1.1 MEA fabrication

The catalyst ink consisting of the catalyst powder, Nafion® solution, Milli-Q water and isopropanol was prepared by mixing the materials in certain portions followed by ultrasonication. The catalyst ink was then evenly sprayed on a commercial membrane at elevated temperature with an airbrush to build the working electrode (WE). Commercial electrodes used as combined counter and reference electrode (CE/RE). The commercial electrode was then hot-pressed on the sprayed membrane with catalyst ink and a commercial gas diffusion layer was mounted on the WE finalizing the MEA fabrication.

2.5.1.2 Cell assembly

PEM single cells, with an active area of 1 cm^2 (for the tests in Chapter 4) and 5 cm^2 for the rest of the chapters, were assembled from the selected MEA fabricated of the already characterized electrocatalysts. The cells were symmetrically tightened using eight stainless steel screws. Electrical resistance of the cell and the torque for the screws were optimized prior to start the tests to ensure that short-circuits and also unnecessary physical tensions on the samples were avoided. The temperature and humidification as well as sealing pressure applied to the MEAs were carefully monitored and controlled in the course of the in-situ experiments.

2.5.2 In-situ CVs and CO stripping

In in-situ CVs, the working electrode is covered by an inert gas such as Ar and the other electrode in the fuel cell serving as both counter and reference electrode is exposed to hydrogen. The potential is then cycled between a lower vertex potential (usually 0 V) and a higher vertex potential (usually 0.7 V) with a sweep rate of 10-50 mVs^{-1}.

The results from ex-situ and in-situ voltammetry are not necessarily identical due to the difference in experimental conditions between the classical three-neck liquid electrolyte cell and PEM single cell, but the trends in important electrochemical characteristics should be naturally compatible in both cases.

2.5.3 Polarization curves

Polarization curve is typically a plot of fuel cell voltage as a function of output current density in the (pseudo-) steady state. In this work the curves were acquired under constant temperature, inlet humidity and flow rates of the reactants, pure oxygen in

cathode and pure hydrogen in anode. Recording of polarization curves frequently starts from the open circuit voltage as the maximum practical cell voltage, which is still less than the theoretical "no loss" voltage of 1.23 V for overall water formation reaction in fuel cell. Then in the activation region, there is a rapid fall in voltage until the curve enters the ohmic region. Here the voltage decreases more gradually and the curve is fairly linear. The last region of the polarization curve is the mass transport where a rapid fall at higher current densities forming a knee shape and a cut-off at the end of the curve. Polarization curves were widely used in this work in Chapter 4, Chapter 5, Chapter 6 and Chapter 7. Sometimes to study the mass transport properties of the electrodes, instead of pure oxygen, diluted oxygen were utilized such as in the data reported in Chapter 4. The information about the activity and probable losses provided by the polarization curves do not specify the exact source of the cell that is accountable for the actual flaw. In practice a comprehensive interpretation of the irreversible losses needs a combination of polarization curves with supplementary technique such as in-situ CO stripping and impedance spectroscopy.

2.5.3.1 Cell performance in presence of CO

Considering the importance of the activity and durability issues associated with impurities present in the feed streams of fuel cell, especially CO, there are different techniques developed to study such effects. One simple method is to keep cell at a constant current density with pure gases flowing on the electrodes and subsequently switch the pure hydrogen on anode with a stream of CO at ppm level concentration and finally switching back to the pure hydrogen on anode side. Recording the cell voltage in such circumstances will provide a measure of the effect of CO on fuel cell performance. Using this technique it is also possible to measure how recoverable an electrocatalyst is against CO poisoning where the cell voltages under CO/H_2 and under pure H_2 are compared.

In a separate but similar method polarization curves were collected under pure oxygen on cathode and pure hydrogen and then a mixture of carbon monoxide and hydrogen. This experiment was performed in Chapter 6 to compare the cell performance under slight CO presence with that of pure hydrogen. Electrocatalysts with different Pt particle dispersion were tested by this experiment.

2.5.4 Electrochemical impedance spectroscopy

Electrochemical impedance spectroscopy (EIS) is a diagnosis tool for studying many electrochemical system including fuel cells [112][113]. In the EIS technique a small sinusoidal AC potential (or current) as a perturbation signal is applied to the system (here the fuel cell) and the current (or potential) response is measured. Using this technique the frequency dependence of the impedance of the system can be studied.

The expression for impedance composes of a real and an imaginary part. Normally the real part is plotted on the x-axis and the imaginary part on the y-axis of a chart frequently referred to as "Nyquist plot" (or impedance-plane plot). Each point on the Nyquist plot represents the impedance of the item under test at a unique frequency. In Nyquist plot low frequency data are presented on the right side of the plot and higher frequencies are located on the left side. This presentation of impedance spectra is used in this thesis in Chapter 4 and Chapter 7. Other forms of representation include capacitance plots, Bode diagrams and admittance plots. These were, however, not used in the present work.

The most straightforward application of EIS is for estimation of the ohmic and charge transfer resistances [114][115][116][117], for which the technique is now routinely used. For this purpose the ohmic resistance of the system is taken from the intercept of the experimental curve with the real axis in the high-frequency end of the spectrum.

EIS data analysis also offers information complementary to that obtained from polarization curves and cyclic voltammetry alone, such as information relating to electrode structure and electrode reaction mechanisms. EIS then provides dynamic information, which is not available in polarization curves, and often with a higher resolution than that offered by cyclic voltammetry since in EIS studies, different contributing processes can be sorted according to their corresponding frequencies [112][118]. Different types of EIS measurements were used in this thesis as following.

- High frequency resistance (HFR) of the fuel cell was utilized to correct the recorded polarization curves for iR-drop in Chapter 4.
- Polarization and solution resistances were also estimated from the EIS in O_2 which was performed in concentrated and diluted oxygen to also study the diffusional properties of the CCLs.
- EIS in N_2 were carried out to estimate the conductivity of the CCL ionomer. EIS spectra were analyzed according to the method proposed by Jaouen [119].

In this thesis EIS spectra were only analyzed qualitatively even though impedance data are typically fitted to an equivalent electrical circuit model to analogically obtain kinetic information and mass-transport information.

2.5.4.1 dEIS

Although EIS is normally performed under steady-state conditions, in dynamical impedance spectroscopy (dEIS) [120] the spectra are collected also for systems under dynamic conditions. Thus, a multi-sine wave consisting of all frequencies of interest are superimposed on a dc potential scan. This provides the possibility to collect kinetic information on transient surfaces, which is not available in EIS under steady-state conditions. Another importance of this method is that the polarization curves can be extracted from the measurements at the same time with the impedance spectra. This

extracted from the measurements at the same time with the impedance spectra. This gives the possibility for a direct correlation between the impedance spectra and features in the fuel cell performance. This method was used in Chapter 7 to detect slight alteration of an agglomeration containing electrocatalyst subjected to cycling, the changes that were not possible to observe in other electrochemical techniques.

2.5.5 Accelerated degradation test

The degradation phenomena in fuel cell are not instantaneous and a relatively long time may be required a relatively long time before observing changes in characteristics of a fuel cell due to catalyst degradation. Being not practical to have such a long interval (as much as the life time of a fuel cell) in research projects, accelerated protocols are invented to physically simulate the degradation of fuel cell components.

Aging with potential holds and degradation with potential cycling are two common methods widely used now. The gases that are fed into fuel cell in both cases are usually the same as those of polarization curve experiments, however some variations are applicable. Potentiostatic holds can be operated at high or low potential depending on the degradation mechanism of interest with the duration of few to several hundreds of hour. The strong point of this method is to be able to isolate a degradation mechanism based on the potential but on the other hand the method is not always effective to get proper results in a reasonable time.

In potential cycling the fuel cell is normally operated in hundred cycles between the min and max potential and a sweep rate of around 50 mVs^{-1}. The possibility to single out a degradation mechanism is less in potential cycling comparing to potentiostatic holds. Potential cycling is, however, much quicker than potentiostatic holds to make a significant modification on fuel cell components.

In this work potential cycling type of ADT was applied with 100 potential cycles between 0.6 and 1.5 V vs. RHE. The ADT was performed with pure O_2 on cathode and pure hydrogen on anode for the tests in Chapter 4. The technique was also tried with harmix (5% H_2 balanced with Ar) on anode side and nitrogen on cathode side as an attempt to isolate only Pt degradation phenomena and to harm the carbon support as low as possible for the results reported in Chapter 5 and Chapter 7.

All the in-situ experiments performed on pristine samples were repeated on the same samples that underwent an accelerated degradation test (ADT). In some cases post mortem analysis was also carried out such as SEM and TEM imaging of the degraded samples in Chapter 4 and Chapter 7.

Chapter 3

Control over Particle Dispersion

This chapter describes how the synthesis conditions have been optimized in order to have the desired architecture of the nanostructured Pt/C electrocatalysts. The chapter is a manuscript intended for publication.

3.1 Introduction

Efficient electrocatalyst is a critical component of fuel cells and has a direct bearing on the overall efficiency of the cell [121][122][123]. The difficulty with efficiency and affordability of the electrocatalysts varies with fuel cell type. This problem is particularly challenging for low temperature fuel cells operating below 100 °C and in an acidic medium, such as the proton exchange membrane fuel cell (PEMFC), and has therefore gained a specific attention from the electrochemical community [124][125]. Although the new generations of electrocatalysts with low-cost materials are emerging [24][25][26][27][28], nanoparticles of platinum and its alloys deposited on various carbon structures (Pt/C) still seem to be the focus in PEMFC research [31][32][33].

Not only chemical composition but also the structure of the Pt/C electrocatalysts is important from at least two points of view: i) the effect of the structure on activity and stability of the electrocatalysts ii) the utilization of the costly platinum and therefore the

overall cost of the different catalyst architectures. Major efforts in this area is thus dedicated to synthesize more durable and also electrochemically better performing catalysts while restraining the platinum content [126][127]. The ability to precisely manipulate the architecture of the electrocatalyst through optimized synthesis routes may thus serve as a path to reduce the cost of current Pt/C electrocatalysts, and thus to optimize Pt dispersion and significantly reduce the required Pt loading while maintaining high performance [72][73][74]. For instance, in the case of the cathode reaction in PEMFCs much research has gone into overcome the sluggish kinetics of the oxygen reduction reaction (ORR) through producing electrocatalysts with high particle dispersion and a reasonable metal loading with a controlled particle size and structural features [125][128][129]. The sensitivity of ORR towards structure and the so-called particle size effect exert a significant impact on fundamental ORR research [130].

In addition to the ORR the architecture dependence of electrocatalyst is also the case for carbon monoxide (CO) bulk oxidation, which is another important process when it comes to the operation of PEMFCs under working conditions. On one hand the presence of hydroxyl (OH) species promotes Langmuir-Hinshelwood CO bulk oxidation, and a decrease in particle size increases the specific activity for CO oxidation since oxygen-containing species appears to adsorb more strongly on small particles than on large. On the other hand when the coverage of oxygenated species increases on the surface the specific activity of the electrocatalyst for ORR decreases [131] much through the same dependence of the coverage of oxygenated species on particle size. It is also believed that Pt individual nanoparticles are less active in terms of CO monolayer oxidation compared to Pt aggregated nanoparticles since aggregates include large amounts of grain boundaries interconnecting the isolated particles and defect sites which seem to be more active to the reaction [66][67].

These examples present the motivation of structural-related studies on electrocatalysts to understand their effect on some reactions of interest in PEMFCs and the desire to achieve accurate preparation methods for electrocatalysts and thus to optimize architecture and dispersion for Pt/C for PEMFCs.

Among recently developed preparation techniques for fuel cell materials, such methods based on ultrasound [94], micro dispersion [95], co-precipitation [96], and ion exchange and chemical methods [97][98], the polyol method has received a special attention and been extensively studied since it offers a proper control over catalyst structure [99] [100][101][102][103][104]. This method was used in the present work, where ethylene glycol (EG) was utilized as simultaneously solvent and reducing agent for metallic precursors.

Classical wet impregnation method to synthesize Pt/C catalysts that has been available for a long time [132] was also used in this work as a benchmark to examine the quality of the prepared electrocatalysts by polyol.

CO monolayer oxidation ($CO_{ads} + H_2O \rightarrow CO_2 + 2H^+ + 2e^-$) is a widely used test reaction in electrocatalysis [73][133], and was used by Maillard et al. [69] as a method for examining whether the Pt/C catalyst contains aggregated particles. It was also utilized to correlate the Pt particle dispersion with catalytic activity [134]. In this work the CO electrooxidation was assumed to take place mechanistically according to Langmuir-Hinshelwood CO oxidation on Pt [135].

The demonstration of how synthetic method affects the architecture of the electrocatalyst is targeted in this article. We aim to illustrate how the various synthesis techniques and preparation conditions are responsible for high potential single peak (between 0.75 and 0.8 V vs RHE) and peak multiplicity in CO stripping voltammograms for the catalysts with isolated particles solely and aggregation containing samples, respectively. Adsorption polyol will be introduced as a neat route to synthesize agglomeration-free electrocatalysts with pH control.

Using the polyol synthesis techniques outlined below and the information given for the preparation conditions one can achieve a decent control over the architectural features and hence electrochemical characteristics of an electrocatalyst.

3.2 Experimental

3.2.1 Catalyst synthesis

Materials and solvents were obtained from commercial suppliers and were used without further purification. Carbon black (CABOT Corporation), hexachloroplatinic acid (IV) (Johnson Mattey, Pt content: 39.76 %, purity ≥ 99%), sodium borohydride (Fluka Analytical, purity 96%) and isopropanol and acetone in analytical grade were used for the Wet Impregnation (WI) method, while carbon black (Vulcan XC72, CABOT Corporation), few walled carbon nanotubes (grown at Aalto University by chemical vapor deposition of CH_4), hexachloroplatinate (IV) (Johnson Mattey, Pt content: 39.76%, purity ≥ 99%), sodium hydroxide (VMR, purity>99%), ethylene glycol (Sigma-Aldrich purity ≥ 99%) and acetone (analytical grade) were used to synthesize the catalyst by the polyol method. Solutions were diluted with deionized water (18MΩcm conductivity, MilliQ System). The sample Pt on carbon nanofiber (VGCF®-H, Showa Denko Inc.) was also provided by Aalto University.

3.2.1.1 Wet impregnation (WI)

In the wet impregnation technique in this study the support material without pretreatment was dispersed in a mixture of isopropanol/water and was heated at 80 °C under reflux. The solution was stirred and platinic acid added drop-wise to prevent the aggregates from forming immediately. The initial pH at this stage was measured around

4. Aqueous sodium borohydride 1 M in isopropanol was added at this step during which the final pH became detectably basic. The catalyst was collected using filtration and washed several times with water to reach the neutral pH before drying at 90 °C for 480 minutes.

3.2.1.2 Polyol (P)

NaOH was dissolved in ethylene glycol (EG) and then the non-pretreated support materials were added. The solution was kept at 50 °C for 30 minutes. In this technique EG simultaneously acts as solvent and reducing agent [104]. The initial value of pH was measured around 10. Clear yellowish solution of platinic acid in EG was then added to the solution while keeping the nitrogen atmosphere to the mixture. The temperature was increased to 110 °C for 90 minutes, after which the solution was allowed to cool in air. The final pH was measured around 6. After centrifuging, ultrasonic homogenization, and washing with water and acetone, the catalyst was dried at 80 °C for 480 minutes.

3.2.1.3 Modified polyol (MP)

The modified polyol employed is similar to the polyol method described above. However, the maximum temperature was increased to 150 °C rather than the 110 °C employed in the polyol method. The amount of reducing agent was doubled, and the chemicals were mixed differently. Thus, NaOH pellets were dissolved slowly overnight in EG solution under a flow of N_2. Reduction duration was also changed to 3 hours in the modified polyol method, and washing with hot water was avoided. The final pH measured around 4.5; the sample was cooled down to room temperature prior to pH measurement. The solution was cooled down and centrifuged. The catalyst was washed repeatedly with acetone and finally water and dried at 70 °C for 500 minutes.

3.2.1.4 Adsorption polyol (AP)

Platinum nanoparticles were prepared first with 1.0 g of H_2PtCl_6 dissolved in 150 ml of EG followed by addition of 100 ml of 0.5 M NaOH also dissolved in EG to maintain the pH basic. The mixture was subsequently heated at 145 °C for 240 minutes under N_2 flow.

In the next step the Pt nanoparticles were deposited on carbon supports in accordance to [106][105]. The carbon support was pretreated by adding 80 mg of the carbon support material to 40 ml of EG and ultrasonicating the mixture for 15 minutes. A known volume of metal colloidal solution was added to the carbon-EG suspension and sonicated for another 10 minutes. The pH of the mixture was adjusted to be approximately 2 by adding 1 M HCl. The mixture was stirred at 55 °C for 1080 minutes with N_2 continuously bubbling through the suspension. The solution was cooled down and centrifuged. The catalyst was then washed repeatedly with acetone and finally water and dried at 70 °C for 500 minutes.

The synthesized electrocatalysts were denoted as XmN where X stands for the abbreviation of the synthesis technique, m is the nominal Pt loading in weight percentage and N is the type of carbon support wherever it is included in the designation and is Vulcan XC-72 otherwise.

An overview of the four different preparations with the corresponding steps is illustrated in Figure 3-1.

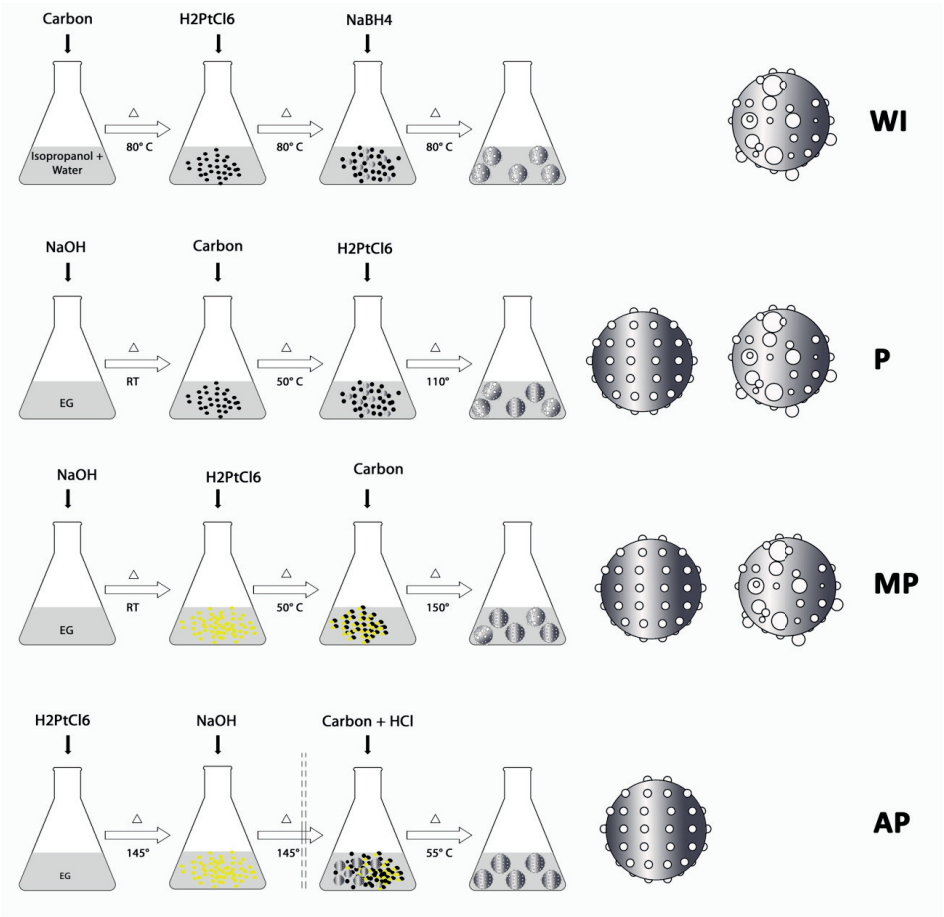

FIGURE 3-1: Schematic representation of the synthesis methods used in this study together with illustration of the molecular architecture of the catalysts as would be seen by TEM.

3.2.2 Physicochemical characterization

Thermal gravimetric analysis (TGAQ500, TA Instrument) with an air flow rate of 100 $mlmin^{-1}$ from room temperature up to 800 °C and a heating ramp of 10 $Cmin^{-1}$ was used to evaluate the purity of the material and examine the actual metal loading.

Transmission electron microscopy (JEOL, JEM-2010) was performed on some of the samples to estimate the particle size and study the metal distribution on the support.

3.2.3 Electrochemical characterization

Since CO is believed to be one of the appropriate choices of adsorbates [69][108] for the determination of the electrochemically active surface area (ESA) of Pt/C PEM fuel cell electrodes, the CO stripping voltammetry was used in this work to both measure the ESA and detect the aggregations.

Electrochemical measurements were carried out in a classical three-electrode cell at room temperature in Ar. The reference electrode was a reversible hydrogen electrode (RHE) placed in a special housing connected to the cell. The counter electrode consisted of a 1.5 cm^2 platinum plate. The working electrode was a glassy carbon (GC) electrode coated with a catalyst-containing ink covered with Nafion® prepared as follows. The catalyst ink was prepared by sonication 1.0 mg of the catalyst in 1.0 mL of water. 20.0 µL of the catalyst ink was pipetted then on the GC disk-type and dried under N_2, followed by addition of 20 µL Nafion®. The area of the GC electrode used in the experiments was 0.196 cm^2. An Auto-lab potentiostat type PGSTAT302N along with the three-electrode cell equipped with necessary connections for Ar and CO was used in this experiment. The voltammetric sequence before sparging the solution with CO included 20 CVs at 100 mVs^{-1} and then 5 CVs at 10 mVs^{-1}. CO sparging then occurred at 50 mV vs. RHE for 120 seconds. Thereafter dissolved CO was removed by Ar purging. The sweep rate was 10 mVs^{-1}. Final step in the experiment was a number of CVs with a sweep rate of 10 mVs^{-1} to ascertain that the electrolyte (0.5 M $HClO_4$) was completely free of CO.

To calculate the electrochemically active surface area (ESA) we considered the process of CO oxidation to CO_2 which involves two electrons as shown here:

$$CO_{ads} + H_2O = CO_2 + 2H^+ + 2e^- \qquad (3\text{-}1)$$

Assuming that CO is linearly bound to the catalyst surface as one CO molecule per Pt atom (Pt-CO_{ads}), the charge required to strip the entire CO layer off the electrode is equal to 420 µC cm^{-2}. The ESA can then be calculated using the total charge transferred during the CO electrooxidation process [109][110]:

$$ESA_{CO}(cm^2g^{-1}) = \frac{Q_{CO}(mC)}{0.420(mCcm^{-2}) \times W_{Pt}(g)} \quad (3\text{-}2)$$

While Q_{CO} is the CO stripping charge and W_{Pt} is the mass of the catalyst [111].

3.3 Result and discussion

Table *3-1* summarizes support type, synthesis technique, nominal and actual metal loading, catalyst uptake (CU), and the ESA. ESA values reported here are only estimations from the CO stripping charge with respect to actual and nominal Pt loadings and may be not very accurate and therefore should be considered only for comparison purposes. The presence of aggregates is also indicated in the table.

TABLE 3-1: Summary of the samples used in this study.

Sample ID	Support	Synthesis technique	Pt Loading (wt%)		Catalyst Uptake (%)	ESA (m^2g^{-1}) [1]		Aggregates[2]
			Nominal	Actual		Nominal	Actual	
AP10	XC72	AP	10	10	100 %	93.66	93.66	no
AP20	XC72	AP	20	19	95 %	101.73	107.08	no
AP30	XC72	AP	30	29	97 %	64.06	66.27	yes
ETEK	Carbon Black	N/A	20	20	N/A	N/A	81.88	no
MP10	XC72	MP	10	9	90 %	94.34	104.82	yes
MP20	XC72	MP	20	12	60 %	34.28	57.14	yes
WI10	XC72	WI	20	10	50 %	25.58	51.16	yes
P10	XC72	P	10	6	60 %	20.37	33.96	yes
P20	XC72	P	20	8	40 %	10.49	26.23	yes
P20CNT	FWCNT	P	26	22	85 %	37.70	44.55	yes
P23CNF	CNF	P	24.6	24	98 %	17.89	18.34	yes

The nominal Pt loading in Table 3-1 is what was expected based on the stoichiometry of the synthesis reaction while the actual compositions of the samples are those that resulted from an examination after synthesis by thermogravimetric analysis. Nominal and actual ESA are also based on the corresponding metal loadings.

[1] Estimated from CO stripping

[2] The presence of aggregates was examined later with TEM imaging and CO stripping voltammetry, so this column was completed at the end of the work.

The ratio of actual to nominal loading is defined in this work as catalyst uptake inspired from the reference [136] for each synthesis technique which is also listed in Table *3-1*. This parameter can be ideally one where the nominal and actual loadings are equal. The presence of aggregates ("yes") or only isolated particles ("no") is presented at the last column in Table 3-1. This conclusion is based on the visual inspection of TEM images and the indication from CO stripping voltammograms.

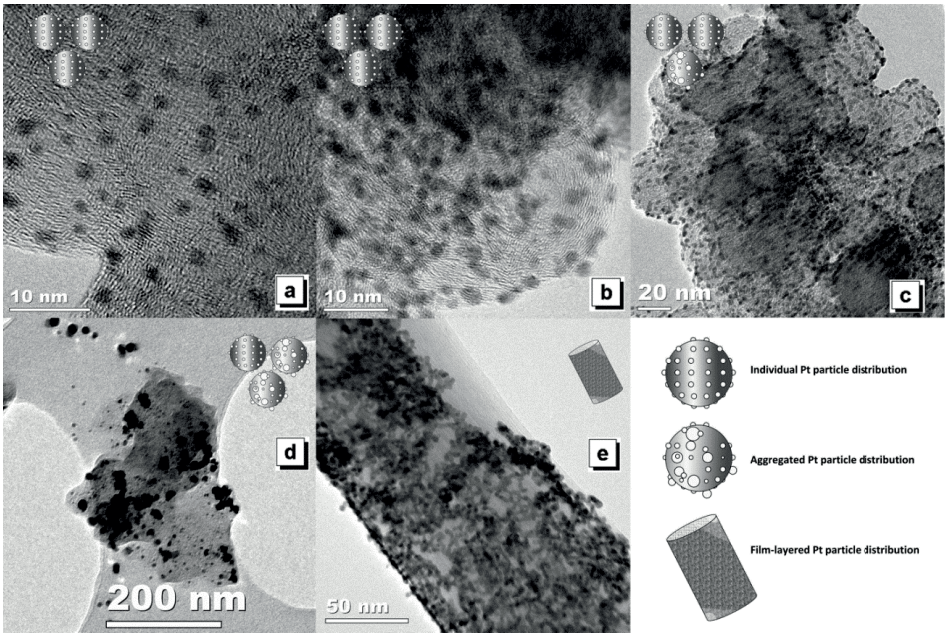

FIGURE 3-2: TEM images for selected samples a) AP10, b) AP20, c) AP30, d) MP10, and e) P23CNF

Figure 3-2 shows TEM images for the selected samples in this study. The symbolic representation of the particle dispersion pattern is also presented in inset of the pictures with a guide at the bottom-right.

Samples AP10 and AP20 appear to contain mostly individual particles and few if any aggregates (Figure 3-2.a and Figure 3-2.b). The catalysts here seem to possess homogeneity and uniform dispersion on the support matrix and the architecture of the catalysts particles is that of isolated-particles only. Pt particle diameter is estimated to be slightly more than 2 nm in these samples.

The highest metal loading in this study was 30% platinum in the catalyst AP30 shown in Figure 3-2.C. The high content of metal in this sample increases the probability of having a mixture of isolated and aggregated particles in the structure of the catalyst, although this may not be very obvious from the TEM images. The higher loading of this sample also resulted in some particle growth and the particle size was estimated less than 4 nm

here. The distribution of the Pt particles is again fairly homogenous on the carbon support.

The TEM image of the sample MP10 shown in Figure 3-2.d presents both isolated and aggregated Pt particles. The Pt particles for this sample synthesized by modified polyol appear to be larger than that of the previous sample (Figure 3-2.a) with the same loading, by synthesized with adsorption polyol.

The TEM image of the sample 23% Pt supported on graphitized carbon nanofiber, P23CNF, is shown in Figure 3-2.e. This is maybe best described as an interconnected set of small Pt particles establishing some sort of a monolayer on the surface of the carbon fiber. This special architecture of the electrocatalyst could possibly affect the electrochemical performance as will be investigated more closely together with CO stripping voltammetric studies.

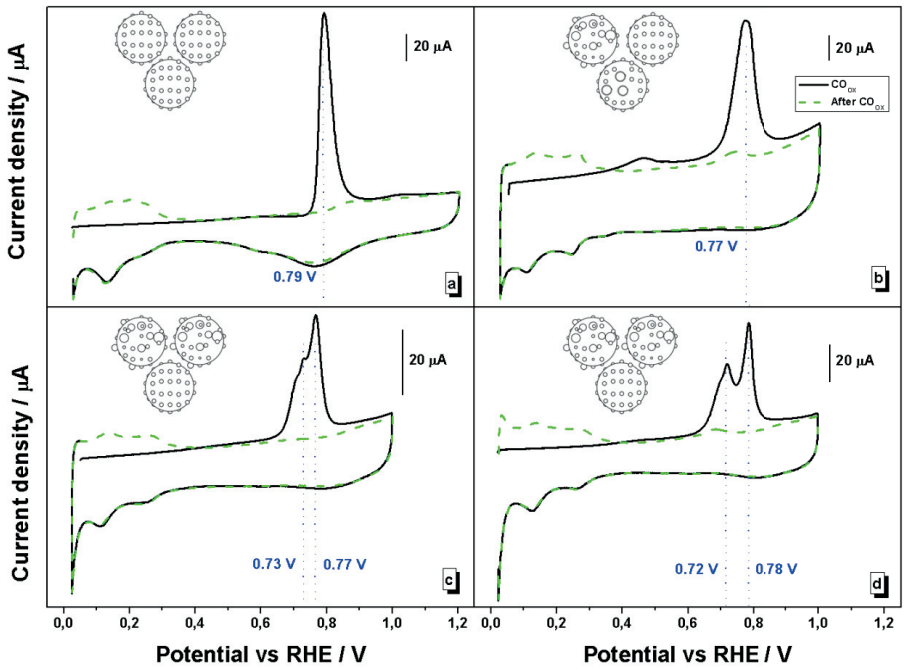

FIGURE 3-3: CO stripping voltammograms for a) AP10, b) MP10, c) P10, d) WI10. Conditions: sweep rate 10 mVs^{-1}, adsorption at 50 mV and 0.5 M $HClO_4$, room temperature.

Figure 3-3 shows CO stripping voltammograms for the same Pt loading (all 10 weight percent) on the same carbon support (all on Vulcan XC72) but synthesized with different methods. Apparently, the synthesis has a decisive influence on the catalytic performance of the resulting catalyst. For AP10, there is a sharp CO oxidation peak at 0.79 V vs RHE indicating an architecture consisting of basically isolated particles as seen in the TEM image (Figure 3-2.a), which is in accordance with previously well-established results [65][69]. There is a slight cathodic shift for the CO electrooxidation peak for MP10 and the peak gets broader due to the contribution of the larger particles in this catalyst (see Figure 3-2.d). For this sample there is also a peak at around 0.5 V vs RHE which might be attributed to oxidation of the quinone compounds in the support [137], however no cathodic peak corresponding to it can be seen.

The sample made by ordinary polyol method, P10, has a peak at 0.77 V vs RHE (for individual particles) like MP10 but in addition to that, there is another peak at lower potential corresponding to the contribution of aggregates (0.73 V, seen as a shoulder on the peak at 0.77 V) due to the presence of particle aggregates [69][138]. This is even more profound for the sample synthesized by impregnation method, WI10, while there is probably a huge contribution from the Pt agglomerates as may be inferred from the ratio

of charge under the agglomeration peak at 0.72 V vs RHE and that corresponding to the small isolated particles at 0.78 V vs RHE.

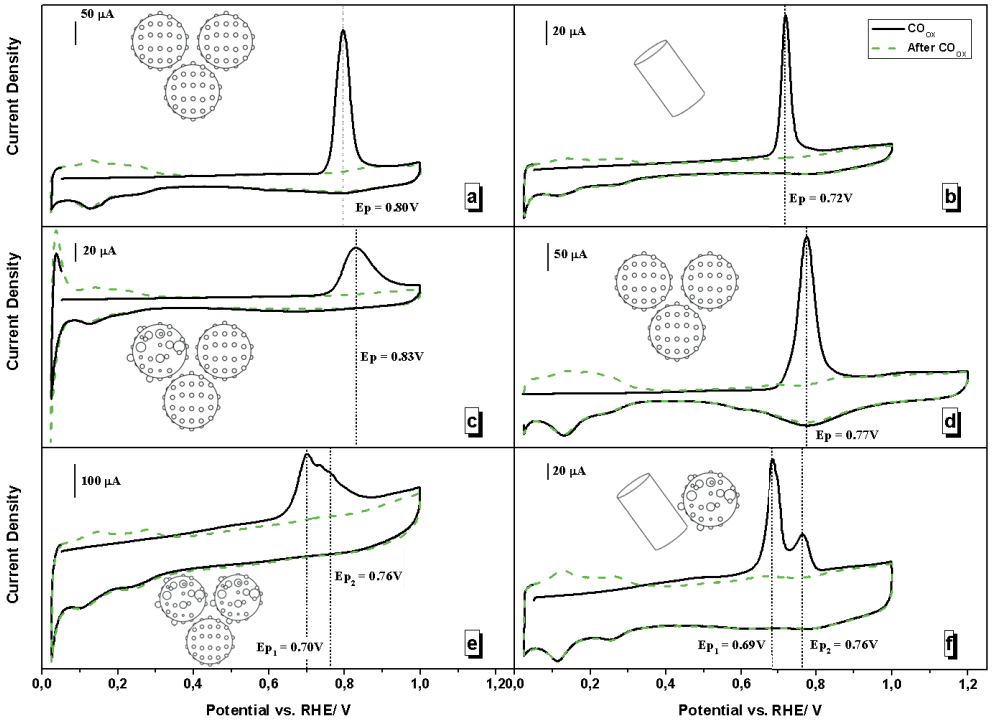

FIGURE 3-4: CO stripping voltammograms for a) 20% Pt/C ETEK commercial catalyst, b) P23CNF, c) MP20, d) AP20, e) P20 and f) P20CNT. Conditions: sweep rate 10 mVs^{-1}, adsorption at 50 mV vs. RHE, 0.5 M $HClO_4$ and room temperature.

Figure 3-4 illustrates the CO stripping voltammetry results for all samples with around 20% platinum loading in this study synthesized by different techniques.

The CO stripping voltammograms of samples ETEK (commercial catalyst), P23CNF and AP20 consist of only a single peak in the CO oxidation region, indicating that the CO electrooxidation reaction was dominated by that occurring on one type of catalyst architecture and not a combination of different size scales. From the peak occurring at 0.8 and 0.77 V vs RHE for ETEK and AP20 respectively, they are therefore thought to contain only isolated Pt particles, a notion that (for AP20) is in agreement with the TEM image in Figure 3-2.b also.

From the shape and the potential of the CO stripping peak in Figure 3-4.c, the MP20 electrocatalyst does not appear to have the same structure as AP20 and ETEK. The much broader oxidation peak for MP20 may imply a wider distribution of particle size. However, single Pt particles still seem to dominate the CO oxidation mechanism.

For the sample P23CNF, a CO stripping peak potential of 0.72 V vs RHE was observed, which is almost the same potential for CO electrooxidation of Pt [106]. The TEM image of this sample (Figure 3-2.e) also shows a particulate film of Pt on the outer surface of the nanofibers and this could possibly explain why it electrochemically looks as if they are only platinum.

P20 displays multiple peaks in its CO electrooxidation region as an indication of a combined architecture of individual and aggregated Pt particles on the carbon support. Higher intensity of the lower potential CO oxidation peak in Figure 3-4.e suggests that Pt agglomerates are dominant in this combined structure. Likewise, peak multiplicity in Figure 3-4.f suggests that P20CNT contain combined architectural features leading to multiple peaks for oxidation of carbon monoxide.

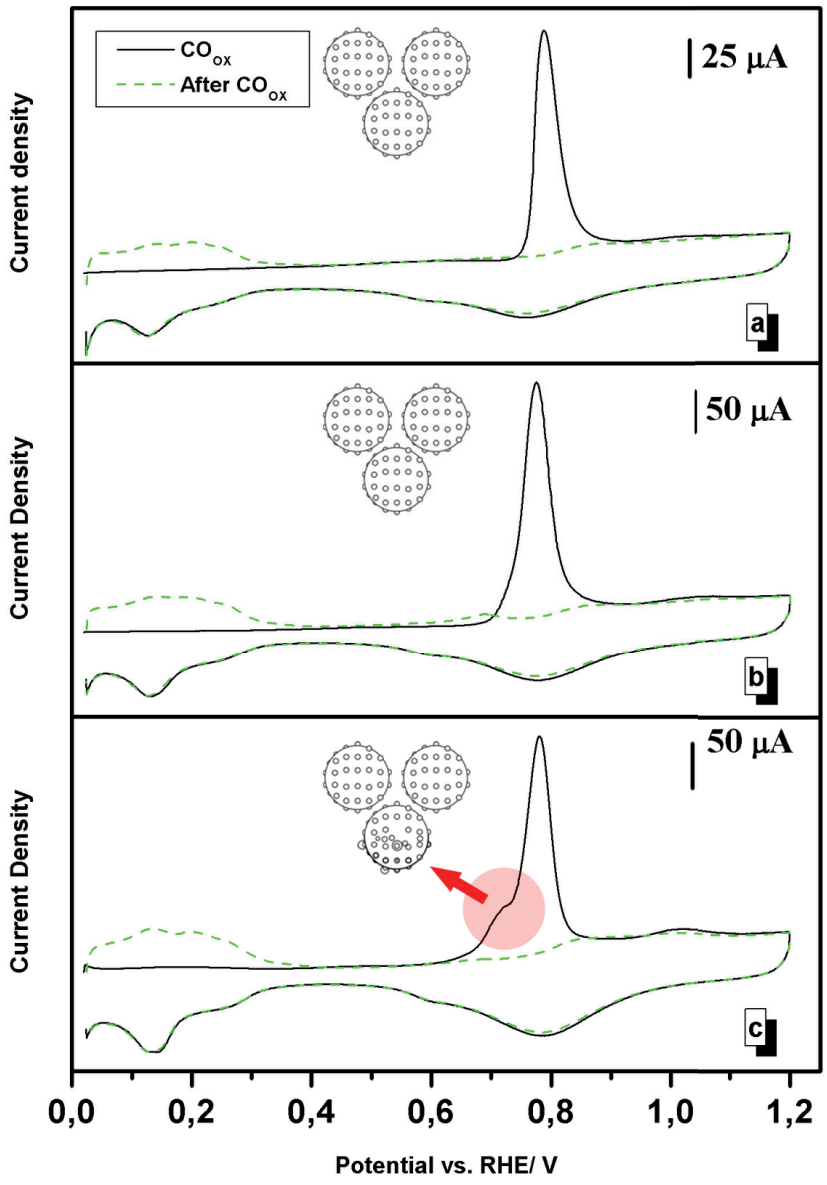

FIGURE 3-5: CO stripping voltammograms for a) AP10 b) AP20 and c) AP30. Conditions: sweep rate 10 mVs^{-1}, adsorption at 50 mV vs. RHE, 0.5 M $HClO_4$ and room temperature.

Figure 3-5 illustrates the CO stripping voltammograms of a set of three samples synthesized by adsorption polyol including the sample AP10 which is again included for the sake of comparison. The support material was Vulcan XC72 for all samples and the platinum loading varied between 10% and 30%.

Even using the most promising synthesis technique in this work for well-dispersed platinum particles on the catalyst, AP, it was observed that a given type of support has a limited capacity to accommodate Pt particles.

The shape and peak potential of the CO stripping peak show that in all samples a major contribution to the stripping peak comes from isolated and independent platinum particles on the support at all the different loadings. However at the highest loading, i.e. 30%, some catalyst particles have agglomerated, and thus a minor shoulder appears on the negative side of the CO oxidation peak. This is also in accordance with the TEM images in Figure 3-2.a, b and c where AP10 and AP20 clearly contained individual well-dispersed Pt particles whereas AP30 seemed to include some larger particles in addition.

This observation for AP30 could potentially fuel the notion that at given synthesis conditions, there is a threshold for a carbon support (Vulcan XC-72 in this case) that if passed, the accommodation of Pt isolated particles is hindered, and the signs of formation of aggregates thus start to appear.

The TEM images and CO stripping results show that the synthetic route by which the catalyst is made significantly influences the structural and thus electrochemical properties of carbon supported platinum nanoparticles.

Figure 3-6 summarizes how the different synthesis techniques in this work affect the catalyst uptake and ESA for electrocatalysts with a range of given carbon support materials and metal loading. The catalyst uptake for the commercial sample, ETEK, was not possible to calculate since the nominal Pt loading was not available from the supplier and therefore the CU line is dashed around the corresponding point for this sample.

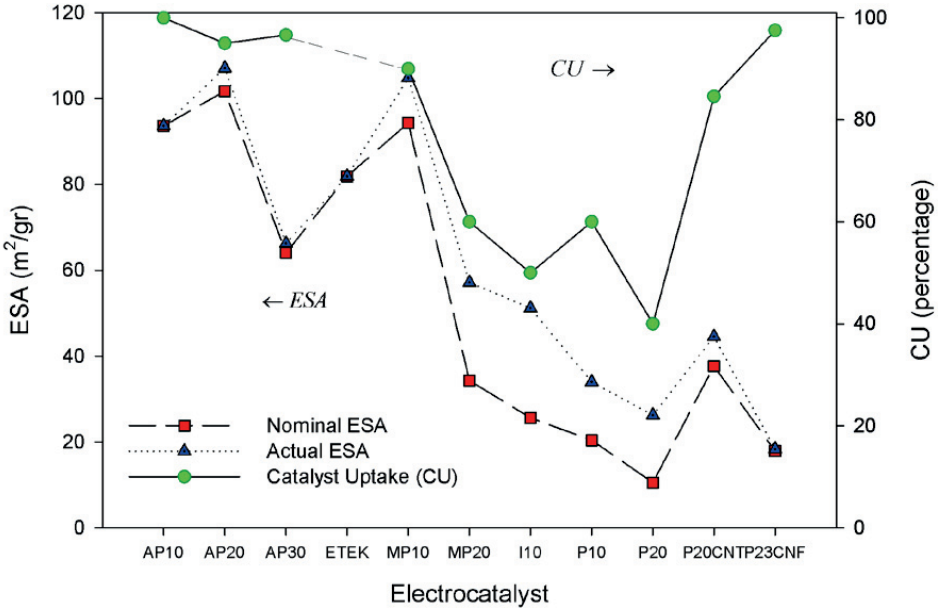

FIGURE 3-6: Electrochemically active surface areas and catalytic uptakes for the electrocatalysts used in this study.

It is seen that for the same type of support materials, the following relationship among the samples appears to hold:

$$\mathrm{CU_{AP}} > \mathrm{CU_{MP}} > \mathrm{CU_{wI}} \approx \mathrm{CU_{P}} \qquad (3\text{-}3)$$

where CU is the catalyst uptake and the indices give the synthesis techniques. Almost the same sequence can be seen for the electrochemical active surface area, and thus:

$$\mathrm{ESA_{AP}} \geq \mathrm{ESA_{MP}} > \mathrm{ESA_{wI}} \approx \mathrm{ESA_{P}} \qquad (3\text{-}4)$$

Catalyst uptakes less than 100% mean that the Pt particles were lost in the course of the preparation steps. We believe that the reason for lost catalyst during synthesis is the formation of lumped (i. e. aggregated) structures that are more vulnerable and can be often washed off. From the outcome of the electrochemical measurements together with corresponding TEM images it appears that the higher catalyst uptake correlates with minor degree of agglomeration and vice versa.

With the exception of nanocarbon supports the trend in ESA for the different synthesis techniques is the same as catalyst uptake. It can be then thought that the more successful the synthesis technique in maintaining the amount of platinum, the higher the ESA. This can be seen from the trends in Figure 3-6 and Eq. (3-3) and Eq. (3-4). For the electrocatalysts supported on nanofibers and nanotubes, the film-like pattern of Pt

particles over the outer surface of the support (Figure 3-2.e) could possibly explain why the ESA is not as high as expected based on the high catalytic uptake.

We employ the catalyst uptake, ESA and structure of the resultant electrocatalysts to rank the synthesis techniques applied in this study. Based on the data analysis as summarized in Figure 3-6 and Eq. (3-3) and Eq. (3-4), we thus consider wet impregnation inferior to polyol, polyol inferior to modified polyol and finally modified polyol inferior to adsorption polyol. It has to be noted that this ranking is based on the present observations and is valid with the experimental conditions explained in this article.

We now seek to rationalize how each of these methods produces different electrocatalysts with distinct catalytic and structural features in terms of the Pt-precursor adsorption density in each technique. For a given carbon support, the density of Pt precursors adsorbed is expected to be significantly dependent on the solution's pH, among other influential factors such as processing temperature, conforming to earlier studies [139][140].

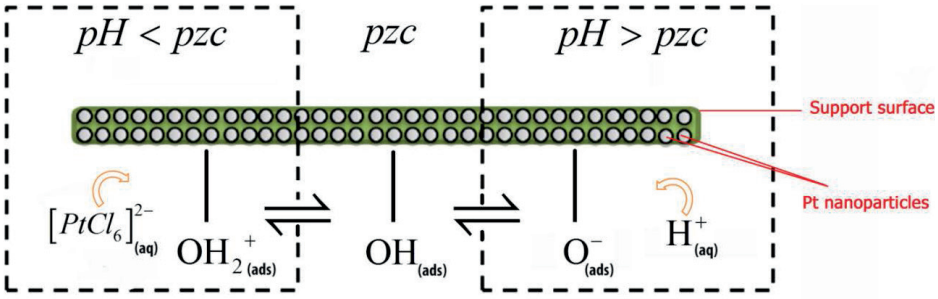

FIGURE 3-7: Drawing for point of zero charge and the favorable electrostatic ion attractions in the platinic acid media.

Figure 3-7 is a schematic representation of the carbon surface as a function of pH for the final stage of the synthesis solution together with influential species in the Pt/C synthesis process.

Since $PtCl_6^{2-}$ ions are negatively charged it appears favorable for Pt nanoparticles to interact with the carbon support in the acidic pH. Thus, the density of adsorbed hexachloroplatinum (IV) is less for pH values higher than the isoelectric point (IEP) or the point of zero charge (pzc) if no other adsorbing ions are present in the solution compared to pH values less than the IEP or the pzc.

In the initial phase of the wet impregnation synthesis the dissolution of chloroplatinic acid (CPA) makes the solution acidic with a pH around 4.

Besides the amount of BH_4^- that is already spent to reduce $PtCl_6^{2-}$, its surplus will be neutralized by the released protons according to the following path [141]:

$$BH4^- + H^+ + 3H_2O \rightarrow H_3BO_3 + 4H_2 \quad (3\text{-}5)$$

This also indicates that the amount of sodium borohydride may have consequences for the dispersion. Eventually the entire mixture ends up in the basic range.

Since adsorption of $PtCl_6^{2-}$ ions on the support is hindered electrostatically by the negative charge at the carbon surface at pH>pzc, growth of Pt on already existing nucleation centers is favored and large particles on the carbon surface apparently results. This argument assumes that significant amounts of precursors adsorb only before the addition of the NaBH4, and also that the carbon itself with a reported pzc of 6.9 [142] does not significantly contribute to the reduction of the precursors.

In the polyol method (see Figure 3-1 for detailed recopies) we again encounter indications of the presence of Pt agglomeration on the samples characterized by CO stripping. In this technique ethylene glycol acts as both reducing agent and solvent. The method offers control over the particle size and dispersed nanoparticles through its dual functionality of reducing agent and stabilizer. The latter is effected by glycolate derived from the EG itself, which acts as a stabilizer for metal colloids [127][104]. As the reaction proceeds the CPA gets reduced and the EG oxidized. In the initial phase of the synthesis the pH is high, but in the later phases of the synthesis the pH of the solution decreases since protons are produced through the EG oxidation as more EG molecules are turned to glycolic acid [104]. At the same time, the stabilizing effect of the EG fades out since the concentration of the glycolate decreases as it becomes protonated in the more acidic solution.

In addition to the effect of a reduced concentration of stabilizing glycolate, the addition of carbon and the choloroplatinic acid to the mixture before heating may cause some of the hexachloroplatinum (IV) ions to adsorb on the carbon much in the same fashion as discussed above in connection with the wet impregnation method. Changing the processing temperature and reversing the sequence in which carbon and the precursor was added, which has previously been claimed to be beneficial for Pt dispersion [143], does not appear to avoid agglomeration, and this is in agreement with both hypotheses.

However, the results that the addition of carbon to mixture after the Pt particles have formed strongly indicate that the adsorption of Pt precursors on the carbon support is the likely source of agglomeration in the polyol and modified polyol methods. Consequently, adding the carbon after the Pt particles have formed results in a narrow sized distribution and the absence of large agglomerates provided that the accommodation capacity for the support is not trespassed. This result appears to be opposite of the conclusion recently reached by Briskeby et al. [144] who synthesized Pt particles on carbon support employing citric acid as stabilizer and reducing agent and for a different type of carbon. A tuning of the synthesis conditions for the best possible

result therefore appears necessary depending on the type of reducing agent and the type of carbon support.

3.4 Conclusion

The synthetic route effectively affects the structural and electrochemical properties of carbon supported platinum nanoparticles. In this work we optimized the architecture of PEMFC electrocatalyst through choice of synthesis method and optimization of synthesis conditions.

Although the wet impregnation method was easily applicable and had no waste streams, in this particular work it exhibited poor capability for anchoring high metal loading, and hence its electrocatalytic activity was low. The architecture of the electrocatalysts synthesized by this technique was a mixture of isolated and aggregated Pt particles with dominant aggregation. As aggregation leads to a lower potential (between 0.69 and 0.75 V vs RHE) for CO oxidation this would actually have some (marginal) advantages from the point of view of CO-tolerance.

The polyol method with some improvements represented a capability to obtain high platinum loading and an acceptable control over the particle size and distribution. Drawbacks of the polyol method in this work included large waste streams and a time-consuming synthesis procedure. The outcomes of ordinary and modified polyol methods were samples with mixture of individual and agglomerated Pt particles comprising dominant individual particles.

Adsorption polyol method where the colloid of platinum nanoparticles is prepared prior to deposition of metallic particles onto carbon support proved to be an appropriate choice to produce electrocatalysts with the desired platinum particle size and distribution. The catalysts synthesized by this method, AP10-30, exhibited the maximum uniformity in particle size distribution and the highest electrochemically active surface areas of the methods investigated here.

The structure of the electrocatalysts presents special electrochemical characteristics of electrocatalysts. By using a proper synthesis technique, it is possible to synthesize electrocatalysts with specific particle size and distribution features. It enables us to synthesize samples containing aggregated or isolated Pt particles on carbon support with flexibility to choose the dominant phase and hence to exhibit targeted electrochemical characteristics.

3.5 Acknowledgments

Virginia Ruiz from Aalto University is greatly appreciated for providing the nanostructured materials (both Pt/C catalyst and carbon support). Yingda Yu is thanked for the assistance with TEM imaging. The financial support of the work by the Research Council of Norway and the Department of Materials Science and Engineering, NTNU, is acknowledged.

Chapter 4

Effect of Catalytic Layer Thickness

In this chapter the influence of catalyst layer thickness on the performance of a degraded cathode is reported. The cathode was fabricated of samples containing only isolated Pt particles supported on carbon black. The chapter is a manuscript intended for publication.

4.1 Introduction

To overcome the cost issue as a major barrier limiting the large-scale commercialization of proton exchange membrane fuel cells (PEMFCs) is a central focus of PEMFC research [145][146][147][148][149][150]. An important part of the PEMFC for which substantial cost-reductions would be possible is the catalytic layers, which typically consist of carbon material, ionomer and platinum. Given the limited availability and high cost of precious metals such as Pt, optimization of catalyst layer structure is of particular importance to get PEMFCs closer to market. Evidence exist to show that the catalyst layer imperfections such as a spot with restricted metal loading have a substantial effect on both membrane electrode assembly's (MEA) performance and durability [151][152][153]. This shows the importance of studies on catalyst layer in the larger context of PEMFC commercialization.

It has been suggested that for PEMFCs the catalyst layer should be as thin as possible for a given catalyst loading in order to increase catalyst utilization and as a consequence decrease the cost of the electricity produced by the fuel cell [154][155][156]. Processes at the PEMFC cathode are complex and involve complicated transport and electrochemical reaction phenomena that take place in the porous cathode catalytic layer (CCL). Therefore, the idea that the CCL should be as thin as possible has been debated [157], making the optimization of the CCL a field of research with potential rewards in terms of improved performance and extended life-time.

Some relevant modeling and simulation work [158][159][160][161] has appeared in the last decades which successfully optimize the CCL in terms of factors affecting in the catalyst layer of PEMFCs such as porosity, loading, and CCL thickness. For example Suzuki et al. made efforts to understand the link the between the CCL's particulars such as pore networks in the CCL on one hand and the polarization characteristics on the other. Based on a three-dimensional pore network model of PEMFC they predicted that an MEA with 40% porosity has better electrochemical performance and higher power density than an MEA with 50% porosity and the same catalyst loading.

Song et al. [162] also by using a numerical optimization technique predicted that for a 0.3 $mgcm^{-2}$ Pt loaded catalyst layer, the optimal thickness lies between 10 µm and 15 µm and concluded that in the design of catalyst layers, thickness needs special consideration. Here is the need for more experimental work dealing with the link between the catalyst layer thickness and the electrochemical performance of the MEA applied in a PEMFC.

Obut and Alper [163] used a numerical assessment method to predict the fuel cell MEA performance dependence on cathode catalyst layer parameters. They showed that a fuel cell working with an 80 µm thick catalyst had better performance than cells with layer 40 µm and 20 µm thick catalyst layers at currents below the limiting current. In consequence they suggested that in low and medium current densities the thicker the catalyst layer, the higher the fuel cell performance while at very high current densities use of thicker catalyst layer is ineffective.

While there is research related to the effect of the thickness of the Nafion® electrolyte on fuel cell performance [164], there appears to be little experimental work on the effect of CCL thickness. It was, however, indicated in recent research [165] that CCL experiences a significant thinning upon degradation protocols and the thinner areas of the catalyst layer have a lower electronic resistance, but less active catalyst. Also, in the theoretical models on the effect of catalyst layer thickness on the cell performance referred to above, the total platinum loading of catalyst in the layers was not kept constant for the different layer thicknesses. As a result the reported effect of catalysts layer thickness on the fuel cell performance may in fact have been the effect of total platinum loading of the catalysts layer of the cell. A thicker CCL would therefore imply a larger total platinum

loading in the layer. In these studies the effect of excessive platinum loading in the thicker catalyst layer was not neutralized.

An issue as important as the performance per se is also the durability of the CCL. In a typical Pt/C electrocatalyst carbon blacks (e.g. Vulcan XC-72) are used as catalyst support due to its low cost and high availability. Thermodynamically the carbon support is expected to oxidize to CO_2 and CO at potentials higher than 0.2 V vs. RHE [166]. On the other hand, under fuel cell operating conditions and cathode potentials around 0.6-0.9 V vs. RHE, the kinetics of carbon corrosion is still quite slow. In practice, elevated potentials greater than 1.2 V vs. NHE are required to corrode the carbon support at sufficiently high reaction rates to cause a significant degradation to the PEMFC electrode [167].

It appears that few studies exist that investigate the stability of a PEM cathode CCL thickness. It is well-known that the potential is not evenly distributed in porous electrodes [168], and therefore there may be a thickness dependence also for the stability since this is related to the local potential in the electrode. Also, degradation depends on the chemical environment and thus on transport rates etc., which may differ in a thick electrode from that of a thin. For the reaction $O_2 + 4H^+ + 4e^- \rightarrow 2H_2O$ to occur this requires the simultaneous presence of both electrons and hydrogen ions. Since proton mobility is relatively low in the catalyst layer while electron mobility will in general be expected to be much faster, the electrochemical reaction will occur to a larger extent close to the membrane than far from it. Thus, a decrease in the catalyst layer thickness (for example as a consequence of corrosion) would not necessarily affect the electrochemical performance in a proportional manner. So the current distribution in thick and thin catalyst layer is one of the important factors and one for which deeper studies are needed. Also efforts to understand the role that catalyst layer variations play in electrochemical performance in liquid electrolyte cell [169] and relations to performance in fuel cells need in general to be completed by more in-situ studies.

The scope of this work is thus to investigate role of the catalyst layer thickness with respect to degradation and corrosion and MEA electrochemical performance, but with a constant total loading of the catalyst. The cathode was chosen for the study since the rate-determining chemical reaction and the lion's share of the activation overpotential losses take place in this region. The degradation in cathode therefore merits attention for durability studies of PEMFCs. In this study a well-controlled synthesis technique was used to control the Pt-particle dispersion in the CCL and also to produce samples with almost the same range of particle sizes to avoid the effect of particle size on activity and durability of the electro-catalysts [170][171]. The results below will demonstrate that the electrocatalytic activity is independent of thickness for a given Pt loading and for typical thicknesses employed in PEM fuel cells. For degradation processes, on the other hand, we aim to show that thickness does matter in layers with a constant total Pt content, and that the major cause for the degradation is not related to Pt-catalyzed carbon corrosion.

4.2 Experimental

4.2.1 Catalyst synthesis

Materials and solvents were obtained from commercial suppliers and were used without further purification. Carbon black (Vulcan XC72, CABOT Corporation), hexachloroplatinate (IV) (Johnson Mattey, Pt content: 39.76 %, purity ≥ 99%), sodium hydroxide (VMR, purity ≥ 99%), ethylene glycol (Sigma-Aldrich purity ≥ 99%) and analytical grade acetone have been used to synthesize the catalyst by the adsorption polyol (AP) method explained in details elsewhere [101][105] but in brief, first Pt colloidal solution was prepared using a polyol method. In this method 1.0 g of H_2PtCl_6 is dissolved in 250 ml of ethylene glycol followed by addition of 100ml of 0.5 M NaOH in ethylene glycol to maintain the pH slightly basic. Later, the prepared mixture is heated at 145 °C for 4 hours. Nitrogen was kept flowing on the solution in the course of reaction. After this step for the deposition of Pt nanoparticles on carbon material, the support was suspended in ethanol by ultra-sonication for 15 minutes. Later a known volume of metal colloidal solution was added to the suspension described above and the pH of the mixture was adjusted to around 2 by addition of 1 M HCl and sonication for another 10 minutes. The above mixture was stirred at 55 °C for 18 hours by bubbling N_2 through the suspension. The solution was cooled down and centrifuged. The catalyst was then washed repeatedly with acetone and finally water and dried at 70 °C for 500 minutes. The same batch of Pt colloidal solution was used to deposit on the carbon support with different metal loading namely 10% (PtC10), 20% (PtC20) and 30% (PtC30).

4.2.2 TEM analysis

Transmission electron microscopy (JEOL JEM-2010) was performed on the samples to estimate the particle size and study the metal distribution on the support as well as the morphology. TEM was also used to check for presence of aggregates or isolated platinum nanoparticles in the catalysts.

From the estimates of the particle size from the high resolution TEM images and by assuming that the particles are spherical, we estimated the Pt particle size from the Eq. (4-1):

$$S_{overall} = \frac{6 \times 10^3}{\rho \times d} \qquad (4\text{-}1)$$

where $S_{overall}$ is the overall surface area, ρ =21.4 gcm^{-3} is the density of Pt and d is the particle size [109].

4.2.3 Thermal gravimetric analysis

Thermal Gravimetric Analysis (TGA) was conducted on a NETZCH, STA449C thermogravimetric analyzer using a flow of air between temperature range 25 and 800 °C to determine the actual Pt loadings on the carbon foam supports.

4.2.4 MEA fabrication

Nafion® 112 membranes (DuPont) were pre-treated by boiling in 3% H_2O_2 as well as in 0.5 M H_2SO_4 followed by rinsing in boiling Milli-Q water. The ink was prepared by mixing either 10 wt%, 20 wt% or 30 wt% Pt/Vulcan with 5 wt% Nafion® solution (DuPont). Equal amounts Milli-Q water and iso-propanol was subsequently added so that the final ink had a constant Pt/C concentration of about 3 wt%. The ink was ultrasonicated for 1 hour and vigorously stirred overnight. The working electrodes (WE) were prepared by spray-painting the pretreated Nafion® 112 membranes placed on a 90 °C hot plate. Electrode loading was determined by comparing the weight difference between the original and the Pt-catalyst coated membranes. The achieved Pt loadings were 0.1 $mg_{Pt}cm^{-2}$, 0.12 $mg_{Pt}cm^{-2}$ and 0.11 $mg_{Pt}cm^{-2}$ for the 10 wt%, 20 wt% and 30 wt%, respectively and the Nafion® to carbon ratio (N/C) was 0.8. Catalyzed ELAT (ETEK, Inc.) electrodes, used as combined counter and reference electrode (CE/RE), were employed in the anode with 30 wt% Pt/Vulcan XC-72 and loading of 0.5 $mgPtcm^{-2}$. The fabrication of MEAs was accomplished by heat-pressing the ELAT electrodes onto the catalyzed Nafion® 112 membranes at 130 °C under a pressure of 3 bar for 5 min. Gas diffusion layer (GDL Sigracet 10BA) was mounted on the WE.

4.2.5 SEM analysis

SEM imaging was carried out using a Hitachi S-4800 FE Scanning Electron Microscope operated at 1.5 kV accelerating voltage at 8.3 mm and 8.8 mm working distances. The analysis cross sections of the MEAs were obtained by the freeze and break technique described elsewhere [172]. Pore size distribution of the catalysts were estimated from SEM images using the open-source image software ImageJ [173].

4.2.6 In-situ electrochemical evaluation

The fuel cell hardware was purchased from Fuel Cell Technology Inc. The sealing pressure applied to the MEAs was 6 MPa. Additionally, the test bench also controlled the temperature of the cell (T_{cell}), the H_2 and O_2/air humidification temperatures ($T_{hum,a}$ and $T_{hum,c}$) as well as the temperature of the pipe (T_{pipes}) connecting the humidifiers (Fuel Cell Technology Inc.) with the cell. Cyclic voltammetry and polarization curves were recorded by using a PAR 273A potentiostat. Electrochemical impedance spectroscopy (EIS) measurements were carried out on an Autolab 302N impedance analyzer.

Cyclic voltammograms and CO stripping were obtained at 80 °C using fully humidified gases, sweep rates of 20 mVs^{-1} with a flow rate of 60 $mlmin^{-1}$ of N_2 fed to the WE and 120

mlmin^{-1} of 5% H_2/Ar fed to the CE/RE. Due to lower H_2 partial pressure on CE/RE, the presented cyclic voltammograms were corrected with a 45.5 mV shift calculated by the Nernst equation [17].

The electrochemically active surface area (ESA) is estimated based on the charge transferred during the CO electrooxidation assuming CO monolayer bonded with one Pt atom in a linear adsorption configuration (Pt-CO_{ads}) and Eq.(4-2) [110]:

$$ESA_{CO}(cm^2 g^{-1}) = \frac{Q_{CO}(mC)}{0.420(mC cm^{-2}) \times W_{Pt}(g)} \quad (4\text{-}2)$$

where Q_{CO} is the charge transferred related to CO oxidation reaction, 420 µC cm^{-2} is the charge required to oxidize CO monolayer bonded with one Pt atom in a linear adsorption configuration and W_{Pt} is the mass of Pt used in the electrode.

To estimate the conductivity of the CCL ionomer, EIS measurements were carried out with N_2 and 5% H_2/Ar on the WE and the CE/RE with flow rates of 60 mlmin^{-1} and 120 mlmin^{-1}, respectively. EIS spectra were recorded with an amplitude of the AC signal of 10 mV (top) at 0.35 V vs RHE by varying the frequency between 10 kHz and 0.1 Hz. EIS spectra were analyzed according to Eq. (21) presented in the work of Jaouen and Lindbergh [119].

The polarization curves were recorded at a sweep rate of 1 mVs^{-1} between open circuit potential (OCP) and 0.3 V vs. CE/RE. To investigate the mass transport properties of the cathodes, diluted O_2 was used as oxidant using the same flow rate (120 mlmin^{-1}) ensuring equivalent water content at a particular current density in the cell.

The recorded polarization curves were corrected for iR-drop using the high frequency resistance (HFR) of the fuel cell that was obtained for every 100 mAcm^{-2} increment in current density between a 100 kHz and 1 kHz range and applying an AC signal amplitude that was 5% of dc (direct current) measured. Moreover, longer EIS spectra between 100 kHz-100 mHz frequencies were also recorded at 0.01, 0.2, 0.5 and 1 Acm^{-2}.

4.2.7 Accelerated degradation test (ADT)

The carbon degradation routine consisted of 100 cycles of the cathode potential between 0.6-1.5 V vs. RHE using a sweep rate of 40 mVs^{-1}. The temperature of the cell was set 80 °C, using fully humidified H_2 at the anode and fully humidified O_2 at the cathode.

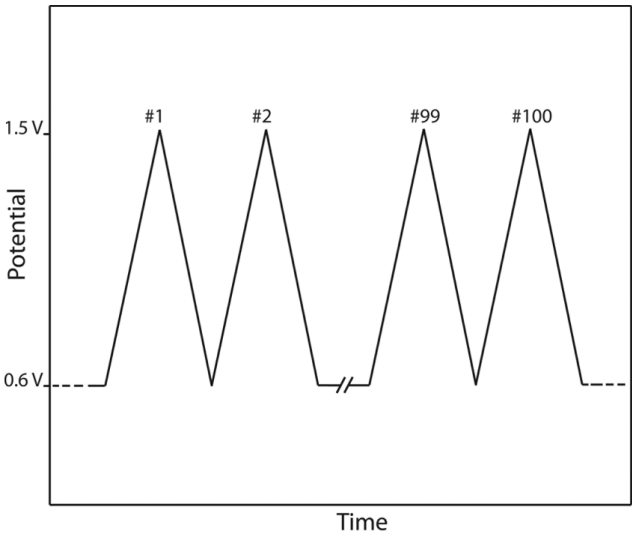

FIGURE 4-1: Illustration of the potential cycling in the degradation protocol applied to the MEAs in this study

4.3 Results and discussion

4.3.1 Ex-situ evaluation of synthesized catalyst

Figure 4-2 shows the substance weight percentage as a function of temperature for PtC10, PtC20 and PtC30 electrocatalysts as measured by thermal gravimetry. The steep drop around 400 °C for all samples is a signature of carbon oxidation, and the residue is the platinum content in the specimens. It is seen in Figure 4-2 that the nominal loading is in agreement with the weight percentage of the residue up to 800 °C.

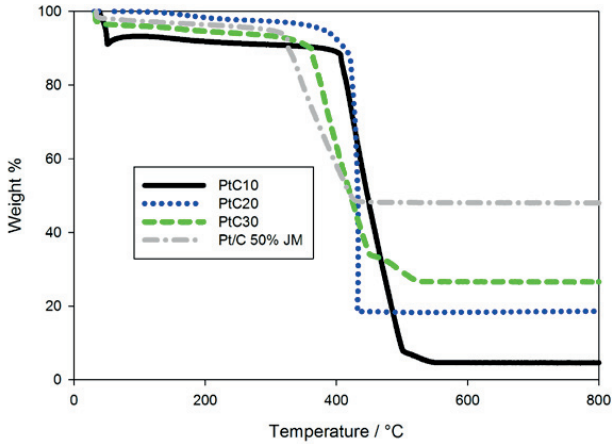

FIGURE 4-2: Thermal gravimetric analysis (TGA) results for the samples listed in Table 4-1. The atmosphere was oxygen and the temperature ramp was 10 °Cmin^{-1}.

The TPO results for the three catalysts in this study and a commercial benchmark (Pt/C 50% JM) are presented in Figure 4-2. From Figure 4-2 and Figure 4-3 it is apparent that the higher the platinum content (relative to the amount of carbon) the less stable the catalyst, which may be attributed to the catalytic action of Pt in the oxidation of carbon degradation.

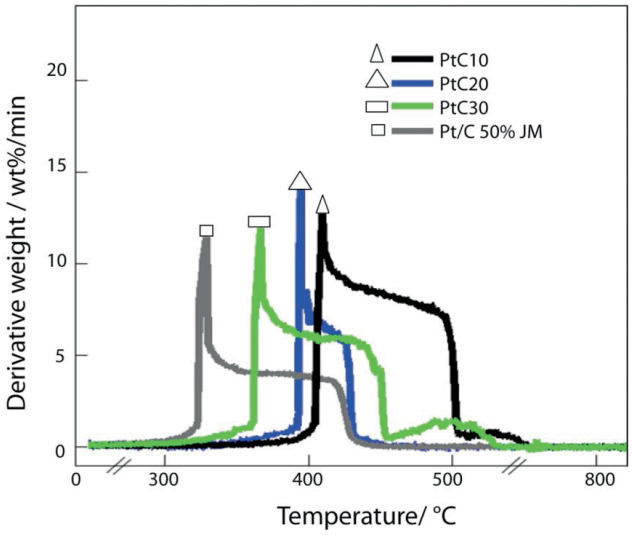

FIGURE 4-3: Temperate programmed oxidation (TPO) results for the samples listed in Table 4-1. Conditions: the same as Figure 4-2.

The different peak temperatures in Figure 4-3 for the catalysts indicate different activation energies for the same reaction (carbon reacting to CO_2), meaning that the Pt to a significant degree catalyzes the carbon corrosion reaction. It has been shown that the particle size influences TPO peak temperatures, a large particle size leading to high peak temperature and vice versa for a given Pt loading [174]. The variations in particle size here are of a similar or even larger magnitude as in [174], where the PtC10 sample is the smallest particle diameter and PtC30 is the largest. Our results are therefore opposite of those of [174]. However, in our case the loading is not constant, and the results in Figure 4-3 therefore suggest that the differences in peak temperature are due to the catalyst loading and not to the differences in particle size. We cannot rule out, however, the differences in structure and size also seem to affect the peak temperatures.

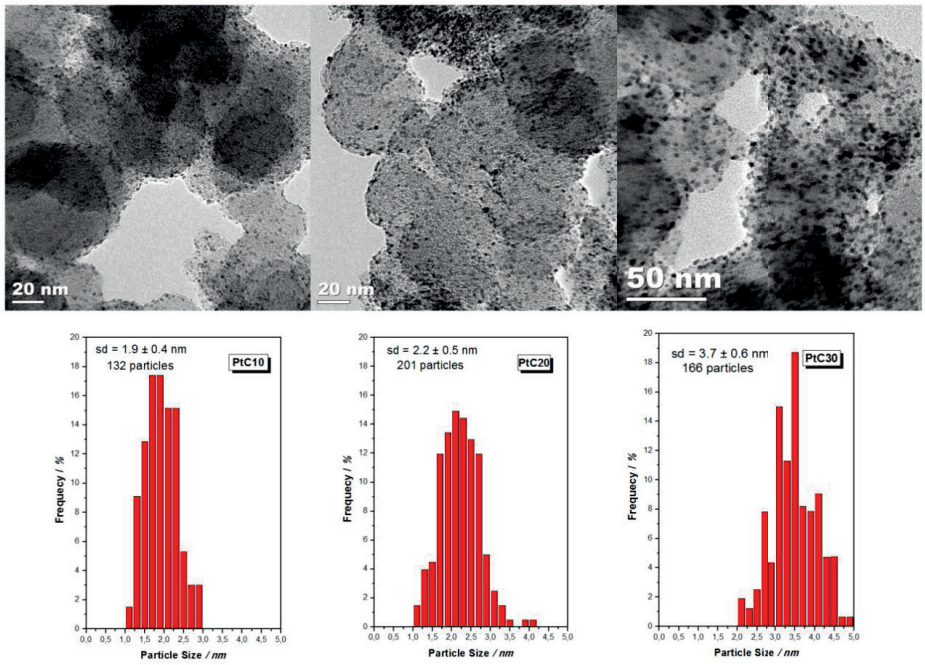

FIGURE 4-4: TEM images and corresponding histograms of particle size distribution for the samples a) PtC10, b) PtC20, c) PtC30.

TEM images of the electrocatalysts and the corresponding histograms of particle size distribution are shown in Figure 4-4. All catalysts appear well dispersed with a particle size around a few nanometers. However, whereas the Pt particles look very well separated in PtC10 and PtC20, some minor tendencies towards clustering are apparent in PtC30. The histograms indicate fairly narrow particle distributions. The average particle sizes for the three samples are also summarized in Table 4-1 and, again, they all seem to be in the

same range, that is 1.9 nm, 2.2 nm and 3.7 nm for fresh samples of PtC10, PtC20 and PtC30 respectively. The results demonstrate that although the materials and preparation conditions remained the same, more Pt content favors slightly higher particle size.

From the TEM images of the fresh samples the Pt-Pt distance was also measured to be 3.6, 3.1 and 4.2 nm for PtC10, PtC20 and PtC30 respectively. This is of relevance since according to the territory theory by Watanabe et. al [175], the distance between catalyst particles may affect catalytic activity if the catalyst support is active in adsorbing and transporting reactants or products of the electrochemical reaction.

TABLE 4-1: Properties of the catalysts used in this study including metal loading, platinum particle sizes and average Pt-Pt particle distance. All samples are supported on carbon XC-72.

Sample	**Pt on C load**	**Pt size (nm) (TEM)**	**Pt-Pt distance (nm) (TEM)**	**$S_{overall}$ (m^2g^{-1})**
PtC10	10 wt%	1.9±0.4	3.56±0.4	147.5± 32
PtC20	20 wt%	2.2±0.5	3.11±0.5	127.4±29
PtC30	30 wt%	3.7±0.6	4.2±0.6	103.8±24

Table 4-1 summarizes the Pt loadings and the estimation for particle size and overall surface area from the TEM images calculated using Eq. (4-1).

It will be shown below that the sample PtC20 has the highest electrochemically active surface area, slightly more than that of PtC10, while sample PtC30 has the lowest ESA. It thus appears that in the case of PtC30 that the significantly larger particle size led to lower ESA while the lesser difference between the particle sizes for PtC10 and PtC20 led to the lesser differences in the ESA between these samples.

4.3.2 Fuel cell performance and degradation using pure H_2 and O_2

Figure 4-5 shows the iR-corrected polarization curves for the three MEAs before and after the ADT. The polarization curves are not corrected for the crossover current. PtC20 had a slightly lower cell resistance, as measured from EIS at 1 kHz, than the other two samples, e.g. at 1 Acm^{-2} the values were 121, 111, 124 $m\Omega cm^2$ for the PtC10, PtC20 and PtC30, respectively.

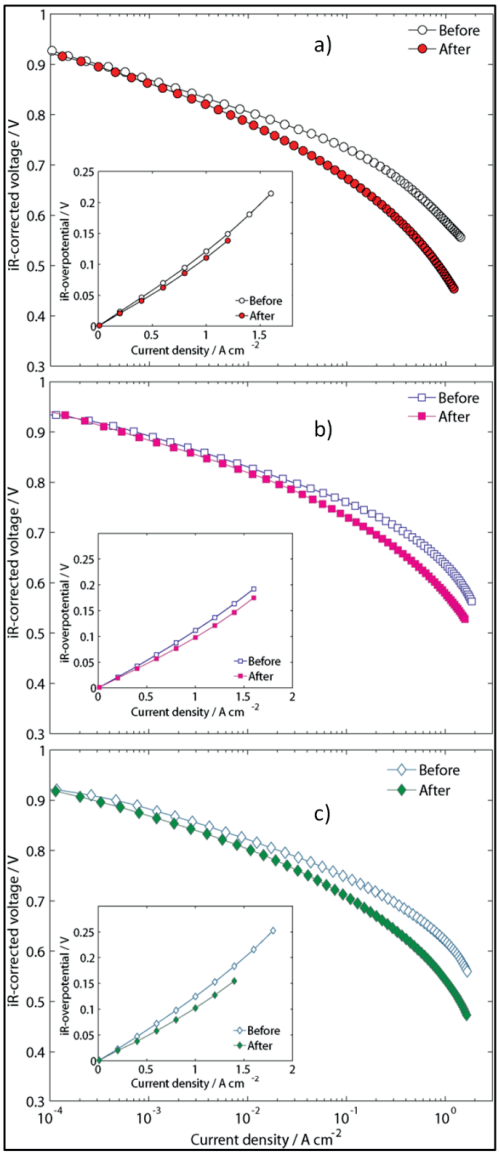

FIGURE 4-5: iR-corrected polarization curves before and after ADT. a) PtC10, b) PtC20 and c) PtC30. Insects: iR related performance loss for the same samples before and after the ADT. Conditions: temperature 80 °C, fully humidified gases with a flow rate of 60 mlmin^{-1} of O_2 fed to the WE and 120 mlmin^{-1} of H_2 fed to the CE/RE. The iR-correction is carried out using the *Re(Z)* in EIS data at 1 kHz.

TABLE 4-2: IR-free voltages at different current densities for the three samples from polarization curves in pure O_2

Current density	iR-free voltage (V)		
	Before	After	% Decrease
At 10 mAcm^{-2}	**PtC10**		
	0.81	0.78	3
	PtC20		
	0.83	0.82	1
	PtC30		
	0.82	0.80	2
At 0.2 Acm^{-2}	**PtC10**		
	0.70	0.63	10
	PtC20		
	0.73	0.70	5
	PtC30		
	0.72	0.67	7
At 0.5 Acm^{-2}	**PtC10**		
	0.64	0.56	14
	PtC20		
	0.69	0.64	7
	PtC30		
	0.67	0.61	9
At 1 Acm^{-2}	**PtC10**		
	0.59	0.48	18
	PtC20		
	0.64	0.58	9
	PtC30		
	0.62	0.54	13

From Figure 4-5 and Table 4-2 it appears that all three MEAs have similar initial performance (within ± 30 mV at 0.2 Acm^{-2}). The initial activity then seems to be independent of the catalyst layer thickness in the working range of thickness in this study. The Tafel slopes for the pristine samples are 65.0, 63.2 and 63.4 mV decade^{-1} for PtC10, PtC20 and PtC30, respectively, and indicates that the mechanism is the same and that the electrodes are unaffected by porosity [176].

As can be seen from Figure 4-5, the activity of all three CCLs experiences a significant decrease upon the ADT. The effects of performance degradation upon the ADT are more significant at high current densities; at low current densities the loss of activity is only a few percent, whereas at high current densities the degradation in performance is quite

pronounced for all samples. However, it seems that the degradation of sample PtC10 was somewhat more provoked by the ADT than the other two.

Figure 4-6 shows the EIS measurements at different current densities before and after the ADT. For the sake of clarity the spectra are plotted as impedance normalized with respect to area as described in the reference [119]. For low current densities the impedance plane plots consist of a single arc, but develop into two separate arcs at high currents along with some inductive features at low frequencies [66].

The impedance data were not fitted to any model; however, by comparing catalyst layers having similar Pt loading and Pt particle size, the same type of carbon support, GDL, experimental conditions, and fuel cell hardware, we make use of a qualitative analysis of the impedance data here instead.

Comparing the spectra of the three MEAs before and after the ADT, it is clearly observed that the size of all the impedance arcs increase upon the ADT. Table 3 shows that the size of the semi-circles at 1 Acm^{-2} increases by 73%, 32% and 28% for the PtC10, PtC20 and PtC30, respectively.

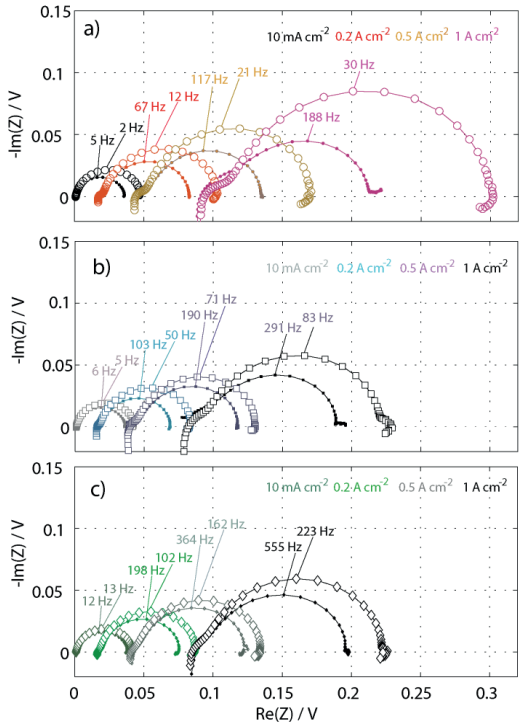

FIGURE 4-6: Nyquist plot of Tafel impedance before and after ADT. a) PtC10, (•) before, (○) after, b) PtC20 (▪) before,(□) after and c) PtC30, (♦) before,(◊) after. Conditions: The same as in Figure 4-5. EIS conditions: Amplitude 5% of i_{dc}, frequency range 10 kHz and 0.1 Hz.

TABLE 4-3: Real impedance from EIS measurements in pure O_2 before and after ADT in oxygen

	PtC10			PtC20			PtC30		
R(Z) (mΩ cm²)	**Before**	**After**	**% Increase**	**Before**	**After**	**% Increase**	**Before**	**After**	**% Increase**
At 10 mAcm^{-2}	35	46	31	35	41	17	37	40	10
At 0.2 Acm^{-2}	65	85	29	53	67	27	58	70	22
At 0.5 Acm^{-2}	91	125	37	77	91	18	79	93	18
At 1 Acm^{-2}	121	209	73	106	140	32	107	137	28

The trend of the decay in fuel cell performance as assessed by impedance spectroscopy is presented in Table 4-3 where PtC20 and PtC30 are almost in the same range of stability while PtC10, the thickest electrode, has a significantly higher performance loss as assessed from the impedance diagrams, the differences between the different catalysts

thus being much more pronounced in the impedance data than in the polarization curves in Figure 4-5. As discussed previously, the changes in performance in pure O_2 can be explained as a loss of ESA.

4.3.3 Fuel cell performance and degradation as a function of O_2 partial pressure

Measurements with diluted O_2 were carried out keeping the total volumetric flow rate constant. During the measurements the amount of water in the incoming gases was held constant. In addition, the high relative humidity and low current density also ensured a low degree of membrane and anode dehydration.

Figure 4-7 shows the iR-corrected voltages at 0.2 Acm^{-2} both before and after the ADT as a function of the partial pressure of oxygen. The voltage is lower the lower the percentage of oxygen and the voltages of the degraded electrodes are consistently lower than those of the corresponding fresh sample. The degraded PtC10 appears to be more sensitive to the P_{O2}-pressure than its pristine counterpart, whereas the curve for the degraded PtC30 appears as a more or less parallel shift of the curve for the fresh PtC30.

As seen in Figure 4-7 and also summarized in Table 4-4, the percentage decrease in cell voltage at 13% O_2 increases with increasing CCL thickness. The iR-corrected voltage decreases as much as 26% for the PtC10, 12% for the PtC20 and 10% for the PtC30. For all the samples the voltage loss for the MEAs subjected to ADT are more than that predicted by the Nernst equation, which we ascribe to a dependence of the kinetics or mass transport on the partial pressure of oxygen.

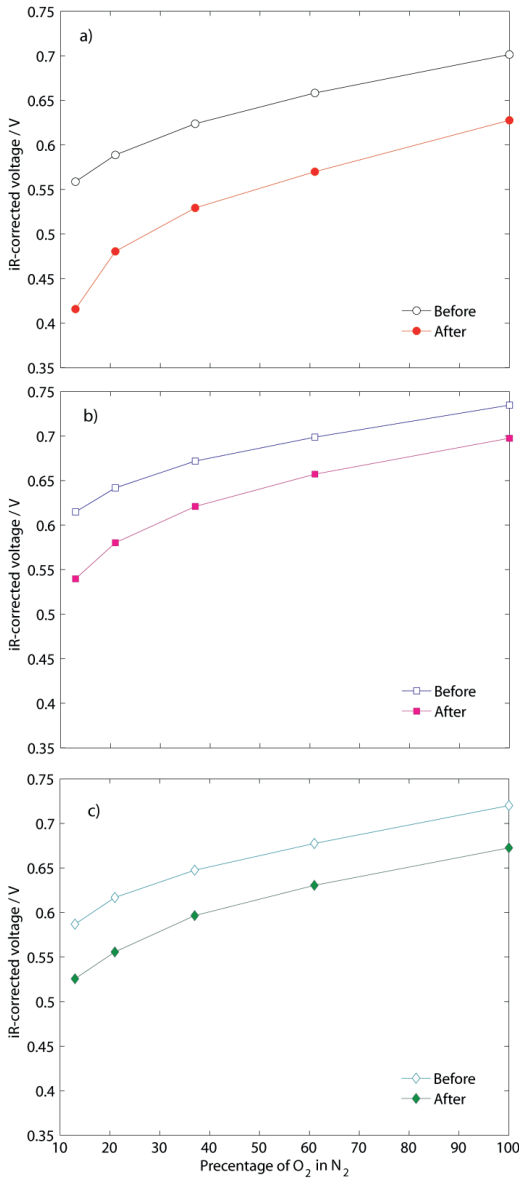

FIGURE 4-7: iR-corrected cell voltage using diluted O_2 at 0.2 Acm^{-2} before and after ADT. a) PtC10, b) PtC20 and c) PtC30. Conditions: atmospheric pressure, temperature 80 °C, fully humidified gases with a flow rate of 60 $mlmin^{-1}$ of diluted O_2 fed to the WE and 120 $mlmin^{-1}$ of H_2 fed to the CE/RE.

These findings are also corroborated by impedance measurements for the same samples in the gas mixtures. Figure 4-8 shows the impedance spectra at 100% O_2 and 13% O_2, both before and after the ADT. All the spectra display a single depressed semicircle-like loop, for some of the samples extending into positive imaginary parts at low frequencies indicative of adsorption as an intermediate step in the reaction kinetics [177][177]. For all fresh MEAs there is an increase in the radius of the semicircle as O_2 concentration decreases. Additionally, there is also a decrease in the value of the apex frequency. As the sample is degraded, the semicircle radius increases for a given partial pressure of oxygen. However, in line with the results in Figure 4-7, the semicircle-radius for the PtC10 in 13% oxygen experiences a much larger increase than all the others.

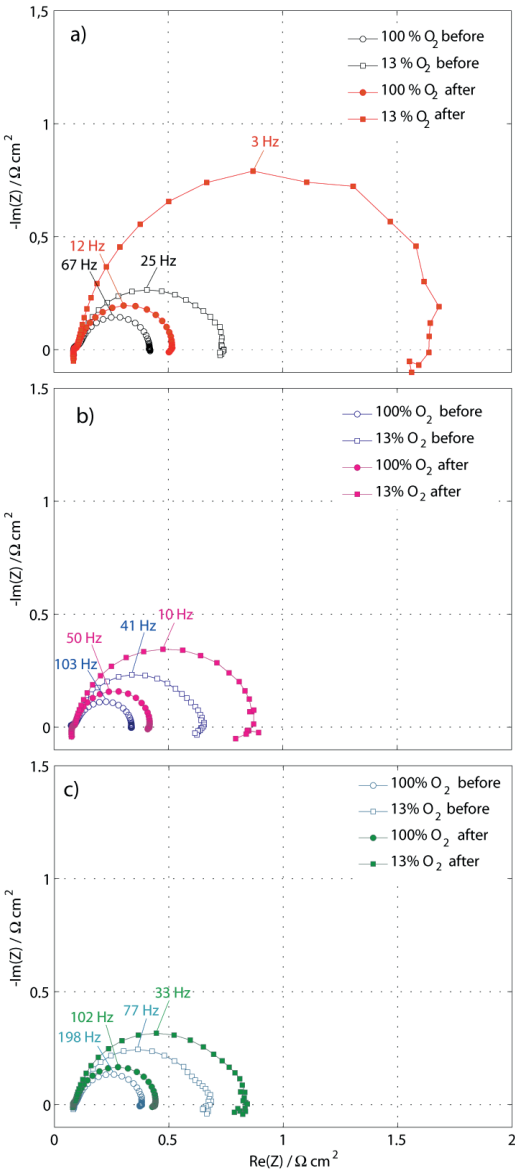

FIGURE 4-8: Nyquist plot using diluted O_2 at 0.2 Acm^{-2} before and after ADT. a) PtC10, b) PtC20 and c) PtC30. Conditions: atmospheric pressure, 80 °C temperature, fully humidified gases with a flow rate of 60 $mlmin^{-1}$ of O_2 fed to the WE and 120 $mlmin^{-1}$ of H_2 fed to the CE/RE.

TABLE 4-4: Real impedance, apex frequency and iR-corrected voltage at 0.2 Acm^{-2} from the EIS measurements using pure and diluted O_2

		R(Z) (mΩ cm²)			Apex Frequency (Hz)			iR-corrected voltage (mv)		
Sample	**% O_2**	**Before**	**After**	**% Increase**	**before**	**After**	**% Decrease**	**Before**	**After**	**% Decrease**
PtC10	100	327	423	29	67	12	82	701	608	11
	13	649	1542	138	25	3	88	559	416	26
PtC20	100	263	334	27	103	50	52	735	698	6
	13	577	793	37	41	10	76	615	540	12
PtC30	100	288	350	22	198	102	49	720	673	7
	13	587	763	30	77	33	57	587	526	10

Although in principle consistent with both mass-transport and kinetics being affected by the ADT, our results indicate that changes in kinetics are the main factor causing reduced performance. The impedance data contain no features consistent with diffusion limitations, such as sloped straight lines [117], and the inductive feature at low frequencies also indicate that the spectra are completely dominated by kinetics [178][179]. Secondly, the current density employed is much smaller than any limiting current density. In addition the main parts of the mass-transport losses are usually explained in the literature to originate in the GDL and gas channel due to diffusion limitations and depletion, respectively[180][181][182]. These are assumed to be unchanged upon exposure to the ADT.

A kinetic explanation for the degradation can also explain the large difference at low partial pressures of oxygen between the three different thicknesses employed here, where the thick (PtC10) sample is much more sensitive than the others in the low p_{O2}-range. We assume that locally the current obeys a Tafel relation described by the constant a_T and the Tafel slope b_T. We also assume that the CCL is characterized by a specific surface area a (cm^{-1}) per volume V. The measured quantity is the total current I_T divided by the geometric area A_g and is what is kept constant in the experiments, and so

$$\frac{I_T}{A_g} = \frac{aVi}{A_g} = \frac{aV}{A_g} 10^{(\eta - a_T)/b_T} \qquad (4\text{-}3)$$

from which the polarization resistance of the ORR (R_{pol}, in units of Ωcm^2) can be expressed by linearizing the current-potential curve. The change in polarization resistance before and after degradation, ΔR_{pol}, thus becomes,

$$\Delta R_{pol} = \Delta\left[\frac{\partial\eta}{\partial\left(I_T / A_g\right)}\right] = \frac{A_g}{VI_T}\Delta\left(\frac{b_T}{a}\right) \qquad (4\text{-}4)$$

The change in the polarization resistance is therefore dependent on any change in the specific area. Eq. (4-4) predicts that if the volume-specific area a decreases or the Tafel slope b_T increases so that $\Delta(b_T/a)$ increases there will be an associated increase in ΔR_{pol}.

A decrease in the specific surface area would thus explain the increase in the polarization resistance in Figure 4-6 and Figure 4-8. It would not, however, explain the rather large change in ΔR_{pol} in Figure 4-7 for PtC10 in air as compared to the same sample in oxygen, since a change in a should lead to the same change in ΔR_{pol} in both cases. Therefore, we seek an explanation in changes in b_T.

Pursuing this line of argument, we consider the break in the polarization curve and change in the Tafel slope frequently observed for the ORR [183][184][185]. For example, Parthasarathy et al. [183] observed that for a Pt microelectrode the kinetics of the electrochemical reactions is significantly dependent on the oxygen partial pressure. In their work the Tafel slope changed from approximately 60 mV to 120 mV above a certain critical current density ($i_{critical}$) for Pt, $i_{critical}$ being a function of the oxygen partial pressure.

In Figure 4-9 we plot the results for the critical current density, $i_{critical}$, separating the low and high Tafel-slope regimes as a function of p_{O2} as we estimate them from the data in [183]. The 10% error in the measurement of the pressure as Parthasarathy et al. reported is also taken into account.

As the partial pressure decreases, the current density tends to switch from low to high Tafel slope at the critical current density as given in Table 4-5. In the figure we also give the current-density before the degradation and after degradation experienced by the catalyst particles in our MEAs, based on the estimated active catalyst area. (The active area was estimated by dividing the transferred charge in CO oxidation region, $Q(CO)$, in CO stripping by the $Q(CO)_{UPD}$. Local current densities for the three electrocatalysts are listed in Table 4-5. The current densities for PtC20 and PtC30 are patently less than those of PtC10 both before and after degradation.

TABLE 4-5: Local current densities values for the three electrocatalysts.

	Local current density (Acm^{-2}) before		Log(i)		Local current density (Acm^{-2}) after		Log(i)	
Sample	**@ 0.2 A**	**@ 1 A**	**@ 0.2 A**	**@ 1 A**	**@ 0.2 A**	**@ 1 A**	**@ 0.2 A**	**@ 1 A**
PtC10	0.00013	0.00068	-3.861	-3.162	0.00029	0.00149	-3.523	-2.824
PtC20	0.00006	0.00031	-4.198	-3.499	0.00013	0.00067	-3.868	-3.169
PtC30	0.00005	0.00029	-4.231	-3.532	0.00011	0.00059	-3.927	-3.228

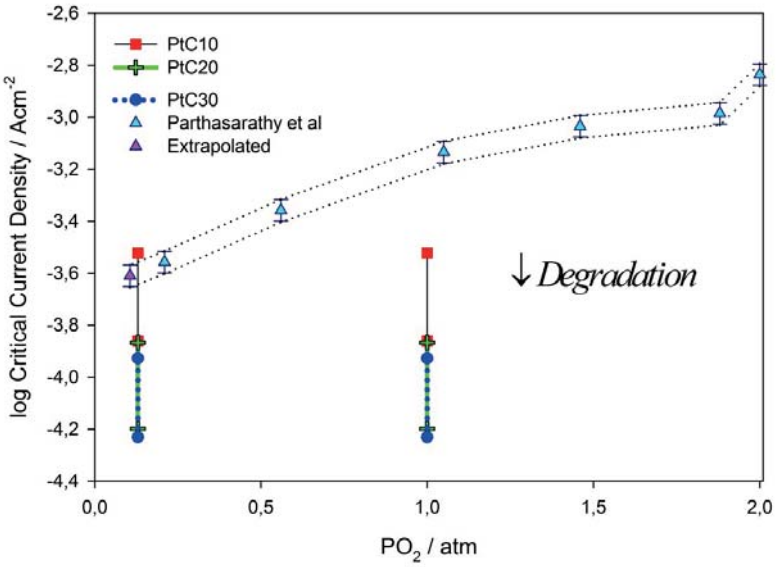

FIGURE 4-9: Critical current density for different oxygen partial pressures with potential cycle between 0.06 and 1.5 V in 50 °C adapted from reference [183] and the change in local current density upon degradation for the three electrocatalysts using the values in Table 4-5. The direction of degradation is illustrated by the arrow.

At low oxygen partial pressures it appears that local current density before and after degradation spans the critical current density for the PtC10 sample. This is not the case for two other catalysts and for high oxygen partial pressures of oxygen (i.e.100%) for all samples. In terms of Eq. (4-4) and if b_{PtC10} (before degradation) < b_{PtC10} (after degradation) while b_{PtC20} and b_{PtC30} remain unchanged upon ADT, we would have:

$$\Delta R_{pol}(PtC10) \gg \Delta R_{pol}(PtC20, PtC30) \qquad (4\text{-}5)$$

We therefore suggest this as a possible explanation for why the degradation appears to be so severe at low partial pressures of oxygen compared to higher oxygen partial pressures

and for the other two samples. Since the Tafel slope doubles according to [183] the polarization resistance would be expected to at least double also. (The change in the specific surface area would cause an additional change over this factor of two from the change in Tafel slope alone, Eq. (4-1)). For PtC10 the polarization resistance thus changes by a factor of 2.4 in 13% O_2 but only by a factor of 1.3 in 100% O_2. For sample PtC20 the polarization resistances change by factors in the range 1.2-1.3, in reasonable agreement with the results in Figure 4-9. Table 4-6 summarizes the polarization resistance values and their corresponding increase upon ADT.

TABLE 4-6: Polarization resistance increase upon degradation for the three samples (data extracted from Figure 4-8).

Sample	**Rp + Rs (mΩ cm²)**				**Rp (mΩ cm²)**		
	% O_2	**Before**	**After**	**% Increase**	**Before**	**After**	**% Increase**
PtC10	100	426	529	24 %	337.75	440.75	30 %
	13	742	1661	124 %	653.75	1572.75	141 %
PtC20	100	338	419	24 %	249.77	330.77	32 %
	13	654	875	34 %	565.77	786.77	39 %
PtC30	100	382	441	15 %	293.8	352.8	20 %
	13	684	831	21 %	595.8	742.8	25 %

Figure 4-10 shows a plot of critical current density along with data for the local current density when the current density relative to the geometric area is 1 Acm^{-2}. Again, the PtC10 sample is likely to cross the critical current density locally, which also in this case would explain the much larger leap in the polarization resistance for this sample than for the other two.

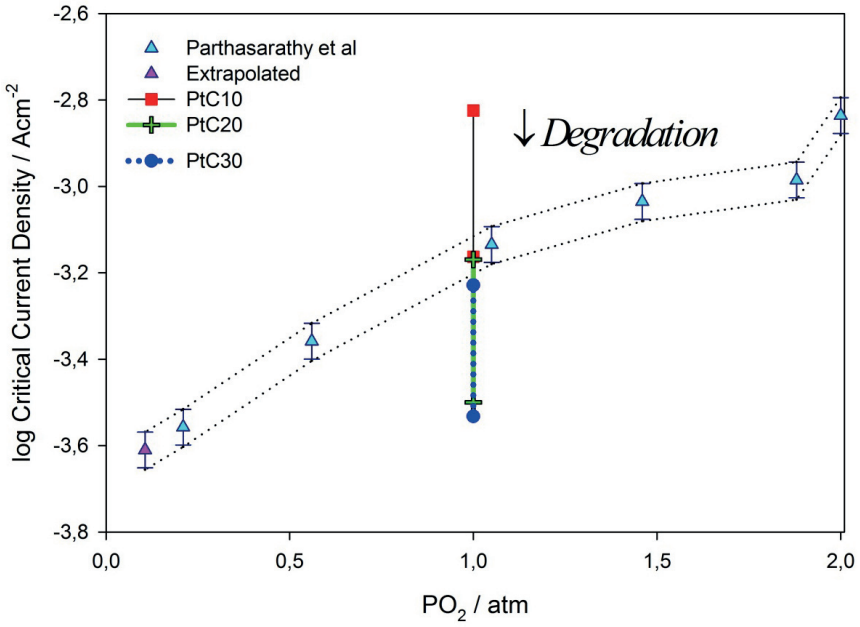

FIGURE 4-10: Critical current density for different oxygen partial pressures with potential cycle between 0.06 and 1.5 V in 50 °C adapted from reference [183] and the change in local current density upon degradation for the three electrocatalysts for the 1 Acm^{-2} situation and pure oxygen as the conditions in Figure 4-6. The direction of degradation is illustrated by the arrow.

4.3.4 Morphological changes due to ADT

Figure 4-11 shows the SEM images of cathode cross-sections for pristine and degraded electrocatalysts while Figure 4-12 also presents the morphology of the cathodes for the electrocatalysts before and after the ADT. As expected, there are clear differences in the average thickness between the three fresh CCLs due to the differences in carbon content. The layers are thinner after the experiments, which may in principle be due to carbon corrosion or MEA reorganization. The average thicknesses of the electrodes decrease 35%, 37% and 36% for the PtC10, PtC20 and PtC30, respectively (Table 4-7) and the thickness reduction is thus quite similar for all samples.

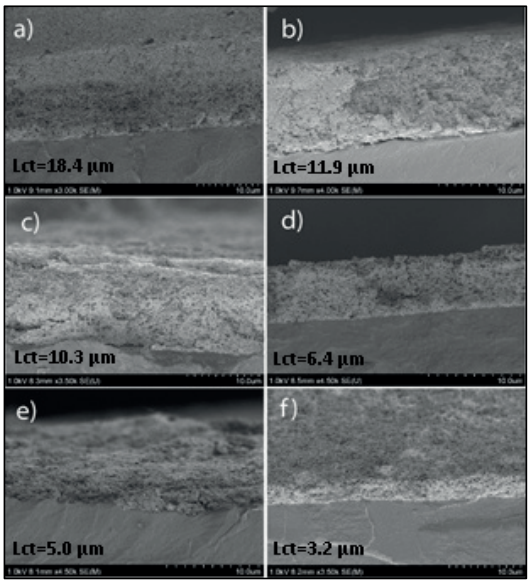

FIGURE 4-11: SEM images of cathode cross-sections before and after the ADT: a) PtC10 before, b) PtC10 after, c) PtC20 before, d) PtC20 after, e) PtC30 before and f) PtC30 after.

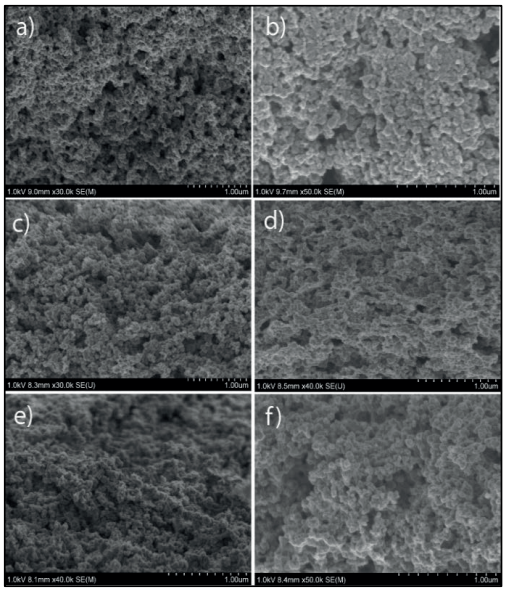

FIGURE 4-12: SEM images of cathode morphology before and after the ADT: a) PtC10 before, b) PtC10 after, c) PtC20 before, d) PtC20 after, e) PtC30 before and f) PtC30 after.

Table 4-7: CCL loadings and resulting thicknesses.

Sample	Pt mg cm^{-2}	C mg cm^{-2}	Nafion mg cm^{-2}	Nafion wt%	L_{before} µm	L_{after} µm	Decrease %
PtC10	0,1	0,9	0,72	42	18.4	11.9	35
PtC20	0,12	0,48	0,38	39	10.3	6.4	37
PtC30	0,11	0,26	0,21	36	5.0	3.2	36

The CCLs not only experience a considerable decrease in the average pore size, but also in the pore size distribution (also estimated from SEM images), as seen in Figure 4-13. There are clear indications that the majority of the pores larger than 100 nm disappear during the ADT and there is a larger count of pores smaller than 50 nm.

As Figure 4-13 shows the reduction of pore size for the catalysts are not significantly different. This indicates that the large polarization resistance seen from PtC10 in Figure 4-6 and Figure 4-8 can be difficult to relate to oxygen diffusion since we should have observed a much larger reduction in pore size for PtC10 compared to PtC20 and PtC30 if this was the case.

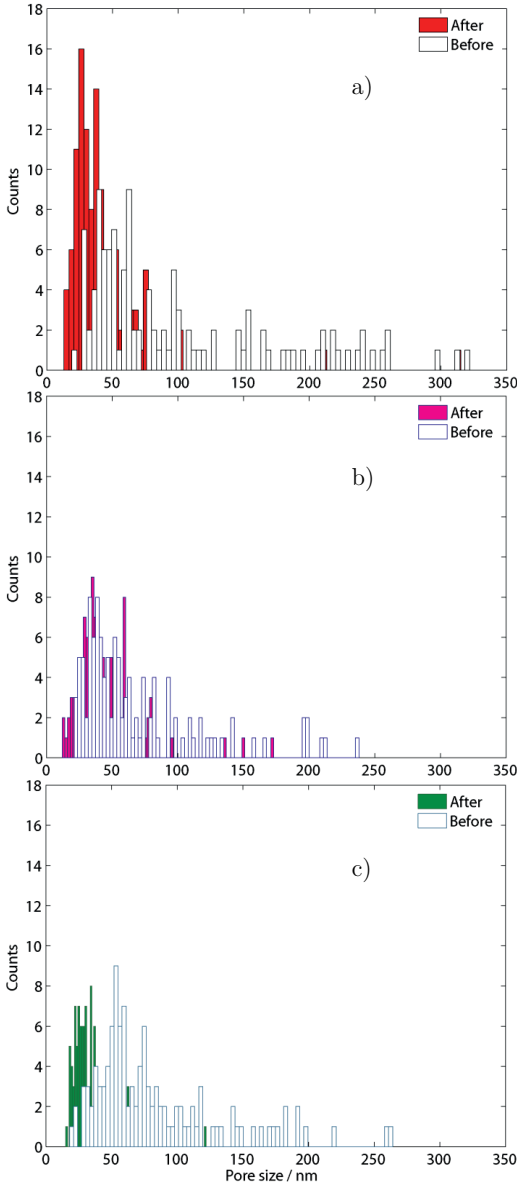

FIGURE 4-13: Pore size distribution estimated from SEM images using image software ImageJ. a) PtC10, b) PtC20 and c) PtC30.

4.3.5 In-situ CO stripping and half-cell measurements in N_2

Figure 4-14 shows the results for in-situ CO stripping of the three samples before after the ADT.

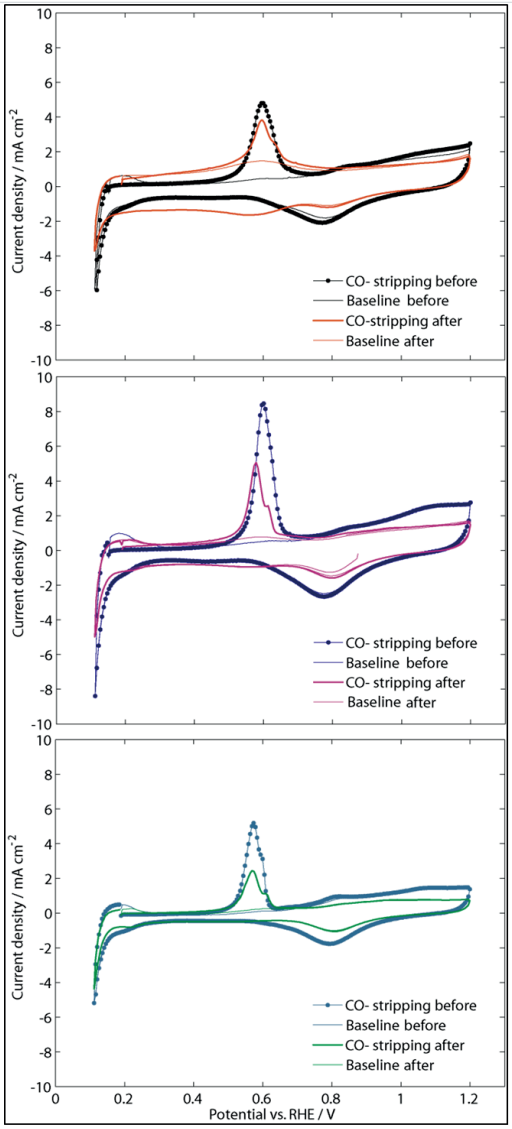

FIGURE 4-14: Cyclic voltammetry and CO stripping before and after ADT. a) PtC10, b) PtC20 and c) PtC30. Conditions: temperature 80 °C, fully humidified gases with a flow rate of 60 $mlmin^{-1}$ of N_2 fed to the WE and 120 $mlmin^{-1}$ of 5 % H_2/Ar fed to the CE/RE, sweep rates 20 mVs^{-1}.

For the pristine samples, the CO oxidation peaks are narrow and single type for PtC10 and PtC20 and show a minor shoulder for PtC30. After the ADT however, all samples exhibit a double peak at CO oxidation region, which according to the findings of Maillard et al. [69] may be related to agglomeration of catalysts.

Table 4-8 summarizes the in-situ CO stripping results for the three MEAs before and after the ADT. Initially PtC20 has the highest ESA, slightly more than that of PtC10, while sample PtC30 has the lowest ESA. For PtC30 this correlates with the significantly larger particle size (Table 4-1) of this catalyst. The ESA of PtC10 is lower than that of PtC20, however, although the particle size of the former is smaller than that of the latter. While the difference is rather small, we assume that this is related to factors not captured by size alone such as shape, agglomeration, experimental uncertainty etc. As seen in Table 4-8, the loss of ESA is 46%, 47% and 50% for PtC10, PtC20 and PtC30, respectively. It thus appears that the almost 50% decrease in ESA translates to disproportionately lesser loss in the performance, see Figure 4-2 and Figure 4-3.

Table 4-8: Results from in-situ CO stripping before and after ADT.

Sample	ESA before (m^2g^{-1}) (CO)	ESA after (m^2g^{-1}) (CO)	Difference (m^2g^{-1})	% Decrease
PtC10	40.3	21.8	18.5	45.9
PtC20	46.1	24.6	21.5	46.7
PtC30	29.5	14.8	14.7	49.7

In summary, we thus observe a number of changes in the catalyst due to the ADT which are relatively easily explained as a loss of Pt surface area. The differences between the various catalysts are not very large as long as the oxygen content in the cathode gas is high, although a slightly more severe degradation is seen in the sample containing the lowest Pt loading. This is opposite to the TPO results (Figure 4-2 and Figure 4-3) for which the process is known to be carbon corrosion. Because of this opposite correlation it is quite clear that the electrode ADT-induced degradation process observed here cannot be limited to carbon corrosion. Some reorganization of the supported catalyst during the ADT is to be expected, though.

EIS in N_2 was performed at 0.35 V vs RHE. Figure 4-15.a, Figure 4-15.c and Figure 4-15.e show the changes in capacitance plotted as a function of frequency, for PtC10, PtC20 and PtC30, respectively. Figure 4-15.b, Figure 4-15.d and Figure 4-15.f present the Nyquist plots, for PtC10, PtC20 and PtC30, respectively.

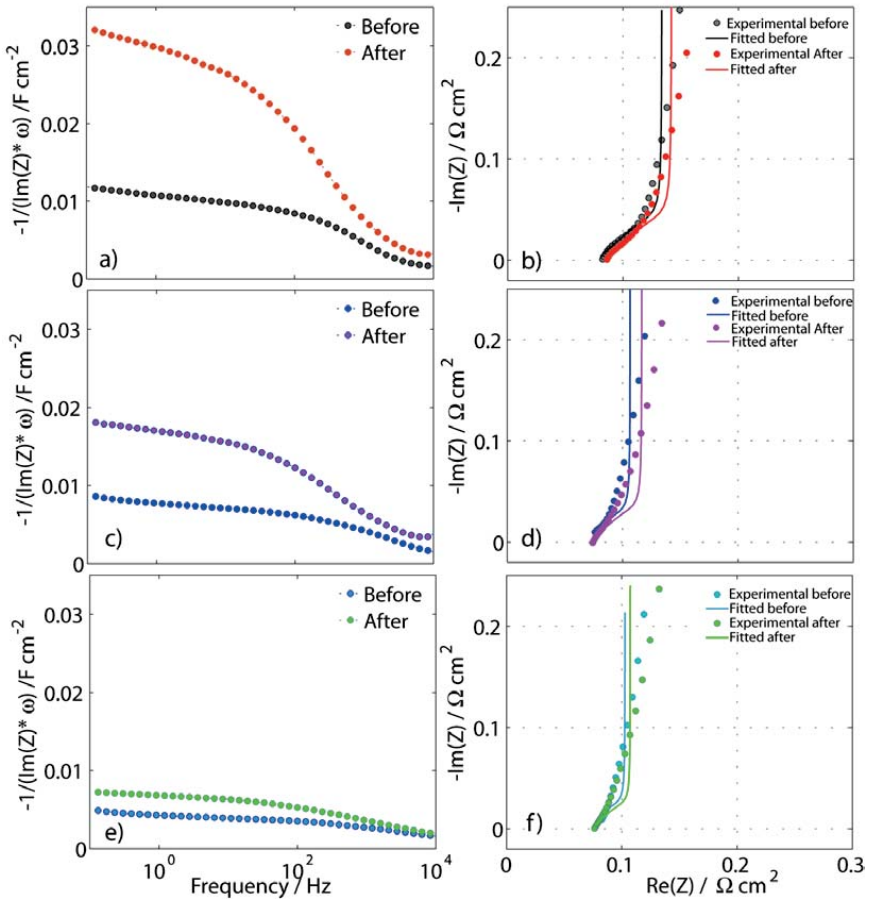

FIGURE 4-15: EIS measurements in N_2 before and after ADT: a) PtC10 capacitance plot, b) PtC10 Nyquist plot, c) PtC20 capacitance plot, d) PtC20 Nyquist plot, e) PtC30 capacitance plot and f) PtC30 Nyquist plot. Conditions: the same as in Figure 4-14. EIS conditions: alternating voltage 10 mV (top) at 0.376 V vs RHE by varying the frequency between 10 kHz and 0.1 Hz.

The EIS in N_2 data was analyzed using Eq. (21) in [119]. At high frequencies, the model suggests a 45° zone and then a vertical line at low frequencies. the real part of the impedance *(Re(Z))* ideally converges to $L/3\sigma_{eff}$ [119] or $R_i/3$ [186] where σ_{eff} is the effective conductivity, R_i is ionomer resistance of the CCL and L is cathode thickness. The electrode thickness was estimated from the cross sectional SEM images before and after the ADT for the corresponding values of fresh and degraded catalysts. These values are listed in Table 4-9.

Although the experimental data do not perfectly match with the model behavior at low frequencies, the high frequency zone, exhibiting 45° features, was considered to comply with the model.

Electrode capacitance, $C_{electrode}$, was also calculated as $1/\left(-\mathrm{Im}(Z)*\omega\right)$ according to Easton and Pickup [187].

TABLE 4-9: Results from EIS in N_2

Parameter	PtC10		PtC20		PtC30	
	Before	After	Before	After	Before	After
C_{dl} ($mFcm^{-2}$)	10.8	29.6	7.8	17.1	4.3	6.8
$R_i/3$ ($m\Omega cm^2$)	46.6	56.2	27.9	32.3	14.1	16.4
R_i ($m\Omega cm^2$)	140	169	84	97	42	49
σ_{eff} (Scm^{-2})	1.32	0.71	1.23	0.66	1.18	0.65

The results in Table 4-9 display a modest increase in the electrode resistance in all cases. The thinning of the CCL does therefore not translate into smaller resistances across the layers, and must be ascribed to either some increase in contact resistances or loss of water [188]. The changes in the capacitance are significant, however, and the capacitances become much larger after the tests than before for all three samples. This is at odds with the decrease in the surface area observed here. Following reference [188], however, the increase in the double layer capacitance may be due to chemical changes due to for example carbon corrosion in the layer, leading to the presence of carbon species with oxygen functionalities assembling at the carbon surface, which in turn lead to larger values for C_{dl} [188]. Apparently, the duration of our experiments is too short to observe the area losses outcompeting the changes in the specific values for the double-layer capacity, as was for instance seen in reference [188].

4.4 Conclusion

Three Pt/C cathode electrodes for PEMFCs with Pt loadings of 10%, 20%, and 30%, were synthesized by the polyol technique. Electrodes were prepared from these all containing approximately the same total amount of Pt, that is the electrodes contained different total amount of carbon and therefore the electrode thicknesses were also different. These electrodes were comprehensively characterized ex-situ (physically and electrochemically) and in a fuel cell set-up before and after being subjected to an accelerated degradation protocol.

We found that the initial electrochemical activities were independent of total carbon content, or equivalently independent of catalyst layer thickness for the range of electrode thickness in this study.

The activity of all CCLs experiences a significant decrease when subjected to the accelerated degradation protocol, both in pure oxygen and in diluted oxygen. Polarization curves and impedance spectra recorded in pure oxygen shows a reduction in catalytic activity approximately independent of the Pt-to-carbon ratio. In diluted oxygen, however, polarization curves and impedance spectra showed a reduction in catalytic activity due to the acceleration test strongly dependent on the Pt-to-carbon ratio. In this case there was a much larger reduction in cell voltage with the catalytic layer containing 10 wt% Pt and 90 wt% carbon than the other two.

We resolve the conflict between these latter results and the fact that there is a significant change in the electrochemical results in diluted oxygen by pointing to the local current density and using the fact that polarization curves for the oxygen-reduction reaction frequently displays a change in Tafel slope at intermediate current densities. For low Pt loading the degradation protocol may cause the local current density to pass from one Tafel regime (before the degradation) to another (after the degradation), whereas at high Pt loading the local current density remains within the same Tafel regime also after the degradation.

The TPO results indicate that the carbon degradation is catalyzed by Pt to a degree depending on loading and therefore in principle also with the other quantities correlating with loading such as particle size. Since the accelerated degradation of the samples appear to cause a degree of deactivation independent on Pt loading, at least in oxygen atmospheres, the process of degradation is likely to be dominated by factors other than carbon corrosion.

4.5 **Acknowledgments**

The assistance from Per Erik Vullum and Yingda Yu with TEM imaging is appreciated. This work was performed within the N-INNER project “Nanoduramea – synthesis and durability of CNT-based MEAs for PEMFC” and financially supported by the Research Council of Norway under contract no 187142/S30 and the Department of Materials Science and Engineering, NTNU.

Chapter 5

Pt Dispersion and FC Performance

In this chapter the variations of the electrochemical performance with respect to pure singular Pt particles, a film of networked nanoparticles and a mixture of individual particles and aggregated ones are presented with relations to fuel cell performance and durability. The fuel cell performance for these catalysts was studied before and after an accelerated degradation test.

The chapter is partially published in ECS Transactions, 50(2) 1353-1367(2012)
(reproduced here by permission of ECS - The Electrochemical Society) and the rest of the data is intended for another publication.

5.1 Introduction

To overcome the cost issue as a major barrier limiting the large-scale commercialization of proton exchange membrane To commercialize low temperature fuel cells operating below 100 °C including proton exchange membrane fuel cells (PEMFCs) we still need them to make electricity at lower cost [11][189]. A quite active approach to address the cost issue has been optimal utilization of the precious metals in the electrocatalysts while improving the durability of the catalysts in general [105][82][190].

With respect to building durable electrocatalysts for PEMFCs, there are at least two degradation regimes to be taken into account; loss of active Pt surface area and carbon support corrosion [75]. An efficient way to study degradation under varying operational conditions is to monitor changes in properties of the catalysts critical to its performance during a provoked protocol. During such a protocol the degradation of the electrocatalyst can be physically simulated so as to reflect real fuel cell operating conditions [191].

Surface and atomic scale approaches have dramatically improved the understanding of catalytic properties of fuel cell catalysts [74][192][193]. However, durability of PEMFC catalysts and catalytic layers appears to have attracted less attention from this part of the scientific community. Durability studies therefore remain an experimental and application-oriented activity [32][67][194]; although some studies of a more fundamental nature have also appeared. In this regard compromises have to be struck for parameters such as the Pt particle size, its distribution and dispersion of the metal on the carbon support since they typically affect reactivity and durability oppositely [41][195][196].

In the current study the different orientations of localized Pt particles over the carbon support was observed basically in three categories with respect to transmission electron microscopy images, demonstrating three surface metallic dispersions: i) solely individual platinum nanoparticles, ii) a mixture of isolated and aggregated platinum particles and iii) a film of inter-networked platinum nanoparticles. It is now well established that agglomeration and grain boundaries affect the CO stripping by inducing a second stripping peak at lower potentials than that observed for catalysts without such agglomeration [69]. While there are well known correlations of this nature between the ex-situ electrochemical performance of electrocatalysts with different platinum particle dispersion [32][69][134], available in-situ fuel cell results do not allow for similarly strong correlations to be drawn. This is maybe not yet a well-developed field in terms of gauging the influence of such catalyst characteristics in-situ in a PEMFC.

In this study we seek to reveal the dependence of fuel cell performance of MEAs with their platinum particles orientation and isolation in the catalysts layer in-situ in PEM single cells. The samples were synthesized by utilizing two different techniques on high surface carbon black and treated graphitized carbon nanofibers (GNF). This way we were able to achieve three types of the Pt particle dispersions on the support. Each catalyst was tested in both liquid electrolyte cells and fuel cell set-up under identical experimental conditions for al samples. The in-situ data were acquired both before and after a degradation protocol to simultaneously study the fuel cell performance and durability as a function of particle dispersion. It will be shown that the catalysts whit only isolated Pt particles have higher initial fuel cell performance but relatively lower durability comparing to catalysts with aggregated Pt particles. The samples with film-coat Pt nanoparticles supported on nanofiber also have performance and durability in between the values for catalysts with aggregated particles and pure singular particles.

5.2 Experimental

5.2.1 Electrocatalyst synthesis

A modified polyol and an adsorption polyol technique were utilized for synthesizing the catalysts samples with an appropriate control over the particle size and particle dispersion in the support. Materials and solvents were obtained from commercial suppliers and were used without further purification. Carbon black (Vulcan XC72, CABOT Corporation), hexachloroplatinate (IV) (Johnson Mattey, Pt content: 39.76 %, purity ≥ 99%), Sodium Hydroxide (VMR, purity ≥ 99%), ethylene glycol (Sigma-Aldrich purity ≥ 99%), isopropanol and acetone in analytical grades were used for the synthesis. Solutions were diluted with distilled water (18MΩcm conductivity, MilliQ System).

To synthesize the 15 wt% Pt/C (Vulcan XC-72) by polyol method, ethylene glycol were kept at 50 °C for ½ hour. While nitrogen was flowing in the reactor, platinic acid, already dissolved in ethylene glycol to make a shining yellowish solution, was added to the mixture whilst the temperature was increased to 110 °C. The mixture was kept at elevated temperature for 1½ hours followed by a cooling step in the air and centrifuging the catalyst, ultrasonic homogenization and washing with water and acetone. The sample was dried at 80 °C for 8 hours to shape the final catalyst. 20 wt% Pt/C sample was synthesized in accordance to the reference [101] with a colloidal polyol method where Pt solution was prepared first followed by an introduction of suitable volume of the solution to carbon supports solution then mixed under extensive ultrasonication and controlled pH.

In addition to the synthesized samples, the sample Pt/GNF which was made by polyol method with chloroplatinic acid and pretreated graphitized carbon nanofibers with 4M H_2SO_4 at 120 °C for 8 hour was obtained from the project partner, Aalto University.

The samples used for this study are then 15 wt% platinum on carbon black Vulcan XC-72 (XC15), 20 wt% platinum on carbon black Vulcan XC-72 (XC20) and 23 wt% platinum on graphitized carbon nanofibers (GNF23).

5.2.2 Physical characterization

The resultant electrocatalysts were extensively studied by physical techniques to gather the necessary information on their structures. Transmission electron microscopy (JEOL-JEM2010) was performed to estimate the particle size and study the metal distribution on the support. TEM was also applicable to check the presence of aggregates or isolated platinum nanoparticles in the catalysts. Thermal gravimetric analysis (NETZCH, STA 449 °C) was also used to evaluate the purity of the material and to examine the actual metal loading.

5.2.3 Ex-situ electrochemical measurements

The ex-situ characterization including cyclic voltammetry (CV) and CO stripping was carried out in a classical three electrode cell at room temperature in Ar. The reference electrode was a reversible hydrogen electrode (RHE) connected to the cell. The counter electrode also was a 1.5 cm^2 plate of platinum. The working electrode was a glassy carbon (GC) electrode that the dispersed catalysts as ink and Nafion® were coated on its surface. Here the catalyst ink was prepared by sonication of 1.0 mg catalyst in 1.0 mL of distilled water. 20.0 µL of the catalyst ink was pipetted then on the disk-type GC and dried in N_2 followed by addition of 20 µL Nafion®. The area of the GC electrode used in the experiment was 0.1962 cm^2. An Autolab potentiostat type PGSTAT302N along with the three electrode cell equipped with necessary inlet connections for Ar and CO was used in this experiment. The CV data were acquired at room temperature and a sweep rate of 10 mVs^{-1}.

The CO adsorption was sparked after a potential loop at 50 mV and CO exposure for 120 seconds. There was an Ar purge step hereafter to remove the dissolved CO, leaving the working electrode with an adsorbed monolayer of carbon monoxide. $HClO_4$ 0.5 M was used as electrolyte.

5.2.4 MEA fabrication and fuel cell testing

The synthesized powder of the catalysts together with the ionomer and isopropanol with an optimized ratio comprised the catalyst's ink. The ink was then evenly sprayed on the membrane with an airbrush, and this assembly was hot-pressed together with the gas diffusion electrode at 130 °C and 1000 psi for 1 min, whereas the GDL on the target electrode was simply added into cell while assembling.

MEAs were built using the synthesized catalysts and commercial gas diffusion media (SIGRACET® gas diffusion media, type GDL 10 BC), Nafion® membrane PFSA NRE-211 and ETEK Pt/C commercial catalysts as the supplementary electrode.

A PEM single cell, with an active area of 5 cm^2, was assembled from the already made MEAs in the PEMFC lab at NTNU with Teflon gaskets and the flow fields on both sides of the MEA. The cell was uniformly tightened using eight stainless steel screws.

The polarization curves were recorded using an Agilent N3300A system. The anode was supplied with a stoichiometric gas flow of hydrogen (99.999% purity) and the cathode with oxygen (99.5% purity) with a minimum flow rate of 0.1 $l_n min^{-1}$ and 0.2 $l_n min^{-1}$ respectively to avoid any gas starvation. The gases were humidified in separate sparge bottles with 90% RH. The cell was operated at 80 °C however to ensure inhibiting gas condensation in the system the pipes' temperature was set to 82 °C.

In situ cyclic voltammetry were conducted by a Biologic SP-150 potentiostat with a 2A booster. The incoming gases were harmix (mixture of 95% Ar and 5% H_2) on CE/RE and

N_2 (99.5% purity) on WE. The experiment was carried out at 100% RH and room temperature at sweep rate of 100 mVs^{-1}. The same apparatus was used for accelerated degradation test consisting of 100 potential cycles between 0.6 and 1.5 V vs. RHE. The gases were analogous to the cyclic voltammetry experiment and the sweep rate was 40 mVs^{-1}.

5.3 Results and discussion

5.3.1 Transmission electron microscopy

Figure 5-1 shows typical micrographs of the pristine electrocatalysts as synthesized by the techniques described in the experimental section.

The catalyst XC20 appears to contain only individual particles, as well as being devoid of aggregates, being homogeneous and with the particles uniformly dispersion on the support matrix, as exhibited in Figure 5-1.A . Pt particle size is estimated to be around 2 nm in this sample. A closer look at higher magnification, XC20 displays excellent homogeneity in particle distribution over the carbon support, promising for the electrocatalytic activity of this catalyst.

Sample XC15 which was synthesized with an ordinary polyol technique where the precursor and support material are mixed at the same time, depicts to consist of both individual particles with an average extent of isolation and aggregated Pt particles on carbon as demonstrated in Figure 5-1.B. Although in this sample a number of single particles of around 6 nm diameter are observed, islands of aggregates as large as 50 nm can also be found.

A remarkable phenomenon of formation of a film of inter-networked Pt particles over the outer surface of the carbon nanofibers is presented in Figure 5-1.C. An almost complete coverage of the metallic particles with an average diameter of 5 nm is formed on GNF's surface making it appear as a coating of platinum monolayer.

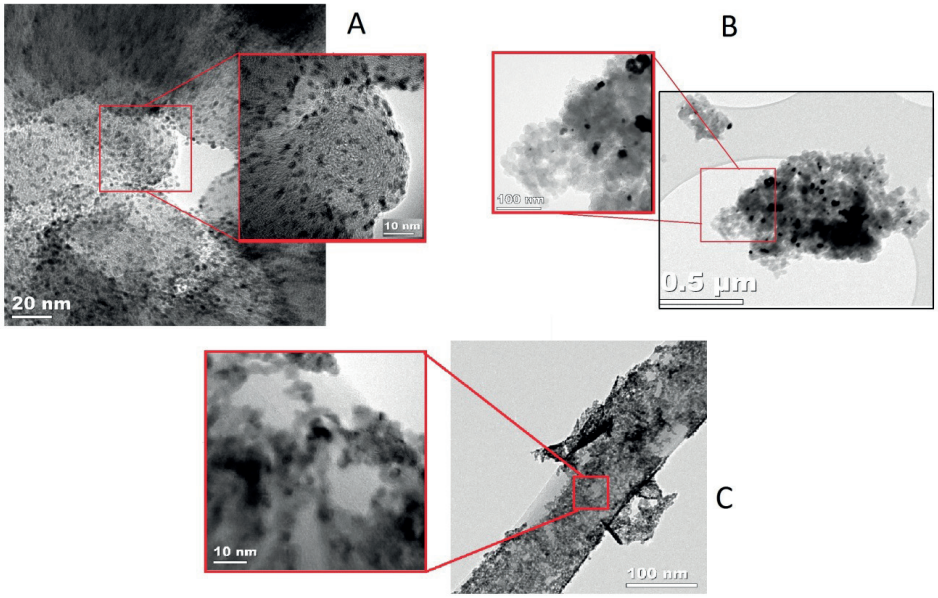

FIGURE 5-1: TEM images for the samples A) 20% Pt/Vulcan XC-72 (XC20 B) 15% Pt/Vulcan XC-72 (XC15) C) 23% Pt/GNF (GNF23).

5.3.2 Ex-situ electrochemical measurements

Ex-situ CO stripping voltammetry results in an acidic electrolyte cell are shown in Figure 5-2 following the same sequence as Figure 5-1. The stripping voltammetry provides valuable electrochemical properties of the samples e.g. onset and peak potential for oxidation. The shape of the oxidation peak (single or multiple peaks) can also be used to provide some information about the Pt particle dispersion [69] which in turn will be coupled with the TEM images.

Figure 5-2.A corresponding to the sample XC20 represents a single narrow peak for the carbon monoxide electrooxidation at around 0.79 V. This agrees with the TEM image of the sample in Figure 5-1.A where isolated particles are a clearly dominant feature of catalyst. As the amount of lumped particles gets significant peak multiplicity [69] in the CO electrooxidation waves is expected. This is precisely seen in Figure 5-2.B, where the two peaks occurring at ~0.72 V and 0.78 V indicate the presence of nearly equally dominant aggregates and individual Pt particles in XC15. The potential peak at higher and lower potential would be attributed to the isolated particles and the aggregated Pt particles in the CO oxidation process, respectively.

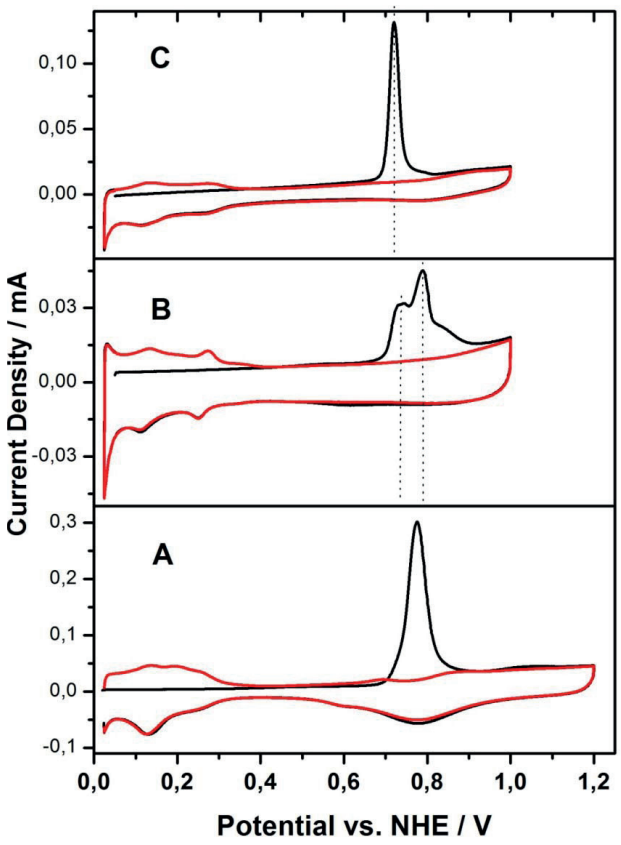

FIGURE 5-2: CO stripping voltammograms at a sweep rate of 10 mVs^{-1} for samples A to C in Figure 5-1. Ar was maintained inside the cell during the experiment at room temperature and the electrolyte was 0.5 M $HClO_4$.

The stripping voltammogram for sample GNF23 displays only a single peak. However, the peak appears at a lower potential, at approximately 0.72 V, than that for sample XC20. As the results in Figure 5-2.C indicates a thin film of metal particles over the surface of the nanofibers, this sample is maybe best compared to that of a Pt film on a substrate [197] which displays a similar potential peak. It was previously reported that there is a positive shift of the stripping peak with the decreasing particle size [197]. The cathodic shift of the oxidation peak at 0.71 V vs NHE then could indicate that the effective size of the Pt particles contributing in the electrooxidation process is larger in GNF23 comparing to two other electrocatalysts. The three peak potentials for the three samples are a characteristic illustration of the three categories of platinum dispersion onto the carbon support; two extreme situations of dominant aggregated particles and

dominant individual particles (GNF23 and XC20 respectively) and an intermediate case of a mixture of aggregates and isolated particles (XC15).

To examine the notion that a covered carbon nanofiber sample with a monolayer of Pt on the surface would electrochemically act as platinum black (unsupported platinum), CO stripping result of a Pt black sample was compared with the one for GNF23 in Figure 5-3. The identical CO oxidation potential at ~0.7V would hypothetically support the conception of similar electrochemical representation at least for the pristine samples of Pt black and GNF23.

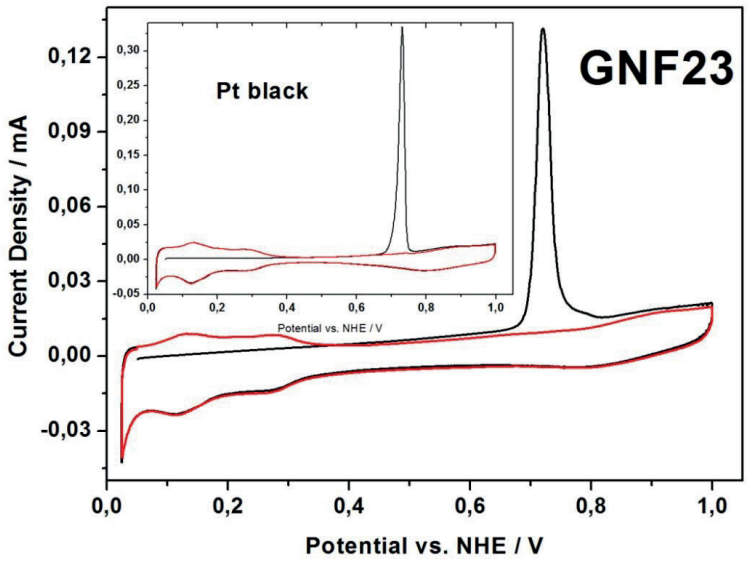

FIGURE 5-3: Comparison of CO stripping voltammograms for Pt black and GNF23. Conditions: sweep rate 10 mVs^{-1}, adsorption at 50 mV vs. RHE, 0.5 M $HClO_4$ and room temperature.

5.3.3 Fuel cell testing

The MEAs of the samples XC15, XC20 and GNF23 as ink of catalyst layer sandwiched between commercial membrane and GDL were studied in-situ. The schematic arrangement of the components of a typical MEA used in this study is shown in Figure 5-4.

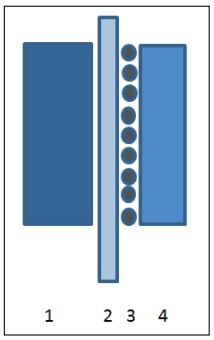

FIGURE 5-4: The schematic structure of the fabricated membrane electrode assembly (MEA) for fuel cell tests: 1) Gas diffusion electrode (ETEK) 2) Polymer membrane (Nafion® 115) 3) Catalyst layer sprayed on the polymer membrane and 4) Gas diffusion layer (SIGRACET® 10 BC). 1, 2 and 3 are hot pressed.

In order to investigate the electrochemical behavior of the three electrocatalysts, a PEM single cell was set to test E-I polarization and in-situ cyclic voltammetry. After the experiments on the pristine electrocatalysts, an accelerated degradation test was conducted. The experiments performed on pristine samples were repeated for the samples subjected to ADT. Figure 5-5 illustrates the fuel cell performance before and after the degradation for the three electrocatalysts.

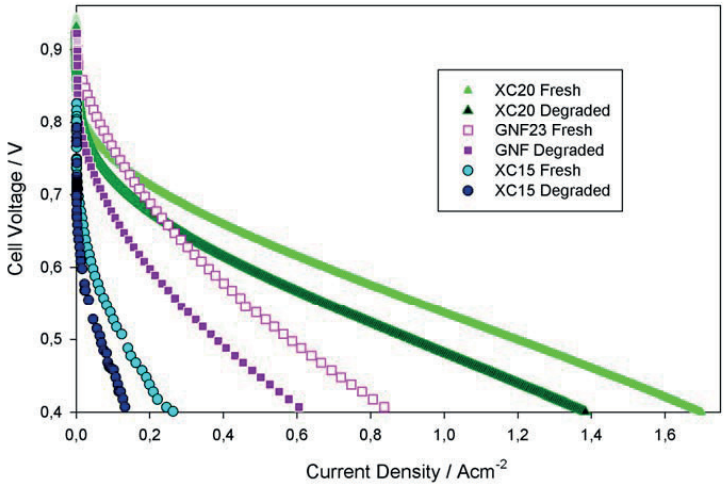

FIGURE 5-5: Polarization curves for the samples A to C in Figure 5-1 before and after the degradation protocol. The potential range: 0.94 V – 0.39 V.

Among the tested samples, XC20 showed the highest initial activity towards the PEMFC reactions as it is visible in Figure 5-5 (light green triangular markers). The aggregate-containing sample, XC15, displayed the poorest initial performance with less than 0.3 Acm^{-2} produced current density at 0.4 V vs. RHE, the lower limit of the potential in the experiment. Considering the I-E curves for the three samples, the initial performance for GNF23 is between the aggregated and isolated particles, higher than XC15 and less than XC20. Although the current density for GNF23 was higher than that with XC20 at the upper potential limit, current density decay for this sample (GNF23) is much steeper than that of XC20 leaving the performance of GNF23 considerably lower than XC20 at the lower potential. At very low current densities (<0.1 Acm^{-2}) where mass transport loss is still negligible [101], the performance of the two catalysts with carbon black support seems to be identical, while in continuation of the experiment the extremely poor performance of XC15 does not comply with the trend.

An important observation here is that the aggregated Pt particles possess a higher capability for resistance against degradation compared to isolated and inter-networked Pt particles. The polarization result after the degradation show that the performance of the degraded electrocatalysts has an obvious drop for XC20 and GNF23 compared to those of the original catalysts and a clear sign of lost activity. Unlike XC20 and GNF23, for sample XC15 the difference between the fresh and degraded catalysts is not significant at lower potentials and is negligible for higher potentials. The probability of coalescence is thus apparently less for already aggregated particles and consequently a higher relative resistance against the ADT is observed for these structures.

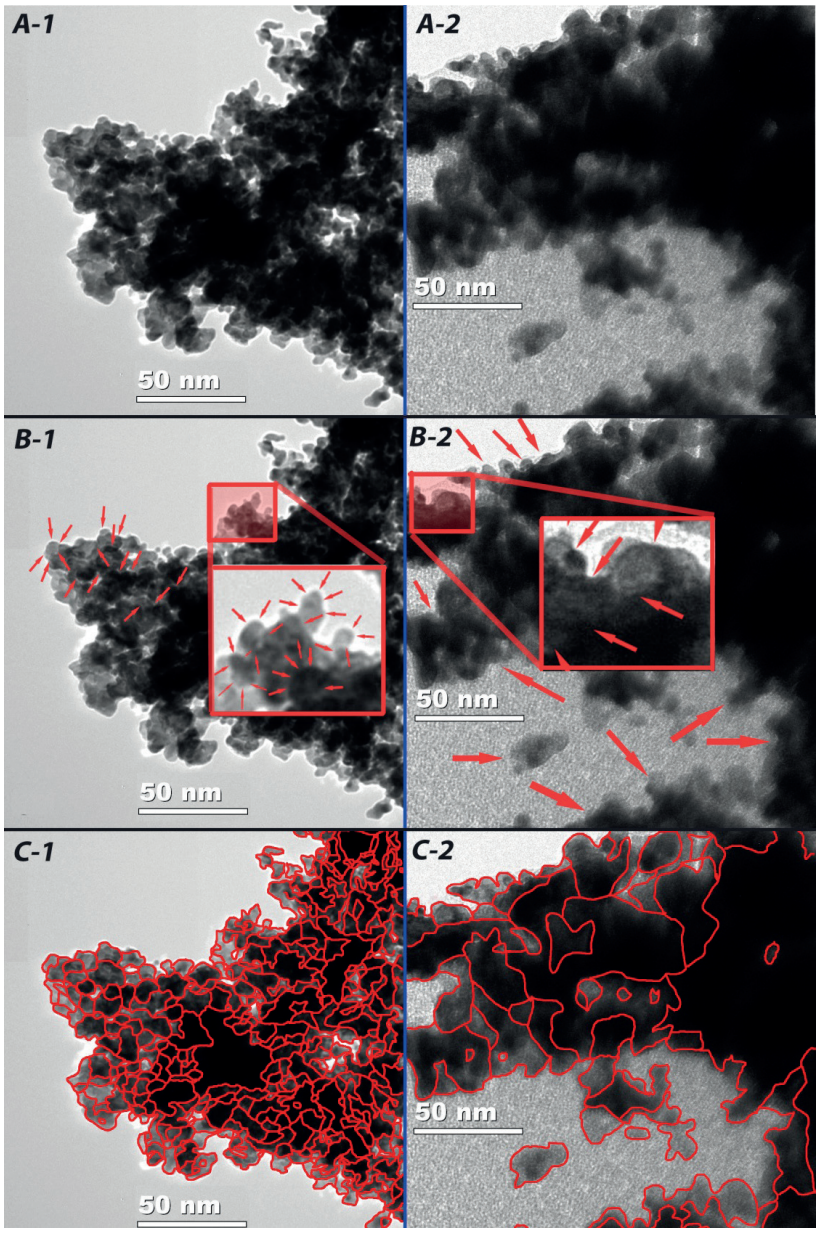

FIGURE 5-6: TEM micrographs at a particular magnification (100K) for the Pt black sample A-1) pristine platinum before starting the cell A-2) Degraded platinum extracted from used MEA after the in-situ degradation protocol. B-1 and B-2) the visual guide used

to estimate the grain boundaries. C-1 and C-2) same TEM micrographs with red lines as estimation of Pt grain boundaries.

The transmission electron microscopy images in Figure 5-6 provide a visual assessment of the extent of degradation for an unsupported Pt sample (Pt black) upon the ADT. The features of the platinum particles shown in Figure 5-6 show an overall coalescence after the degradation. The mean grain size was estimated 6.9±1.5 nm and 20.0±3.5 nm for pristine and degraded Pt respectively.

Figure 5-7 illustrates a comparison for Pt black with GNF23 in degraded and pristine states.

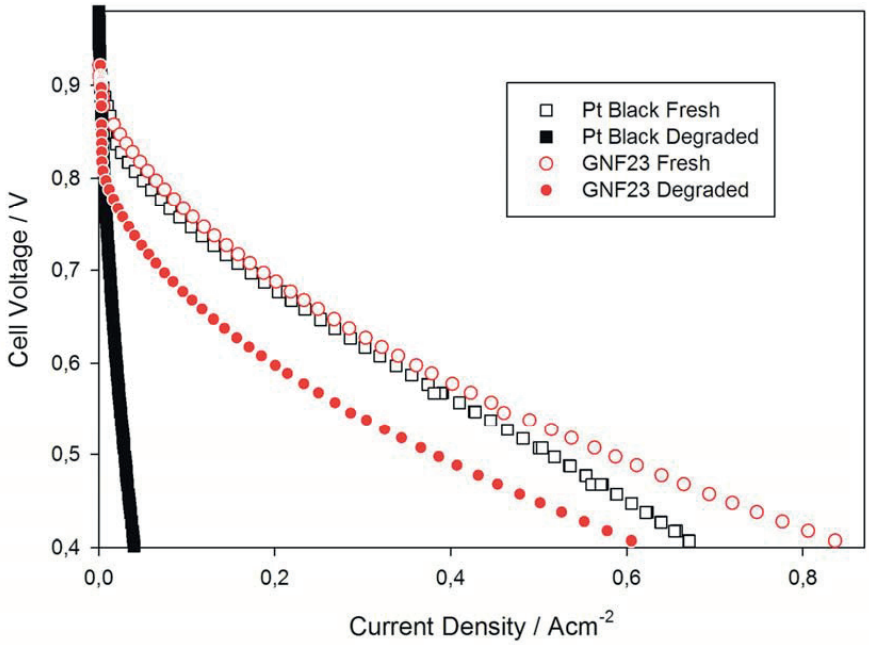

FIGURE 5-7: Comparison of E-I curves for Platinum black and platinum on graphitized nanofibers before and after the degradation with the same experimental conditions as Figure 5-5.

In a wide range of potential (0.94-0.54 V vs. RHE) the initial performance of both catalysts nearly match in an agreement with the electrochemically similar character observed in CO stripping experiment (close peak potentials and comparable peak shapes in Figure 5-3).

The unsupported platinum as one would expect from the dramatic growth in grain size (Figure 5-6.C-2), was severely damaged under the ADT and suffered from a significant drop in electrochemical performance as seen in the polarization curve for degraded

catalysts in Figure 5-7 (black filled square markers). This highlights the important role of support materials for increasing the stability of the electrocatalysts in PEMFC operational conditions.

The very poor performance for the degraded Pt black catalyst observed in the polarization curve was also confirmed with the in-situ cyclic voltammetry results. As it is shown in Figure 5-8, the electrochemically active surface area in the degraded sample is far lower than the one for the fresh sample.

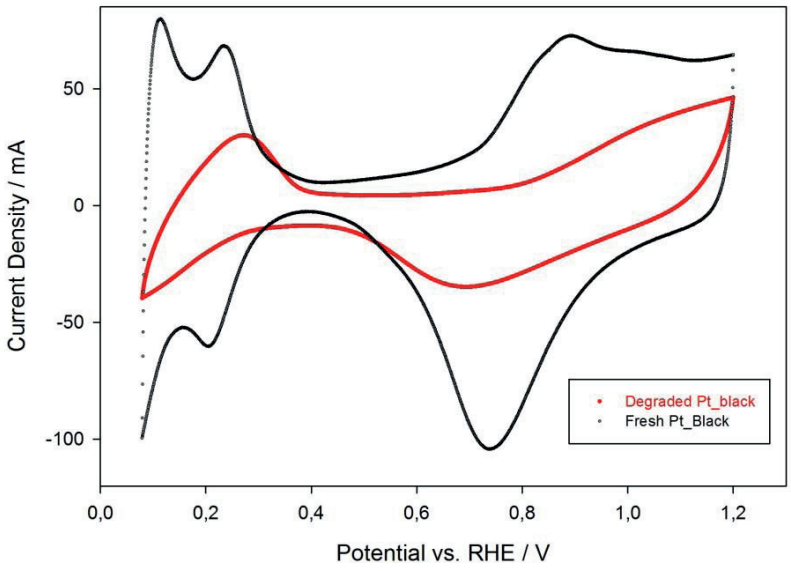

FIGURE 5-8: In-situ cyclic voltammograms for Pt-black sample before and after the degradation. Gases were N_2 on WE and 5% H_2 balanced with Ar on CE/RE and sweep rate was 100 mVs^{-1}. The experiment was carried out at 100% RH and room temperature.

Figure 5-9 gives an overview on the electrochemical activity of the three electrocatalysts by comparing their cyclic voltammograms in the potential range of 0-1.2 V vs. RHE. The CVs fit with the polarization curve data where the electrochemical activity of XC20 is higher than GNF23 at almost all potentials. The Pt aggregation-containing sample, XC15, shows the lowest activity in CVs in a comparable custom to I-E measurements.

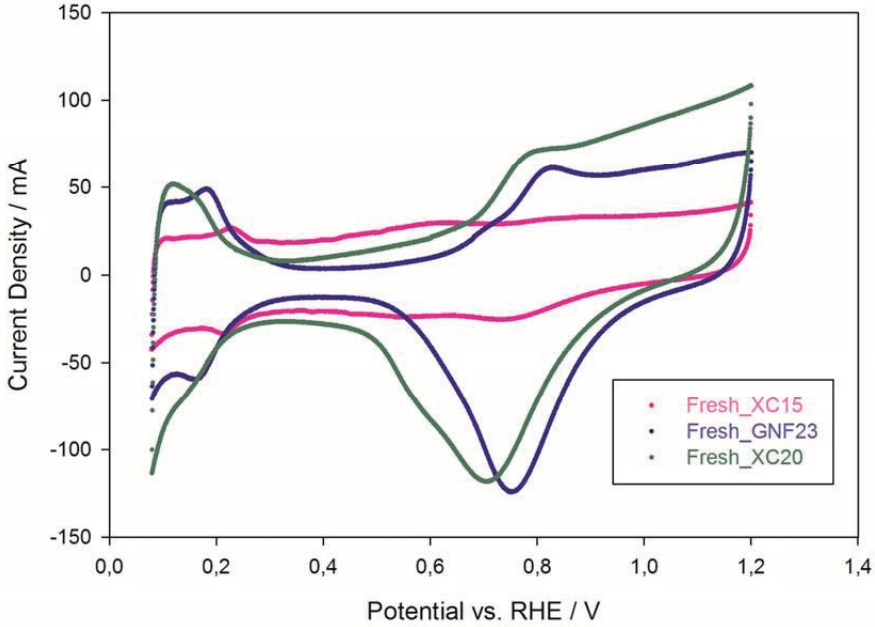

FIGURE 5-9: In-situ cyclic voltammograms for all samples in Figure 5-1. Conditions: the same as Figure 5-8.

The CVs in Figure 5-10 clearly show decreased H_2 adsorption/desorption for XC20 after the degradation signifying an obvious reduction in Pt active surface area. The peaks centered at a potential just below 0.6 V can be assigned to the quinone/hydroquinone couple associated with the carbon surface itself.

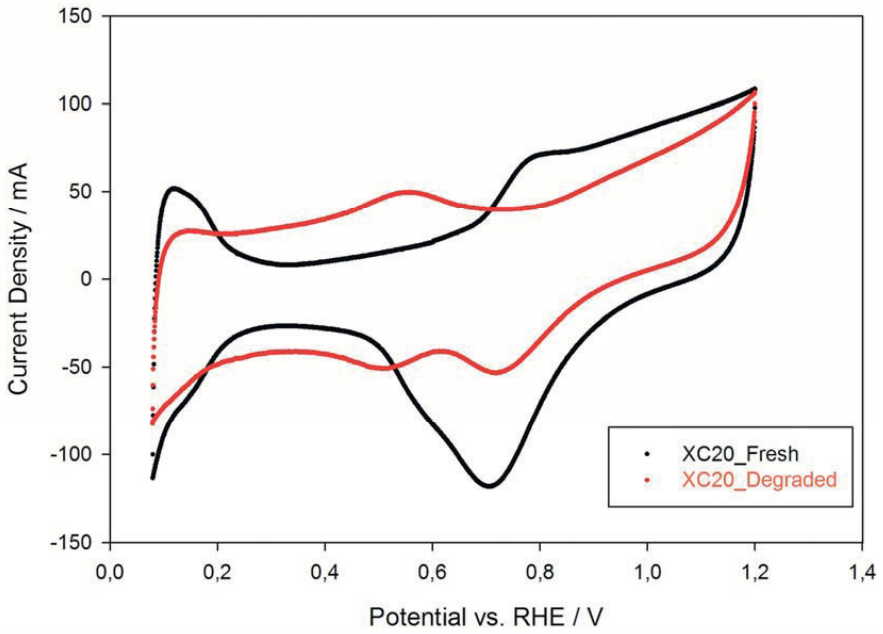

FIGURE 5-10: In-situ cyclic voltammograms for the sample XC20 before and after the ADT. Conditions: the same as Figure 5-8.

There is also a significant increase in the current of double layer area corresponding to the support. This is a clear sign for substantial carbon corrosion in sample XC20 during the degradation protocol.

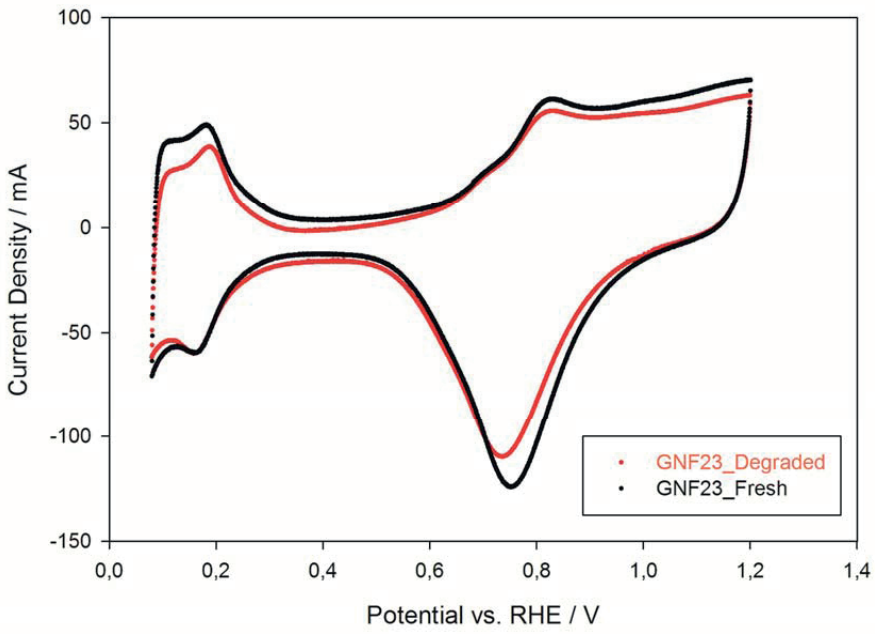

FIGURE 5-11: In-situ cyclic voltammograms the sample GNF23 before and after the ADT. Conditions: the same as Figure 5-8.

Figure 5-11 shows the in-situ cyclic voltammetry results for the sample GNF23 before and after the ADT. The slight decrease in the hydrogen desorption area upon ADT can indicate a minor change in electrochemical surface area for the Pt particles. An interesting observation here is a very slight shrinkage in the double layer region which is completely different from the trend seen in XC20 (Figure 5-10). This may indicate that the carbon support in GNF23 was almost intact upon the ADT while the carbon support in XC20 exhibited clear signs of severe corrosion.

Figure 5-12 shows the results for in-situ CV experiment on XC15, before and after the degradation. A quite small modification after the degradation can be observed in hydrogen adsorption/desorption area as might correlating with the minor decrease in the fuel cell performance seen in the polarization curves in Figure 5-5. On the other hand the change in the double layer current is insignificant analogous to GNF23. This is also an indication that the support material is highly capable to stand the current ADT.

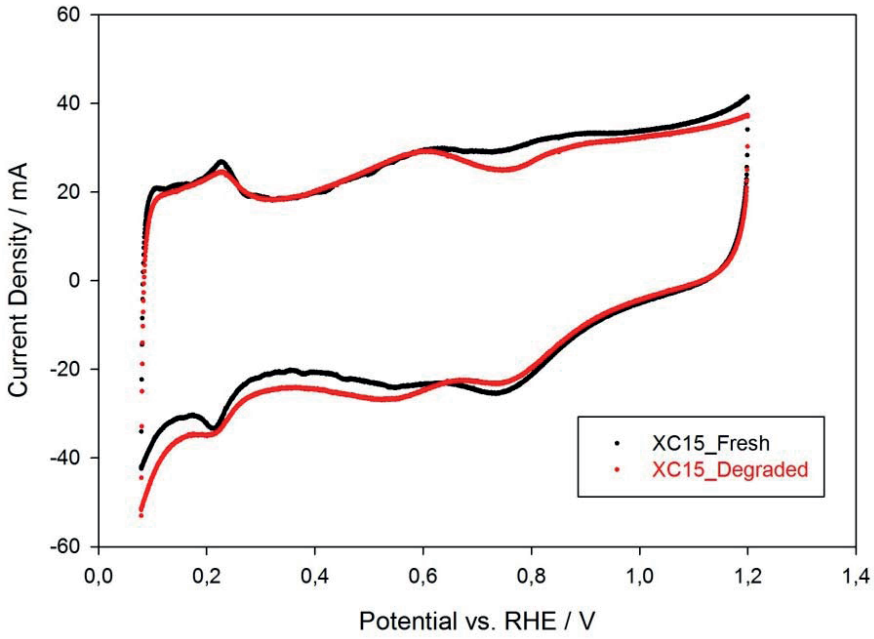

FIGURE 5-12: In-situ cyclic voltammograms for the sample XC15 before and after the ADT. Conditions: the same as Figure 5-8.

The current wide-range potential cycling might potentially cause both Pt degradation and carbon corrosion, given that the incoming gases are similar to polarization curve experiments [75][198][199]. In this work, however, the incoming gases were N_2 and harmix on WE and CE/RE electrodes respectively as explained in Experimental. This was an attempt to ideally isolated different degradation mechanisms. The protocol proved to be determinant for Pt degradation with the observation of the effect of ADT on Pt-black sample and it was also effective in both Pt degradation and carbon corrosion for XC20. On the other hand, the impact of ADT on XC15 (aggregated Pt particles) and GNF23 (film-coat Pt particles) was insignificant and particularly the carbon support in these samples remained unharmed, implying that the current ADT can be used in isolating Pt degradation mechanism for Pt/C catalysts that do not include only individual Pt particles, i.e. samples with a mixture of aggregated and isolated Pt particles on carbon black or samples with nanofibers as the support.

5.4 **Conclusion**

Three classes of carbon-supported Pt samples, containing individual Pt particles only (XC20), a mixture of isolated and aggregated particles (XC15) and inter-networked Pt

particles as a film (GNF23), were investigated structurally and electrochemically. The electrochemical characteristics are clearly different for the three classes of catalysts.

XC20 and XC15 showed the highest and the poorest activity, respectively. Agglomeration thus clearly lowers catalytic activity. The sample Pt supported on GNF (GNF23) had the activity in intermediate to the two samples supported on carbon black. The initial electrochemical characteristics of the Pt film-coat structure over the carbon nanofiber, both in-situ and ex-situ, is similar to that of Pt black (unsupported), but the durability for supported sample (GNF23) is much improved comparing to unsupported Pt.

The sample with aggregated Pt displayed the slowest degradation followed by GNF23. The XC20 had the poorest durability among the tested electrocatalysts. This indicates that the presence of aggregates could improve the durability of the electrocatalysts, however at the cost of electrocatalytic activity.

The ADT used in this work only affected the sample with isolated Pt particles and not the samples with other types of Pt dispersion.

5.5 Acknowledgments

The authors are grateful to Dr. Virginia Ruiz from Aalto University for proving the Pt/GNF samples. The financial support of the work by the Norwegian Research Council and the Department of Materials Science and Engineering, NTNU is acknowledged.

Chapter 6

Pt Dispersion and CO Poisoning

In this chapter the fuel cell performance in presence of CO for the catalysts containing aggregated and only isolated Pt particles are presented. Electrocatalysts with only isolated particles showed higher initial fuel cell performance than the aggregated particles containing electrocatalysts as expected. The degree to which the cell recovers after having been exposed to CO or recoverability of the fuel cell performance for aggregates containing samples appeared to be higher than the electrocatalysts with only isolated Pt particles. The chapter is a manuscript intended for publication.

6.1 Introduction

The practical importance of CO poisoning and CO tolerance of electrocatalysts for PEM fuel cells and the required understanding of the means to handle the hydrogen feedstock for mobile and stationary applications keep the CO-dependent performance of fuel cell central in the electrochemical community [200][201][202].

The research on the effect of the presence and concentration of CO in fuel cell performance has been around for more than a decade [203] and it has been shown that even small traces of CO can significantly affect the hydrogen oxidation reaction on anode

and dramatically reduce the fuel cell performance [204][205]. There is still a tendency in PEM fuel cell research to monitor and enhance the fuel cell performance in presence of CO on the gas fuels as it remains one of the obstacles to mass-commercialization of PEM fuel cells [206][207].

In order to tackle the problem of CO poisoning for the Pt based electrocatalysts, there are studies conducted to implement alloys of Pt with other metals and also innovations for novel electrocatalyst structures [208][209] which basically showed to be promising in terms of CO tolerance enhancement of the [210] but the reproducibility and efficiency of the metal combination for the electrocatalysts can still be improved.

With all these efforts, pure Pt catalysts are still very attractive for PEM fuel cell applications due to the high reactivity they present and the research works are more oriented to increase the platinum utilization as well as electrocatalyst's CO tolerance [211].

A general understanding of mechanism for the CO poisoning of a platinum alloy electrocatalyst and its dependence on the catalyst structure have been already established [212][213][214]. However, it is worth paying closer attention to the nanostructure of the carbon supported Pt catalysts and investigating the link between Pt particles dispersion and the CO poisoning reaction.

In this work it is aimed to study CO-dependent fuel cell performance and to evaluate CO tolerance of Pt/C catalyst with samples containing aggregated and isolated Pt particles on carbon support.

It will be shown that the Pt particle dispersion can have an effect both on the CO resistance and reversibility of CO stripping from the electrocatalysts.

6.2 Experimental

6.2.1 Synthesis

The polyol synthesis technique was employed as explained in details in previous works [106][105]. We synthesized samples consisting of mixtures of isolated and aggregated Pt particles (15 wt% platinum on carbon black Vulcan XC-72) with simultaneous mixing of precursor and support materials and to produce agglomerate-free samples using adsorption polyol method (20 wt% platinum on carbon black Vulcan XC-72). In this work the catalyst with only isolated Pt particles and the one with both individual particles and aggregation are named XC20 and XC15 respectively.

6.2.2 Physical and ex-situ electrochemical characterization

To assess the metal loading, Pt particle size and dispersion and also the structure of the electrocatalysts a set of TGA, TEM and CO stripping voltammetry have been performed as explained in details in the previous works [66][106].

6.2.3 MEA fabrication and fuel cell testing

The catalyst ink consisted of the electrocatalysts together with the ionomer and isopropanol. Evenly airbrush-sprayed ink on the membrane together with the gas diffusion electrode was hot-pressed for 60 seconds at 130 °C and 1000 psi.

Commercial gas diffusion media (SIGRACET® gas diffusion media, Type GDL 10 BC), Nafion® membrane PFSA NRE-211 and ETEK Pt/C commercial catalysts as the supplementary electrode were also used in the process of manufacturing the MEAs. The Pt loading on the MEAs were in both case 0.4 $mgcm^{-2}$.

A PEM single cell, with an active area of 5 cm^2, was assembled from the MEAs with Teflon gaskets and flow fields on both sides of the MEA. The cell was uniformly tightened using eight stainless steel screws. A standard breaking (activation) procedure to activate the MEAs was always carried out before starting the fuel cell tests.

An Agilent N3300A apparatus was utilized to record the voltage-current curves and the voltage-time data for CO tolerance test. For the polarization curves the anode was supplied by a stoichiometric gas flow of hydrogen (99.999% purity) and the cathode with oxygen (99.5% purity) with the minimum flow rate of 0.1 $l_n min^{-1}$ and 0.2 $l_n min^{-1}$ respectively. The gases were humidified in separate bottles with 90% RH. The cell was operated at 80 °C.

In the CO tolerance test, the cell was kept at a constant current density with pure oxygen on cathode and pure hydrogen on anode. Then the pure hydrogen stream was replaced by a 100 ppm CO in hydrogen as the gas fuel for 15 minutes followed by replacing the H_2/CO stream by pure hydrogen again. The cell voltage was recorded versus time in the whole CO tolerance measurement experiment.

6.3 Results and discussion

In the previous work [106] the structural features of the sample XC15 and XC20 have been closely studied using physical characterization techniques and cross-checked by electrochemical methods. XC15 is a sample with a mixture of individual Pt particles on the support while XC20 contains only isolated Pt particles dispersed on carbon support as schematically shown in Figure 6-1.

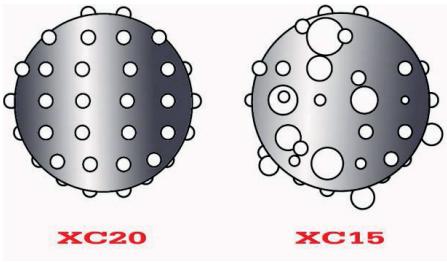

FIGURE 6-1: Schematic representation of the samples XC20 and XC15 with regards to the Pt particle dispersion

Both samples were used to make the ink, MEAs and assembled in a fuel cell hardware as explained in the experimental section and underwent the same activation and characterization protocols.

The CO-dependent polarization curves for both electrocatalysts are shown in Figure 6-2. Except for the very beginning of the polarization curves, for every given potential the fuel cell equipped with XC20 produces higher current density than the one assembled with XC15 electrocatalyst. This indicates that the fuel cell performance of XC20 is higher than XC15 implying that the isolated Pt particles were more efficiently used as electrochemical active sites for the fuel cell reactions in line with previous studies [32][105].

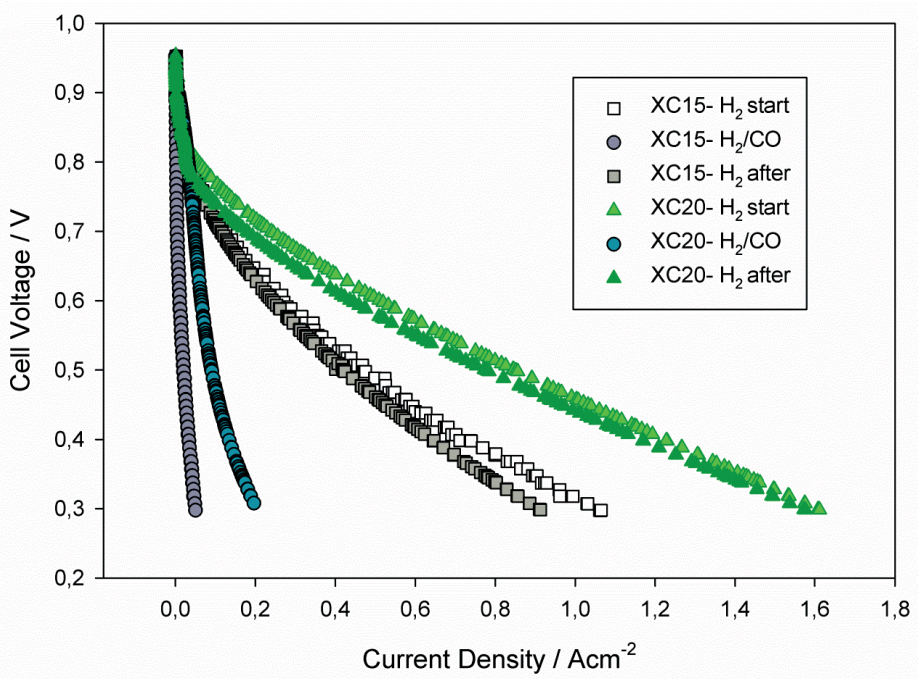

FIGURE 6-2: voltage-current curves for XC15 and XC20. The cathode side was fed by pure oxygen and the anode side was fed first by pure hydrogen (H_2-start), then 100 ppm CO in hydrogen (H_2/CO) and eventually pure hydrogen again (H_2-after).

As one would expect the fuel cell performance in initial measurement on the fresh samples is slightly higher than that of the secondary experiment after the 15-minute CO poisoning time in both cases.

Table 6-1 shows the current densities at 0.6 V extracted from the polarization curves for the three conditions (H_2-start, H_2/CO and H_2-after) with the decrease of current density comparing to the fresh sample in percentage. The decrease of current density from the values in H_2-start to H_2/CO can be considered as a measure of CO resistance for the certain sample while the decrease in current density values from H_2-start to H_2-after can be a measure of reversibility of the electrode in terms of gaining back the same activity as fresh sample after switching to pure hydrogen again. Overall CO tolerance of the electrocatalysts can be then concluded based on the two types of current density decrease.

TABLE 6-1: Current density at 0.6 V for the sample XC15 and XC20 extracted from the polarization curves in Figure 6-2 and percentage decrease in current density comparing to the fresh sample.

	Current density at 0.6 V (Acm^{-2})				
Sample	**H_2-start**	**H_2-after**	**Decrease (Reversibility)**	**H_2-CO**	**Decrease (Resistance)**
XC15	0.2656	0.2413	9 %	0.0106	96 %
XC20	0.5091	0.436	14 %	0.0645	87 %

Comparing the values presented in Table 6-1, XC20 appears to have higher CO resistance while the reversibility of the current density for the electrodes is more promising for XC15.

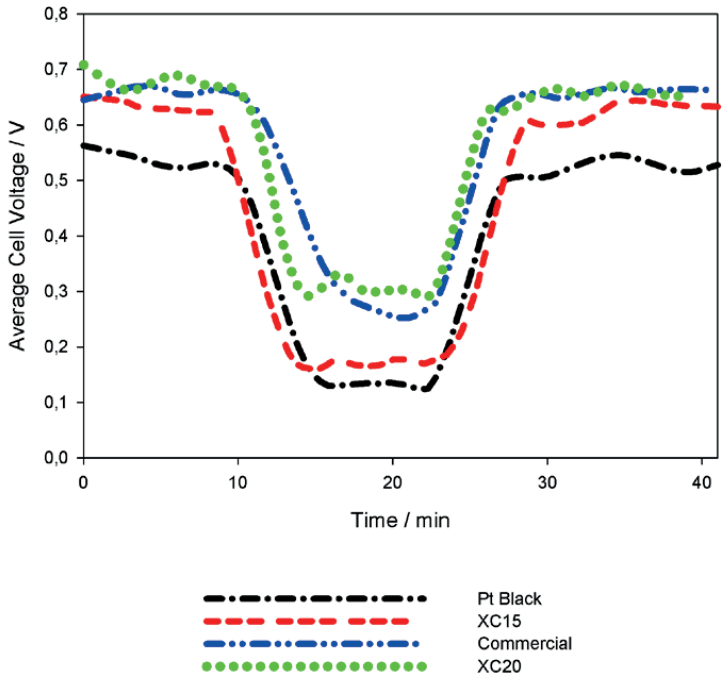

FIGURE 6-3: Average cell voltage versus time plot in pure hydrogen (T<10 min), H_2/100 ppm CO (10 min<T<25 min) and pure hydrogen again (T>25 min). The data has been recorded at 0.4 Acm^{-2}.

In a separate experiment the XC15 and XC20 samples were tested in a simple CO tolerance protocol where at a constant current density, the average cell voltages were recorded versus time with the same condition as outlined in Figure 6-2. Together with

the electrocatalysts samples, a Pt black (unsupported) and a commercial Pt/C catalyst (JM) were also tested here as benchmarks.

As soon as the CO is introduced to the cell, the cell voltage experiences a dramatic fall in all cases until it reaches a steady-state voltage and stabilizes there for the rest of the poisoning time. With almost the same slope, the cell voltages get back towards the values for fresh samples after replacing the gas fuel with pure hydrogen again.

TABLE 6-2: Average cell voltage (V) at 0.4 Acm^{-2} before and after CO poisoning for the four samples. Data extracted from Figure 6-3

	Average cell voltage (V)		
Sample	**H_2-start**	**H_2-after**	**Reversibility**
Pt Black	0.53	0.52	98%
XC15	0.62	0.62	100%
XC20	0.67	0.64	96%
Commercial	0.66	0.65	98%

From Figure 6-3 a lower initial cell voltage and a lower steady-state potential under CO poisoning can be seen from XC15 comparing to XC20. This would be attributed to the higher Pt particle dispersion of XC20 and the more Pt utilization of this sample towards fuel cell reactions as described in the previous section. The lower steady-state cell voltage for XC15 is also a measure of lower CO resistance and is in the same trend as what has been seen in Table 6-1. In this table the recoverability for the average cell voltage after the CO poisoning for XC15 is also slightly higher than XC20 in a similar trend of the measure of reversibility in Figure 6-2.

The bonding of CO molecules on Pt atoms for PEM fuel cell electrocatalysts can be linear and bridge-bonded with different bonding energy and strength [109][110]. For the XC20 sample where Pt nanoparticles are well dispersed on carbon support, the strongest CO adsorption mechanism in linear configuration, meaning one CO molecule per Pt atom ($Pt\text{-}CO_{ads}$), is likely to occur. However for XC15 where the sample contains aggregated Pt particles and alternative defect sites, the possibility to have bridge-bonded CO on Pt atoms in addition to linear configuration increases. This means that the XC15 sample is more affected in terms of fuel cell performance while poisoned with 100 ppm carbon monoxide in anode feed.

But when the mixture of H_2-CO is replaced by pure hydrogen again, the CO-Pt atom linear bonds on Pt atoms in the XC20 sample are more difficult to break than those of bridge-bonded on Pt atoms in the XC15 sample according to the well-established studies on the different energies corresponding to alternative CO-Pt atom bonds [215].

6.4 Conclusion

Samples with only individual Pt nanoparticles on carbon support (XC20) and a mixture of isolated and aggregated Pt nanoparticles (XC15) were utilized to fabricate MEAs and used in a PEM fuel cell hardware. The polarization curves have been drawn under pure H_2, H_2/100 ppm CO and pure H_2 again. Also average cell voltage was recorded versus time in the three mentioned conditions at a constant current density.
The results exhibit that the XC20 have higher initial fuel cell performance than XC15. This might be due to the more available Pt reactive sites as a consequence of a better Pt nanoparticle dispersion over the support.

The resistance of the XC20 electrocatalysts against CO poisoning was also slightly higher than XC15. This was attributed to the possibility of both linear and bridge bonding for CO molecules to the Pt atoms in XC15 with a lot of Pt agglomeration and individual Pt particles comparing to the only linear configuration possibility for XC20 as a well-dispersed Pt nanoparticle electrocatalyst with only individual Pt nanoparticles.

The reversibility of the fuel cell performance was slightly higher for XC15 comparing to XC20. This is thought to be linked to the stronger linear CO bonds on Pt atoms in XC20 and the higher chance for weak bridge-bonded CO molecules in XC15 to strip off due to the change of the gas fuel to pure hydrogen on the anode.

6.5 Acknowledgement

The financial support of the work by the Research Council of Norway and the Department of Materials Science and Engineering, NTNU, is acknowledged.

Chapter 7

Aggregated Particles Subjected to Cycling: dEIS Study

In this chapter a PEM fuel cell membrane electrode assembly (MEA) was characterized by dynamic electrochemical impedance spectroscopy (dEIS) before and after potential cycling in a single cell configuration. The results show that dEIS is a sensitive technique to detect even very moderate changes in electrocatalyst structure. The chapter is based on a paper published in Journal of Power Sources 242 (2013) 447-454.

7.1 Introduction

Although Proton exchange membrane fuel cells (PEMFCs) have come a long way to be an efficient source of power, there are still shortcomings to be addressed. This includes stability issues, for which there are stringent technical requirements to fulfil [216][217][145][218]. It is therefore important to quantify and understand activation and degradation of PEMFC components. In particular there is a need for an understanding and early-fault detection of degradation of electrode catalysts. The cathode appears especially prone to degradation due to its excursion to high potentials and repeated forming and removal of Pt oxide layers. Due to catalyst restructuring, place-exchange

during this process [219] and subsequent loss of catalyst coordination, the cathode is therefore one of the major sources of performance loss in PEM fuel cells. On the other hand the oxygen reduction reaction at the cathode is highly sensitive to the electrode structure [68][130]. Therefore surface restructuring due to degradation will be subject to mechanism changes and possibly also activity changes. To understand these possible changes and in particular to detect them at an early stage, development of associated sensitive characterization and diagnosis techniques such as those suggested by others [165][190][198][220] are required.

Electrochemical impedance spectroscopy (EIS) is a robust diagnosis tool for studying fuel cells and fuel cell reactions, including those relevant for PEM fuel cells [112][113]. The simplest use of EIS is for estimation of the ohmic and charge transfer resistances [114][115][116][117], for which the technique is now routinely used. More sophisticated analysis of EIS data offers in addition information complementary to that obtained from polarization curves and cyclic voltammetry alone, such as information pertaining to electrode structure and electrode reaction mechanisms. As such EIS offers a resolution not available in polarization curves since the different processes that contribute to the acquired data can be separated in frequency [112][118] .

There are a few examples showing that the shape of the impedance spectrum alone can give clear indications of a certain reaction mechanism out of the subset of mechanisms possible under the prevailing reaction conditions [221][222]. A prominent example of the use of EIS in diagnosis of electrochemical systems in terms of reaction mechanism is the study of processes involving multi-step reactions with adsorbed intermediates [222][223]. Thus, a low-frequency inductive loop that appears in the impedance spectra of point contacts of Pt and Ni at YSZ in CO and CO_2 is only consistent with at least two adsorbed intermediates taking part in the reaction [177][224]. Another relevant example is the study performed by Müller and co-workers on a direct methanol fuel cell anode [225][226]. They showed that an inductive loop appears under pure kinetic control, while two capacitive loops are present when introducing significant mass-transfer limitations [225].

Usually, EIS is performed under steady-state conditions. In dynamic impedance spectroscopy (dEIS) [15], on the other hand, EIS spectra can be collected also for systems under dynamic conditions. Thus, a multi-sine wave consisting of all frequencies of interest is superimposed on a dc potential ramp. This provides the possibility to collect kinetic information on transient surfaces, which is not available in electrochemical impedance spectroscopy under steady-state conditions. This may be important for example if one wants to detect the presence of (short-lived) adsorbed intermediates in electrochemical reactions. Also polarization curves can be extracted from the measurements simultaneously with the impedance spectra. This enables direct correlation between the impedance spectra and features in the fuel cell performance in this case. Since all frequencies are applied simultaneously in the dEIS technique, a fast Fourier transform

(FFT) algorithm is used to separate each frequency's current response. dEIS is also different from ac voltammetry, since in the latter technique impedance spectra are collected one frequency per potential scan. As a consequence there will be a time lapse between the first and the last measured frequency which may be the source for some drift effects. Such time effects are eliminated with the dEIS technique.

There is also solid evidence of the feasibility for studying the activation and degradation processes on electrodes and membranes in fuel cells by EIS [227][228]. Although EIS has been applied to some extent for studying the aging of electrodes by EIS at constant current or potential [229][230][231][232], less attention has been paid to impedance spectroscopy at electrocatalysts undergoing potential cycling. Also, ex-situ measurements [112][227] appear to dominate over in-situ techniques [15][233]. To the best of our knowledge there is but very limited data dealing with establishment of a link between overall electrocatalyst activation and degradation and its impedance spectra evolution in-situ. As far as the application of EIS in PEM fuel cell diagnostics are concerned there appears to be at least two possibilities for improvement: i) applications of EIS with comprehensive studies on MEAs in-situ, and ii) investigations on degradation phenomena using a potential cycling protocol, which is different than an aging protocol at a constant current density or potential. A combined perspective is to have an in-situ detectable EIS response to the changes in reaction mechanism occurring as a consequence of a wide-range potential cycling degradation.

In the present study we pursue the mitigation of these two shortcomings by presenting an approach to study the properties of a cycled MEA based on dynamic electrochemical impedance spectroscopy. The appearance of a resolved semicircle and an inductive loop for the pristine sample and an additional partially developed semicircle for the cycled MEA will be discussed in the light of a plausible mechanism change under the cycling protocol.

7.2 **Experimental**

The experimental part in this work includes the synthesis of the Pt/C electrocatalyst and corresponding physical and structural characterization and microscopy and ex-situ electrochemical characterization in the first step and then fabrication of MEAs and relevant in-situ electrochemical measurements in the second step. The following provides a detailed explanation of each sub-step.

7.2.1 Synthesis of electrocatalyst

The polyol technique was used to synthesize the electrocatalysts as described in detail elsewhere [105]. In brief, the support material (carbon black) was dispersed in ethylene glycol (EG) and kept at 50 °C for 30 minutes. Platinic acid, already dissolved in ethylene glycol, was added to the mixture and the temperature was increased to 110 °C under a nitrogen flow. The mixture was kept at elevated temperature for 1.5 hours followed by cooling step in the air and centrifuging the catalyst, ultrasonic homogenization, and washing with water and acetone. The sample was dried at 800 °C for 8 hours.

The sample used in this study comprised 15 wt% platinum on Vulcan XC-72 carbon support and accordingly marked as XC15. The actual metal loading was estimated from the residue of the TGA experiment in oxygen atmosphere from room temperature to 800 °C with a heating rate of 10 °C min^{-1} using an NETZCH system model STA 449C.

7.2.2 Transmission electron microscopy

A JEOL JEM-2010 transmission electron microscope was used to estimate the particle size and assess the metal distribution on the support both before and after the cycling. TEM was performed on the pristine sample as synthesized and on the extracted catalyst from the MEA, which was carefully scraped away from the cathode side of the cycled MEA.

7.2.3 Electrochemical studies in liquid cell

The electrochemical measurements were carried out in a 0.5 M $HClO_4$ solution in a conventional three-electrode cell at room temperature. Ar was bubbled for 30 minutes prior to the experiment to remove any dissolved oxygen from the electrolyte. The electrolyte was kept under an Ar blanket during the course of the experiment.

A reversible hydrogen electrode (RHE) was used as reference electrode and a 1.5 cm^2 plate of pure platinum as counter electrode. An electrocatalyst ink was prepared by sonication of 1.0 mg of the catalyst in 1.0 mL of water. Then 20.0 µL of the ink was pipetted on a disk-type glassy carbon (GC) and dried in N_2, followed by addition of 20 µL Nafion® to cover the working electrode. The area of the GC electrode was 0.196 cm^2. The CVs and CO stripping experiments were performed with an Autolab potentiostat model PGSTAT302N along with a three-electrode cell equipped with necessary connections for Ar and CO. The CO electrooxidation protocol applied in this study was to run cyclic voltammetry (CVs) 20 times at the rate of 100 mVs^{-1} followed by 5 CVs at 10 mVs^{-1}. CO was admitted to the electrode at a potential of 20 mV vs. RHE [209].

Dissolved CO was removed from the cell by an argon purge. In these experiments the CO electrooxidation normally occurred at 10 mVs^{-1}. The experiment was finalized by performing four CVs at 10 mVs^{-1}.

7.2.4 Membrane electrode assembly

In order to prepare an MEA, a Nafion® 115 membrane (DuPont) was cleaned by boiling, first in 3% aqueous H_2O_2 solution for 1 hours, followed by 1 hour boiling in 0.5 M H2SO4, and eventually boiled in Milli-Q water for 15 minutes. The membrane was finally dried in an oven at 70 °C for 15 minutes. The ink of the catalyst was prepared by mixing the Pt/C electrocatalyst powder with the nominal targeted metal mass loading together with 5 wt% Nafion® solution (DuPont), using Milli-Q (18.2 MΩ) distilled water and isopropanol all in analytical grades, in equal volumetric amounts as solvent.

The ink was homogenized in an ultrasound bath and magnetically stirred for a short period before spraying by airbrush (Badger 360 G) on the membrane. The membrane was located on a hot plate at 90 °C for evaporation of the solvents and a more homogenous coating. The area of the resulting electrode was 5 cm^2 and had the loading of 0.4 $mg_{Pt}cm^{-2}$. A commercial gas diffusion electrode (GDE) from ETEK consisting of 20 wt% Pt/Vulcan XC-72 with 0.5 $mg_{Pt}cm^{-2}$ loading on a gas diffusion layer (GDL) was employed for the anode side while the synthesized catalysts served on the cathode side along with commercial SIGRACET gas diffusion media, GDL 35BC. The catalyst-coated Nafion® was hot pressed with the anode GDE at 130 °C and 1400 kPa for 1 minute and the GDL was then mounted on the cathode side to form the MEA.

7.2.5 Fuel cell configuration and in-situ electrochemical studies

A standard commercial PEM fuel cell hardware was used in this study where the MEA was placed inside the cell. The gas inlets were connected to gas humidifiers to reach 100% RH for the incoming gases while the junctions were well sealed to avoid any condensation and unwanted temperature gradients.

Humidified hydrogen and oxygen (5.0) were fed into the anode and cathode, respectively. With the intention of avoiding issues related to gas cross-over, pure hydrogen was replaced by harmix (5% H_2 balanced with Ar) during the cycling test. Oxygen was also substituted with nitrogen for the voltammetric cycles included in the protocol. The gas flow rate for the anode and cathode inlets was minimum 0.10 ln min^{-1} and 0.22 ln min^{-1} respectively to avoid any gas starvation. The fuel cell characteristics were drawn using an Agilent N3300A system. The cell was operated at 80 °C. To avoid gas condensation in the system, the pipe temperature was set to 82 °C.

In-situ cyclic voltammetry and the cycling protocol were conducted by a Biologic SP-150 potentiostat with a 2A booster. The incoming gases were N_2 on the cathode side and harmix on the anode side. The experiment was carried out at 100% RH and room temperature. In-situ CO stripping was also carried out with the same potentiostat and booster configuration and gas inlet except for a replacement of 100 ppm CO in H_2 with the harmix to facilitate CO adsorption.

The fuel cell was characterized with dynamic electrochemical impedance spectroscopy (dEIS). In this experiment a Keithley KUSB-3116 module was used for generation of the multi-sine wave and data logging, a Princeton Applied Research Model 175 waveform generator was used to create the dc potential scan, and the AC and DC components of the potential wave were summed together with Stanford Research System (SRS) Small Instrumentation Modules (SIM). A Gamry Reference 600 potentiostat in analog mode was used to apply the potential signal to the fuel cell. During the dEIS measurements, the time, ac and dc components of the cell potential, and the total cell current were recorded. After the experiment, a custom-made software invokes an FFT algorithm to calculate the impedance at all potentials scanned over according to Reference [120]. In our experiments 46 frequencies in the range 0.2 Hz – 2.6 kHz were superimposed on a slow (1 mVs^{-1}) DC potential scan. A sketch of the dEIS setup is presented in Figure 7-1.

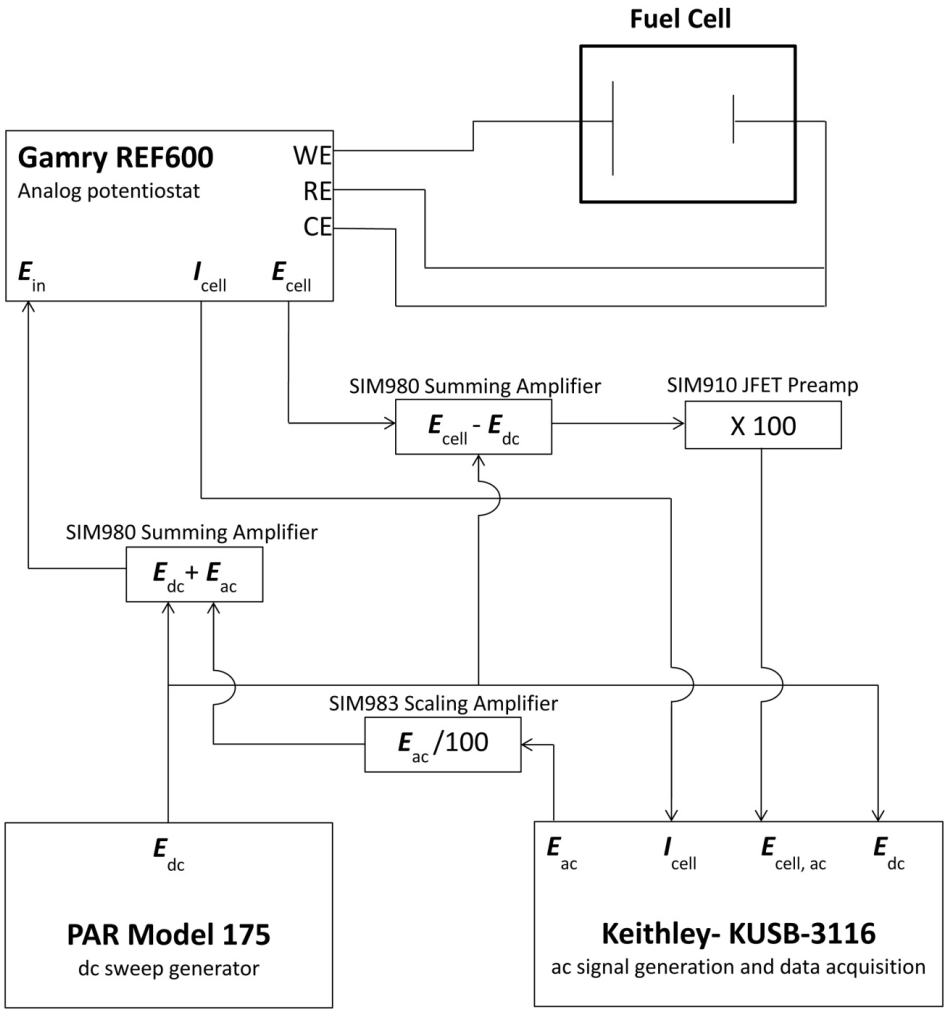

FIGURE 7-1: Sketch of the dEIS setup.

In this study the whole set of in-situ electrochemical measurements were repeated after a cycling protocol of 100 CVs between 0.6 V and 1.5 V vs. RHE in N_2/ 5% H_2 and 80 °C and 100% RH using a sweep rate of 40 mVs^{-1}. O_2 and H_2 flow rates were 24.8 mLs^{-1} and 80 mLs^{-1} respectively.

7.3 Results and discussion

Transmission electron micrographs for pristine XC15 are shown in Figure 7-2 on a range of scales from micron to nanometers. It is apparent that the electrocatalyst consist of both individual and aggregated Pt nanoparticles.

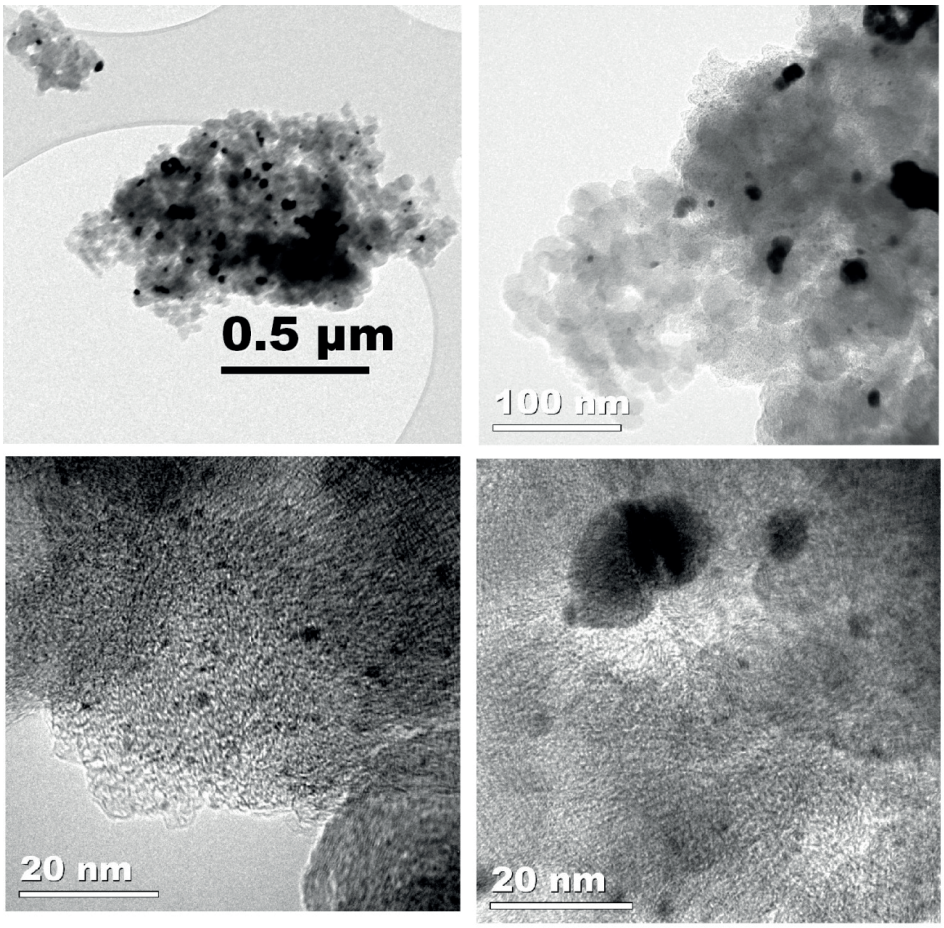

FIGURE 7-2: TEM micrograph from the pristine 15% Pt/XC-72 (XC15) sample powder

Figure 7-3 shows high-resolution TEM images of catalyst scraped away from an MEA surface after it was subjected to the cycling protocol. The images show the same spot of the sample at increasing magnification, the order of which are indicated by the red arrows, in web version. The catalyst particles in the cycled sample in Figure 7-3 appears to be more aggregated than those in the pristine sample, indicating some particle growth during the potential cycling.

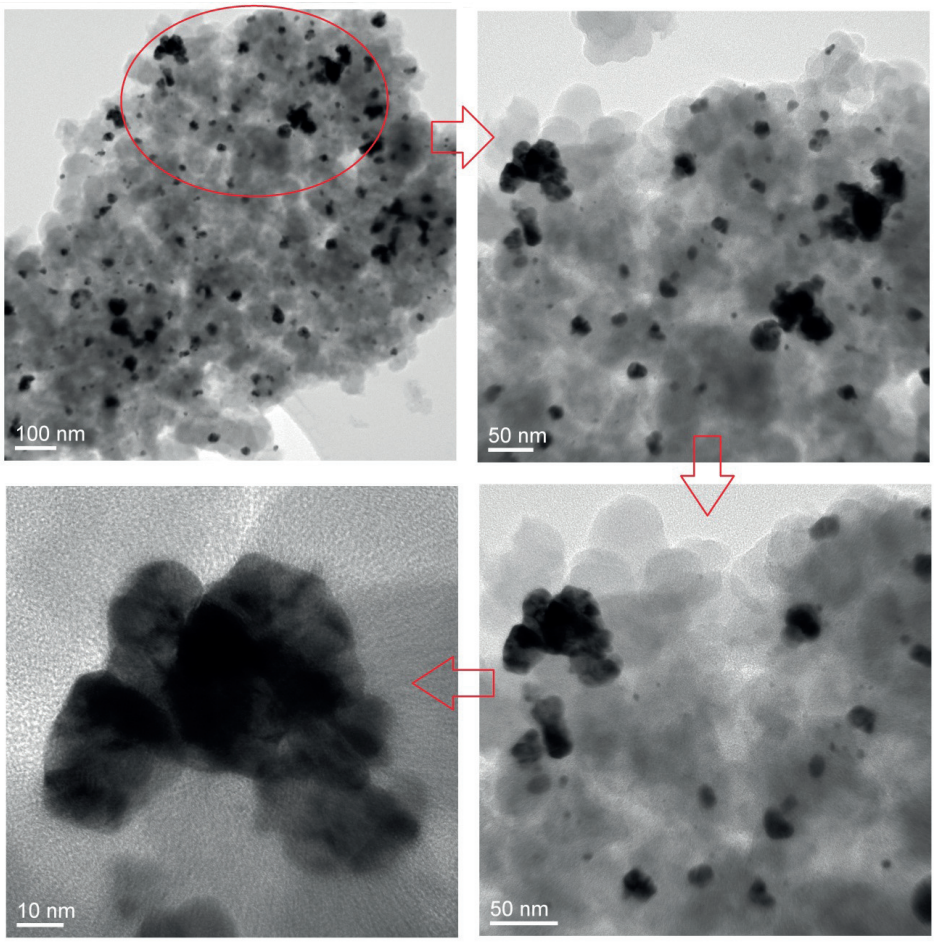

FIGURE 7-3: TEM images of powder scraped away from the cathode surface of the cycled MEA of XC15.

Figure 7-4 shows the collective histograms of platinum particle size from a number of TEM images of pristine and cycled samples. From the histograms there are clear signs of particle growth, and the shape of the distribution for the cycled sample is skewed toward larger diameters relative to that of the pristine samples. The mean particle size for fresh sample is 18.3 ± 0.4 nm while for the MEA of XC15 it is 21.8 ± 0.5 nm.

The particle growth is thus rather moderate. However, quite large particles are present in the fresh sample. These already aggregated Pt particles would not be expected to show a significant tendency for further aggregation. The average increase in diameter may therefore underestimate slightly the actual growth in the most active part of the catalyst,

viz. the smaller particles. In summary, a small but detectable growth in particle size is present as a consequence of the cycling protocol.

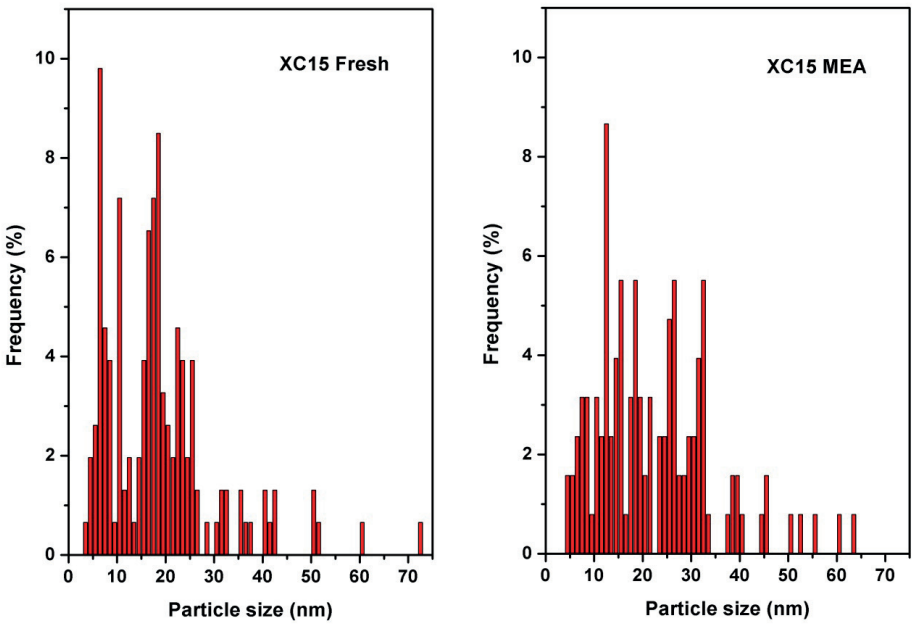

FIGURE 7-4: Histograms of platinum nanoparticles in Figure 7-2 and Figure 7-3 for pristine and cycled samples.

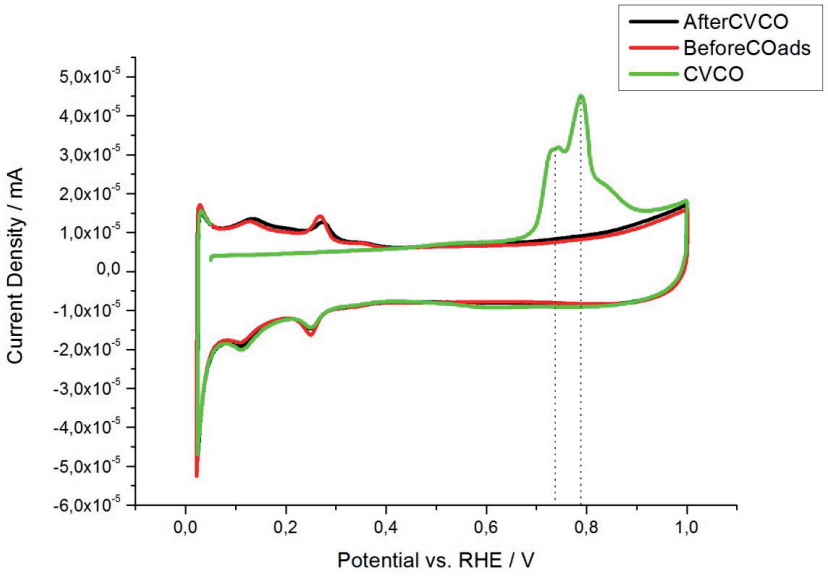

FIGURE 7-5: CO stripping voltammograms at a sweep rate of 10 mVs^{-1} for XC15. The electrolyte was 0.5 M $HClO_4$ and Ar was maintained inside the cell during the experiment at room temperature.

An ex-situ CO stripping voltammogram of the pristine catalyst is shown in Figure 7-5. CO oxidation appears as a double oxidation peak. The larger of these appears at approximately 0.79 V, which is a characteristic value for individual Pt particles. The smaller peak appears at approximately 0.72 V. CO electrooxidation may occur at multiple potentials in samples with aggregated particles [68][69]. In view of the agglomeration apparent in the TEM images in Figure 7-2, we therefore interpret the double peak as being a consequence of particle agglomeration. The peak at 0.72 V may thus corresponds to grain boundaries or other defects associated with the agglomeration.

The electrochemically active surface area (ESA) in the pristine catalyst was estimated to 15.83 m^2g^{-1} based on the charge transferred during the CO electrooxidation assuming CO monolayer bonded with one Pt atom in a linear adsorption configuration (Pt-CO_{ads}), and the equation (7-1) [110]:

$$ESA_{CO}\left(m^2g^{-1}\right) = \left(Q_{CO}\left(C\right) / 420\left(mCcm^{-2}\right)\right).W_{Pt}\left(g\right).100 \qquad (7\text{-}1)$$

where Q_{CO} is the charge transferred related to CO oxidation reaction, 420 $mCcm^{-2}$ is the charge required to oxidize CO monolayer bonded with one Pt atom in a linear adsorption configuration and W is Pt loading.

In-situ CO stripping voltammograms recorded on XC15 before and after the cycling protocol are shown in Figure 7-6. In the fresh sample there is no peak splitting apparent as in the ex-situ stripping voltammogram (Figure 7-5). Apparently, the in-situ CO stripping is less sensitive to agglomeration than ex-situ stripping. We relate this fact to the difference in catalyst mass and the thickness in the two cases. In a porous layer, as in the in-situ experiment, the current and potential are distributed through the layer. Similar changes in the hydrogen-adsorption region are also frequently observed [82][234]. However, in view of the shoulder at 0.76 V in the cycled sample, it does appear possible to also use CO stripping voltammetry in-situ to assess agglomeration in the catalytic layer. In the stripping voltammogram of the cycled sample a small shoulder has developed, again indicating moderate agglomeration as a consequence of the cycling protocol.

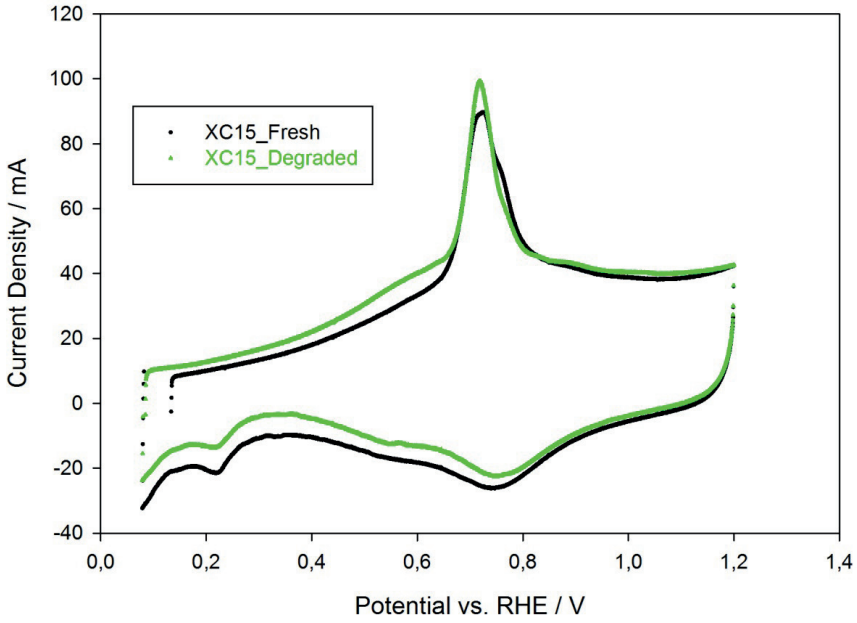

FIGURE 7-6: In-situ CO stripping voltammetry for the sample XC15 before and after the cycling. Gases: N_2/harmix for CVs (100 mVs^{-1}) and CO/harmix for CO adsorption (150 mV vs RHE). The experiment was carried out at 100% RH and room temperature.

The ESA was estimated in the same range as the data extracted from the ex-situ CO stripping voltammetry and showed a loss of around 17% loss. Table 7-1summarizes the mean particle size and ESA for the pristine and cycled electrocatalysts.

TABLE 7-1: Properties of the sample XC15, 15% Pt/XC-72, synthesized by polyol before and after the cycling protocol.

Property↓ Value →	Pristine sample	Cycled sample	Change upon cycling
Mean particle size[3] (nm)	18.3 ± 0.4	21.8 ± 0.5	+17%
ESA[4] ($m^2gr^{-1}_{Pt}$)	15.8	13.2	-16%

In-situ CVs of the fresh and cycled samples shown in Figure 7-7 demonstrate a very slight alteration in the H_2 adsorption/desorption area indicating a minor change in electrochemical surface area for Pt particles as discussed earlier. The CVs in Figure 7-7 comply with the indications in TEM pictures and corresponding histograms of particle size distribution that the Pt particles were only moderately affected by the accelerated cycling.

[3] Obtained from histograms of particle size distribution from TEM images shown in Figure 7-4.
[4] Obtained from ex-situ CVs (for the pristine sample) and in-situ CVs (for the cycled sample)

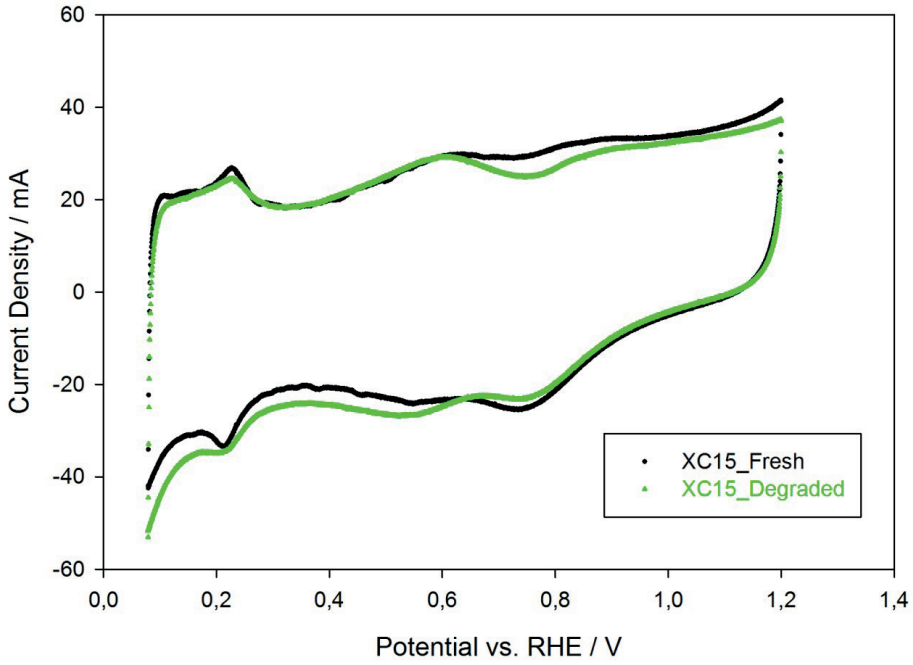

FIGURE 7-7: In-situ anodic cyclic voltammograms for the sample XC15 before and after the cycling. Gases were N_2 on WE and harmix on CE/RE. Sweep rate was 100 mVs^{-1}. The experiment was carried out at 100% RH and room temperature.

Impedance spectra obtained with dEIS measurements at selected cell voltages before and after the cycling procedure are shown in Figure 7-8. At high cell voltages (low overpotentials), the impedance is large and forms an incipient semicircle in the first quadrant. As the voltage decreases, the low-frequency limit of the total impedance decreases as expected since the overpotential increases. The shape then develops into a full semicircle. The radius of the impedance spectra is lower after cycling than for the impedance before cycling, suggesting that the charge-transfer reactions have become faster. A similar behavior was also observed by Hu et al. [232].

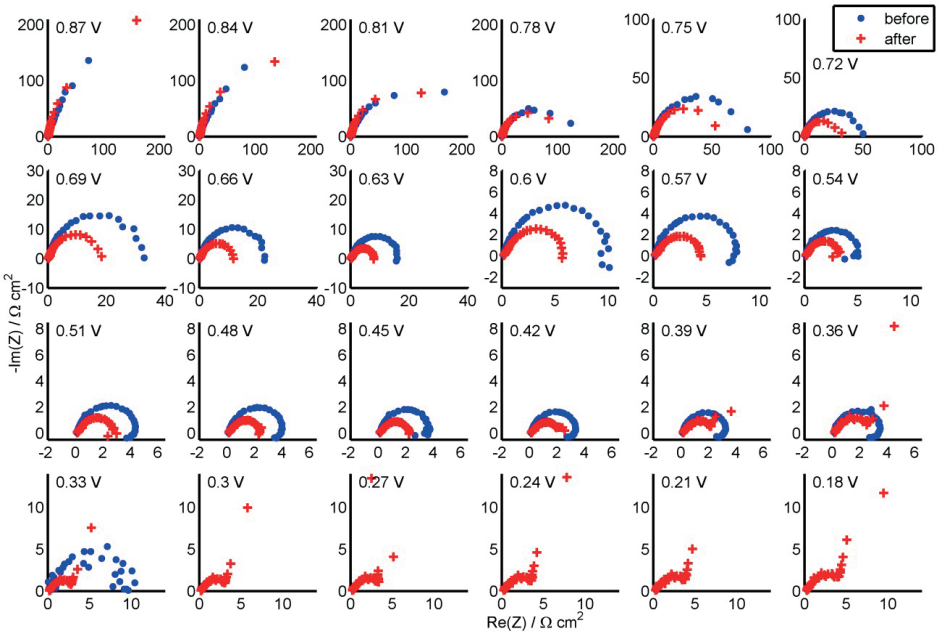

FIGURE 7-8: Impedance spectra at selected cell voltages during the slow potential scan for XC15 MEA before and after the cycling.

At approximately 0.57 V, a loop in the fourth quadrant appears in the low-frequency part of the impedance spectra obtained before cycling (The low frequency part of the spectrum bends back toward the origin of the impedance plan and simultaneously the imaginary part becomes positive.). This inductive loop is often associated with an adsorbed species. After cycling, on the other hand, the inductive loop is not present anymore, except that may be one or two points in the data collected at 0.54 and 0.51 V can be interpreted as an incipient inductive feature of the plot. However, for all the others, all data remain in the first quadrant, and do not curve back toward the origin. Instead, another, first-quadrant semicircle appears below 0.45 V. As the cell voltage is decreased further, this semicircle becomes more visible in the impedance-plane plots.

Quasi-steady-state polarization curves obtained simultaneously as the impedance spectra shown in Figure 7-8 are shown in Figure 7-9. These polarization curves show the effect of the cycling protocol. Between 0.75 V and 0.35 V, the current is slightly higher after the cycling. The limiting current is shifted to lower values after the cycling. (Due to current limitations in the set-up, the polarization curve had to be stopped at approximately 0.3 V before cycling and at approximately 0.2 V after.).

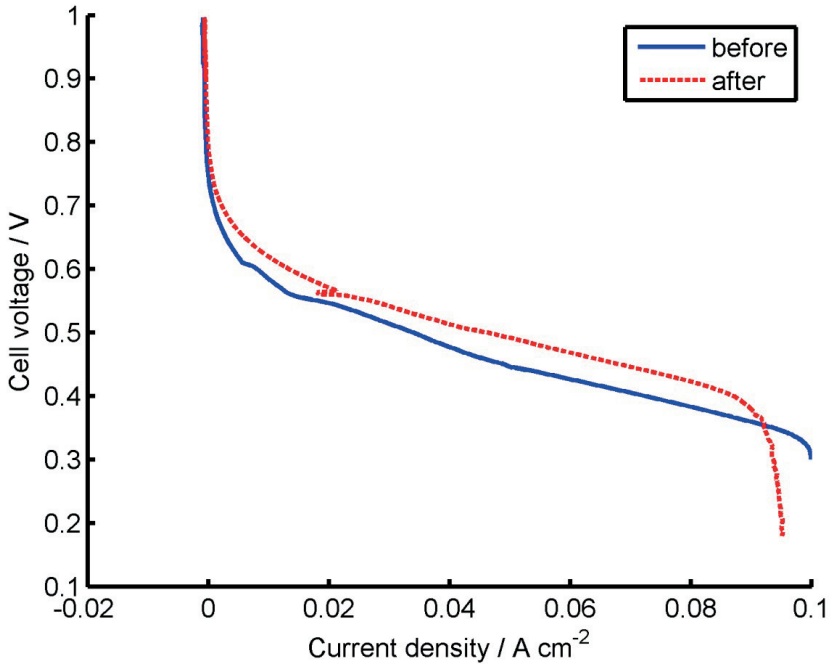

FIGURE 7-9: Polarization curves obtained simultaneously as the impedance spectra when scanning the cell voltage at 1 mVs^{-1}.

Our findings thus indicate that the moderate agglomeration introduced in the samples by the potential cycling leads to an improved activity for CO stripping as reported before and also for the oxygen-reduction reaction (ORR). The latter is in line with the results of Hu et al. [232], who reported impedance spectra showing the effect of time for a fuel cell maintained at constant current for 500 hours. The charge-transfer resistance was found to decrease to a minimum for the first 100 hours, and then increase for the remainder of the experiment. They termed the former phase the activation phase, and the latter phase the degradation phase.

Although the polarization curves in Figure 7-9 only display a limited effect of the cycling procedure, the impedance spectra in Figure 7-8 prove otherwise, since a significant change is seen. This suggests that EIS is a technique that is sensitive enough to study the effects of cycling on fuel cell systems.

The appearance of incipient, second semicircle in the impedance diagrams in Figure 7-8 appears to correlate with the potential at which the limiting current appear in Figure 7-9. When the potential reaches approximately 0.4 V the first few points tracing

out a second feature (semicircle) appear in the in the impedance plane plot (compare impedance plane plots collected at 0.45 V and 0.42 V). It is not easy to define the exact shape of this part of the curve. However, the fact that it appears to bend over rather than rising indefinitely is qualitatively consistent with finite-length diffusion [235], or with simultaneous reaction and diffusion (Gerischer element, see e.g. Reference [177]). We therefore tentatively associate this feature of the spectra with transport limitations in the MEA. However, since no Warburg type sections [236] appear in the plots, a definitive analysis of this feature will not be attempted here.

The inductive loop in the impedance plane plots in Figure 7-8 for the pristine catalyst can in principle also be related to transport phenomena in the electrode, in addition to being related to the electrode kinetics as indicated in the Introduction. Impedance modeling based on flooded agglomerate theory shows that impedance spectra may contain inductive loops purely related to transport in the MEA [178]. However, this only applies if there are two mobile species in the electrolyte, which is not the case here. In the case where one electrolyte species in the model was immobilized, the inductive loop disappeared. In the following we therefore disregard structural changes in the MEA and associated changes in the transport properties as a cause for the changes in the impedance spectra as a result of potential cycling above 0.45 V.

During cycling, the structure of catalyst particles electrodes may change in various ways: Roughening, agglomeration, and dissolution. An explanation for the activation phase while the electrode undergoes a cycling protocol was offered by Nagy, who proposed that surface roughening induced by the oxidation/reduction of Pt atoms would lead to a location exchange with oxygen atoms [219][235]. This is, however, not consistent with the decrease in the EAS observed here, and we disregard the effect of roughening. An increase in particle size is, on the other hand, consistent with the decrease in the ESA, with the increased particle size in the TEM images, and also with the increased activity. Mayrhofer et al. [131] demonstrated a significant increase in the activity for the ORR with increasing particle size, interpreted in terms of changes in the work function with size. Kinoshita [38] has suggested that crystal facets are active for the ORR, whereas corners and edges are not. The reaction thus appears to be only moderately dependent on the concentration of steps in stepped Pt surfaces [237]. Therefore, this also implies that larger particles are more active.

Although the improved performance itself can be explained as due to growing particles, it is difficult to rationalize the initial presence and disappearance of the inductive loop upon cycling any other way than by a change in the reaction mechanism. The inductive loop indicates the involvement of two adsorbed intermediates taking part in the rate-determining step of the reaction. This would be compatible with a large number of reaction mechanisms proposed for the ORR, e.g. involving hydrogen peroxide path for which the rate-determining step is the reaction between two different adsorbates on the Pt surface under acidic conditions [238] (A reaction including the formation of hydrogen

peroxide as an intermediate step in a two-step reaction was recently shown to give inductive loops in impedance plane plots.). It is difficult to explain this with particle growth alone. Lopéz-Cudero et al. [134] recently suggested that the improved activity of agglomerated Pt catalysts is due to the formation of edges at the interface between two different nanoparticles in contact (thus being agglomerated). These edges and an adjacent crystal plane may form a locally concave surface, and are different from edges at single particles which would be convex. This may change the interaction between adsorbates at the edge and those at the adjacent crystal plane. Although the degree to which the ORR in general is structure-sensitive is still open [68], we suggest here that an effect similar to that proposed by Lopéz-Cudero in reference [134] is operative in the ORR and that the changes in the impedance spectra are related to edges between nanoparticles. Also, edges formed in the larger crystal facets of larger particles may give rise to a similar activity increase [68].

Thus, the catalyst may become more active due to either larger particles or due to the formation of steps in the crystal facets or at interfaces between agglomerated particles. Our dynamic impedance data appears to indicate that this activity change is associated with a change in the reaction mechanism.

7.4 Conclusions

The polyol synthesized carbon supported Pt nanoparticles were characterized electrochemically ex-situ (in liquid electrolyte cell) and in-situ (in a single PEMFC) before and after a severe cycling protocol. The slight change in the structure of the electrocatalyst due to the cycling was not easy to detect by the other applied physical and electrochemical techniques than the dEIS method used here.

dEIS proved to be a convenient and time-efficient tool to gather impedance spectra for all cell voltages and to be a strong investigative tool to detect small modifications in electrodes which were not practically detectable by CVs, CO stripping, and TEM. With dEIS we detected that the cycling protocol caused a change in the fuel cell reaction mechanism. These changes are suggested to be due to the formation of particularly active sites at growing crystal facets or at the interface between agglomerated particles.

7.5 Acknowledgment

Per Erik Vullum and Yingda Yu are thanked for the assistance with TEM imaging.

The financial support of the work by the Research Council of Norway and the Department of Materials Science and Engineering, NTNU, is acknowledged.

Chapter 8

Conclusions and Future Work

In this chapter the main findings of the thesis are highlighted with respect to the focus of different chapters. Brief explanations on the pathway to achieve the results are also presented in each case. A list of recommendations for future work is given at the end.

8.1 Concluding remarks

In this thesis, first the synthetic routes to produce electrocatalysts with different Pt nanoparticle dispersion on carbon support were optimized with respect to flexibility to choose the dominant phase in catalyst structure. Samples containing isolated Pt particles were used to examine the CCL thickness effect on fuel cell performance and durability. Isolated, aggregated and film-coat[5] Pt nanoparticles were studied inside PEMFC for i) initial electrochemical performance ii) subjected to ADT and iii) exposed to CO. Finally samples containing aggregated Pt particles were studied by dEIS to detect slight structural modification upon ADT.

[5] Isolated and aggregated Pt nanoparticles were supported on carbon black and film-coat Pt nanoparticles were supported on carbon nanofiber

8.1.1 Synthesis of structure-tailored electrocatalysts

Highlight for Chapter 3: The synthesis technique was optimized to positively affect the structural and thus electrochemical properties of Pt/C.

We used four synthesis techniques to produce electrocatalyst with structural characteristics of interest and tried to correlate the synthesis parameters to the properties of resulting materials.

For the techniques employed we have shown how to precisely control Pt dispersion and aggregation through control of the processing conditions, particularly pH of the synthesis solution at final stage. This has given the freedom to select the dominant dispersion and hence to obtain desired electrochemical characteristics.

8.1.2 Thickness of CCL and fuel cell performance

Highlight for Chapter 4: The thickness of cathode catalyst layer (CCL) plays a role in activity and durability of Pt/C electrodes.

Using Pt/C cathode electrodes with Pt loadings of 10 wt%, 20 wt%, and 30 wt% (containing well-dispersed Pt particles), MEAs were prepared containing the same mass of Pt and thus different amount of carbon and consequently different CCL thickness. The fuel cell performance and durability of the samples were studied before and after an accelerated degradation test (ADT).

The initial electrochemical activity was found to be independent of CCL thickness for the range of electrode thickness in this study.

The activity of all CCLs experiences a significant decrease when subjected to the accelerated degradation protocol, both in pure oxygen and in diluted oxygen and the experiment in pure oxygen shows a reduction in catalytic activity approximately independent of the CCL thickness.

In diluted oxygen, however, the activity was strongly dependent on the CCL thickness (or Pt-to-carbon ratio) and there was a much larger reduction in cell voltage for the sample with 10 wt% Pt loading comparing with the other two samples.

We attributed the large fall in fuel cell performance for 10%Pt(90%C) sample to the local current density. We have shown that local current density for this sample crosses a border between two Tafel regimes upon ADT while the 20% and 30% sample remained in the same Tafel regime also after the degradation.

8.1.3 Pt dispersion and fuel cell performance

Highlight for Chapter 4, Chapter 5, and Chapter 6: Electrocatalysts possess certain Pt dispersion-dependent fuel cell performance, durability and CO-tolerance.

We used three dispersion categories of Pt/C samples, containing isolated Pt particles only (XC20, carbon black support), a mixture of isolated and aggregated particles (XC15, carbon black support) and film-coat Pt nanoparticles (GNF23, nanofiber support) to study the effect of particle dispersion on ex-situ and in-situ electrochemical performance, CO-tolerance and electrocatalyst durability. A set of experiments were performed on the samples prior to undergo ADT (Chapter 5) and CO exposure (Chapter 6).

XC20 and XC15 presented the highest and the poorest activity, respectively and the performance of GNF23 was in between those of the two others. Agglomeration thus obviously decreases catalytic activity.

Pt film-coat structure over the outer surface of carbon nanofiber (GNF23) act electrochemically as Pt black (unsupported), both in-situ and ex-situ. The durability for supported sample (GNF23) is much improved comparing to unsupported Pt.

Aggregated Pt particles (XC15) have slower degradation than film-coat Pt particles. Film-covered carbon nanofibers with Pt particles are also slower in degradation comparing to catalysts containing only isolated Pt particles. The presence of aggregates seems to improve the durability at the cost of catalytic activity.

The ADT used in this work only affected the sample with isolated Pt particles or unsupported Pt and not severely the samples with other types of Pt dispersion.

We also studied the fuel cell performance for fresh XC15 and XC20 in presence of CO. Polarization curves and (in a separate test) average cell voltage versus time at a constant current density, were recorded before-under-after exposure to 100 ppm CO.

In this experiment XC20 also showed higher initial performance than XC15 due to the more available Pt reactive sites. The resistance of the XC20 against CO poisoning was also slightly higher than XC15. This was ascribed to the less possibility of linear and more possibility of bridge bonding for CO molecules to the Pt atoms with high and low bond energy, respectively and that notion that linear CO is more probable for XC20 while bridge-bond is more likely to occur for XC15.

The degree to which the fuel cell performance recovered after being exposed to CO was slightly higher for XC15 than for XC20. This was suggested to be due to better possibilities for weak bridge-bonded CO molecules in XC15 to strip off comparing to high-energy bonded linear CO-Pt in XC20.

8.1.4 dEIS and aggregated particles

Highlight for Chapter 7: dEIS is a convenient tool to detect slight alteration in electrodes that are difficult to detect by other methods.

We used dEIS to collect impedance spectra for all cell voltages before and after an ADT (the same protocol as Chapter 4 and Chapter 6) for a sample with aggregated Pt particles.

Comparing the dEIS results before and after the load cycling, we found a very slight structural modification in the electrocatalyst. This was in practice undetectable by CVs, CO stripping and TEM. The changes of the impedance spectra leaded to the transform of reaction mechanism.

8.2 Recommendations for future work

The durability and CO tolerance of electrocatalyst are very dependent on its dispersion and agglomeration and we still need to have a better customized catalyst structures as well as to understand the degradation mechanisms, mitigations, poisoning and recovery and their links to Pt/C structure better. The following list of investigations may be considered:

- ✓ The techniques reported in this thesis for durability and CO-tolerance protocols were only used for Pt-electrocatalysts and that can be further expanded to a wide range of other active metals with conventional structures, core-shell configuration or nanostructured thin films. Also a wide range of nanocarbons as support materials e.g. fullerenes, carbon nanocages or carbon nanobuds should be used to compare the results with carbon clack, carbon nanofibers and carbon nanotubes.
- ✓ Cost analysis for developing new electrocatalysts should be performed to examine these aspects of different materials and structure in light of the activity and durability.
- ✓ There are indications that the ADT used in Chapter 7 can single out the Pt degradation for non-individual Pt particles, but there are contributions from both Pt particles and carbon support in the overall degradation when samples with only isolated particles were used. The ADT used in Chapter 4 is also a clear combination of different degradation mechanisms independent of the catalysts architecture. Therefore it is recommended to seek for ways to develop better accelerated degradation protocols where the different degradation mechanisms for Pt particles and carbon materials can be ideally isolated.

- ✓ Developing new techniques to investigate the durability of electrocatalysts without the requirement to disrupt the fuel cell operation. It is also interesting to develop in-situ microscopy methods to investigate the structural modification real time.
- ✓ Repeating different ADT and CO-exposure in this thesis with precise analysis on the exhaust products. This may give an assessment to better verify the degradation and poisoning theories. This can be also done for electrocatalysts with different Pt dispersion to check the links suggested between the structure and durability.
- ✓ Precise mathematical modeling is required to formulate the dispersion-dependent behaviors of electrocatalysts in different operational circumstances.
- ✓ CO tolerance tests should be performed for Pt/GNF samples and the results should be compared with aggregated and isolated Pt particles.
- ✓ The experiment on Chapter 4 to study the effect of CCL thickness on fuel cell performance and durability can be expanded more with CCLs of the same thickness, different metal loading and the same carbon content or the same carbon content and actual thickness of CCL and different Pt loading. This way the contribution of active metal, support material and thickness can be deeply studied on the durability and activity of electrocatalysts. The same experiment as Chapter 4 should also be performed on MEAs fabricated of catalysts with Pt dispersion other than individual particles, e.g. film-coat Pt nanoparticles on carbon nanofiber.
- ✓ dEIS as a convenient and robust investigative tool to detect very slight changes in electrode should be used more widely in fuel cell research. In this thesis only an aggregation-containing electrocatalyst subjected to a cycling protocol was studied by this technique, but it can be used for any dispersion and composition of catalysts to investigate probable alterations due to operational conditions.

Bibliography

[1] B. Dudley, BP Energy Outlook 2035, 2014.

[2] B. Dudley, BP Statistical Review of World Energy 2014, 2014.

[3] Norwegian Petroleum Directorate, Petroleum Production on the Norwegian Continental Shelf June 2008, 2008.

[4] Norwegian Petroleum Directorate, Production Figures August 2014, 2014.

[5] B. Dudley, BP Statistical Review of World Energy 2012, 2012.

[6] D. Abbott, Proc. IEEE 98 (2010) 42.

[7] J. Yang, A. Sudik, C. Wolverton, D.J. Siegel, Chem. Soc. Rev. 39 (2010) 656.

[8] A.L. Dicks, PEM Fuel Cells: Applications In: Comprehensive Renewable Energy, Elsevier, Oxford, 2012.

[9] B.G. Pollet, I. Staffell, J.L. Shang, Electrochim. Acta 84 (2012) 235.

[10] B.L. Carrette, K.A. Friedrich, U. Stimming, Fuel Cells 1 (2001) 5.

[11] J. Larminie, A. Dicks, Fuel Cell Systems Explained, 2nd ed., Wiley, New York, 2003.

[12] A.J. Arv, A.E. Bolzan, M.A. Pasqual, Catalysis in Electrochemistry: From Fundamentals to Strategies for Fuel Cell Development, 2011.

[13] R. Balmer, Thermodynamics, Chapter 6, West, St Pau, 1990.

[14] S.G. Kandlikar, Z. Lu, J. Fuel Cell Sci. Technol. 6 (2009) 044001.

[15] Z. Lu, S.G. Kandlikar, C. Rath, M. Grimm, W. Domigan, a. D. White, M. Hardbarger, J.P. Owejan, T. a. Trabold, Int. J. Hydrogen Energy 34 (2009) 3445.

[16] H. Li, Y. Tang, Z. Wang, Z. Shi, S. Wu, D. Song, J. Zhang, K. Fatih, J. Zhang, H. Wang, Z. Liu, R. Abouatallah, A. Mazza, J. Power Sources 178 (2008) 103.

[17] C.-Y. Wang, Chem. Rev. 104 (2004) 4727.

[18] M. Eikerling, J. Electrochem. Soc. 153 (2006) E58.

[19] S. Litster, D. Sinton, N. Djilali, J. Power Sources 154 (2006) 95.

[20] P.K. Sinha, C.-Y. Wang, Chem. Eng. Sci. 63 (2008) 1081.

[21] Z. Chen, D. Higgins, A. Yu, L. Zhang, J. Zhang, Energy Environ. Sci. 4 (2011) 3167.

[22] Y. Bing, H. Liu, L. Zhang, D. Ghosh, J. Zhang, Chem. Soc. Rev. 39 (2010) 2184.

[23] E. Antolini, J. Mater. Sci. 8 (2003) 2995.

[24] L. Zhang, J. Kim, E. Dy, S. Ban, K. Tsay, H. Kawai, Z. Shi, J. Zhang, Electrochim. Acta 108 (2013) 480.

[25] B. Avasarala, P. Haldar, Energy 57 (2013) 545.

[26] S. Li, L. Zhang, J. Kim, M. Pan, Z. Shi, J. Zhang, Electrochim. Acta 55 (2010) 7346.

[27] Z. Yin, T. Hua, J. Wanga, C. Wanga, Z. Liub, J. Guo, Electrochim. Acta 119 (2013) 144.

[28] A. Morozan, M.T. Sougrati, V. Goellner, D. Jones, L. Stievano, F. Jaouen, Electrochim. Acta In Press (2013).

[29] H.A. Gasteige, N.M. Markovic, Science (80-.). 324 (2009) 48.

[30] A. Morozan, B. Jousselme, S. Palacin, Energy Environ. Sci. 4 (2011) 1238.

[31] W. Trongchuankij, K. Pruksathorn, M. Hunsom, Appl. Energy 88 (2011) 974.

[32] E. Yli-Rantala, A. Pasanen, P. Kauranen, V. Ruiz, M. Borghei, E. Kauppinen, A. Oyarce, G. Lindbergh, C. Lagergren, M. Darab, S. Sunde, M. Thomassen, S. Ma-Andersen, E. Skou, Fuel Cells 11 (2011) 715.

[33] Z. Tu, H. Zhang, Z. Luo, J. Liu, Z. Wan, M. Pan, J. Power Sources 222 (2013) 277.

[34] J.-S. Choi, W.S. Chung, H.Y. Ha, T.-H. Lim, I.-H. Oh, S.-A. Hong, H.-I. Lee, J. Power Sources 156 (2006) 466.

[35] J. Wu, X.Z. Yuan, J.J. Martin, H. Wang, J. Zhang, J. Shen, S. Wu, W. Merida, J. Power Sources 184 (2008) 104.

[36] M. Koper, A. Wieckowski, Fuel Cell Catalysis: A Surface Science Approach, John Wiley and Sons, New Jersey, 2009.

[37] X. Li, I.-M. Hsing, Electrochim. Acta 51 (2006) 5250.

[38] K. Kinoshita, J. Electrochem. Soc. 137 (1990) 845.

[39] S. Mukerjee, J. Mcbreen, J. Electroanal. Chem. 448 (1998) 161.

[40] K. Kinoshita, J. Electrochem. Soc. 137 (1990) 845.

[41] Z. Xu, H. Zhang, H. Zhong, Q. Lu, Y. Wang, D. Su, Appl. Catal. B Environ. 111-112 (2012) 264.

[42] R. Narayanan, M. a. El-Sayed, Nano Lett. 4 (2004) 1343.

[43] F.J. Vidal-Iglesias, J. Solla-Gullón, P. Rodríguez, E. Herrero, V. Montiel, J.M. Feliu, a. Aldaz, Electrochem. Commun. 6 (2004) 1080.

[44] S. Zhang, X. Zhang, G. Jiang, H. Zhu, S. Guo, D. Su, G. Lu, S. Sun, J. Am. Chem. Soc. 136 (2014) 7734.

[45] N. Tian, Z.-Y. Zhou, S.-G. Sun, Y. Ding, Z.L. Wang, Science (80-.). 316 (2007) 732.

[46] S.-G. Sun, A.-C. Chen, T.-S. Huang, J.-B. Li, Z.-W. Tian, J. Electroanal. Chem. 340 (1992) 213.

[47] L. Dubau, L. Castanheira, G. Berthomé, F. Maillard, Electrochim. Acta 110 (2013) 273.

[48] O.J. Murphy, G.D. Hitchens, D.J. Manko, J. Power Sources 47 (1994) 353.

[49] Y. Zhu, E. Brosha, P. Zelenay, in:, Prot. Conduct. Membr. Fuel Cells III Proc. Int. Symp., The Electrochemical Society, 2005, pp. 490–505.

[50] Fuel Cell Technologies Program Multi-Year Research, Development and Demonstration Plan, Planned Program Activities for 2011-2020, Updated July 2013, 2013.

[51] H. a. Gasteiger, J.E. Panels, S.G. Yan, J. Power Sources 127 (2004) 162.

[52] E. Auer, a. Freund, J. Pietsch, T. Tacke, Appl. Catal. A Gen. 173 (1998) 259.

[53] F. Rodriguez-reinoso, Carbon N. Y. 36 (1998) 159.

[54] X. Yu, S. Ye, J. Power Sources 172 (2007) 133.

[55] P. Trogadas, T.F. Fuller, P. Strasser, Carbon N. Y. 75 (2014) 5.

[56] S. Sharma, B.G. Pollet, J. Power Sources 208 (2012) 96.

[57] R. Siburian, Int. Res. J. Pure Appl. Chem. 4 (2014) 541.

[58] T.W. Ebbesen, H. Hiura, M.E. Bisher, M.M.J. Treacy, J.L. Shreeve-Keyer, R.C. Haushalter, Adv. Mater. 8 (1996) 155.

[59] Y. Shao, G. Yin, Y. Gao, P. Shi, J. Electrochem. Soc. 153 (2006) A1093.

[60] J. Zhou, X. Zhou, X. Sun, R. Li, M. Murphy, Z. Ding, X. Sun, T.-K. Sham, Chem. Phys. Lett. 437 (2007) 229.

[61] X.X. Wang, Z.H. Tan, M. Zeng, J.N. Wang, Sci. Rep. 4 (2014) 4437.

[62] A. Rodrigues, J.C. Amphlett, R.F. Mann, B. a. Peppley, P.R. Roberge, IECEC-97 Proc. Thirty-Second Intersoc. Energy Convers. Eng. Conf. (Cat. No.97CH6203) (n.d.) 768.

[63] P. Stonehart, J. Lljndqliist, Electrochim. Acta 18 (1973) 907.

[64] J.J. Baschuk, X. Li, Int. J. Energy Res. 25 (2001) 695.

[65] F. Maillard, E.R. Savinova, U. Stimming, J. Electroanal. Chem. 599 (2007) 221.

[66] M. Darab, P.K. Dahlstrøm, M.S. Thomassen, F. Seland, S. Sunde, J. Power Sources 242 (2013) 447.

[67] E.G. Ciapina, S.F. Santos, E.R. Gonzalez, J. Electroanal. Chem. 644 (2010) 132.

[68] M.T.M. Koper, Nanoscale 3 (2011) 2054.

[69] F. Maillard, S. Schreier, M. Hanzlik, E.R. Savinova, S. Weinkauf, U. Stimming, Phys. Chem. Chem. Phys. 7 (2005) 385.

[70] G. a. Camara, E. a. Ticianelli, S. Mukerjee, S.J. Lee, J. McBreen, J. Electrochem. Soc. 149 (2002) A748.

[71] A. Suzuki, T. Hattori, R. Miura, H. Tsuboi, N. Hatakeyama, H. Takaba, M.C. Williams, A. Miyamoto, Int. J. Electrochem. Sci. 5 (2010) 1948.

[72] A. Stassi, I. Gatto, V. Baglio, E. Passalacqua, A.S. Aricò, J. Power Sources 222 (2012) 390.

[73] A. Wieckowski, E.R. Savinova, C.G. Vayenas, Catalysis and Electrocatalysis at Nanoparticle Surfaces, Marcel Dekker Inc., 2003.

[74] M. Koper, W. Andrzej, Fuel Cell Catalysis: A Surface Science Approach, John Wiley and Sons, 2009.

[75] R.L. Borup, J. Meyers, B. Pivovar, Y.S. Kim, R. Mukundan, N. Garland, D. Myers, M. Wilson, F. Garzon, D. Wood, P. Zelenay, K. More, K. Stroh, T. Zawodzinski, J. Boncella, J.E. McGrath, M. Inaba, K. Miyatake, M. Hori, K. Ota, Z. Ogumi, S. Miyata, A. Nishikata, Z. Siroma, Y. Uchimoto, K. Yasuda, K.-I. Kimijima, N. Iwashita, Chem. Rev. 107 (2007) 3904.

[76] A.B. Ofstad, M.S. Thomassen, J.L. Gomez de la Fuente, F. Seland, S. Møller-Holst, S. Sunde, J. Electrochem. Soc. 157 (2010) B621.

[77] M. Watanabe, K. Tsurumi, T. Mizukami, T. Nakamura, P. Stonehart, J. Electrochem. Soc. 141 (1994) 2659.

[78] T. Akita, A. Taniguchi, J. Maekawa, Z. Siroma, K. Tanaka, M. Kohyama, K. Yasuda, J. Power Sources 159 (2006) 461.

[79] Y. Zhai, H. Zhang, D. Xing, Z.-G. Shao, J. Power Sources 164 (2007) 126.

[80] P. Ascarelli, V. Contini, R. Giorgi, J. Appl. Phys. 91 (2002) 4556.

[81] M.S. Wilson, F.H. Garzon, K.E. Sickafus, S. Gottesfeld, J. Electrochem. Soc. 140 (1993) 2872.

[82] R.W. Lindström, K. Kortsdottir, M. Wesselmark, A. Oyarce, C. Lagergren, G. Lindbergh, J. Electrochem. Soc. 157 (2010) B1795.

[83] S.-Y. Ahn, S.-J. Shin, H.Y. Ha, S. -a. Hong, Y.-C. Lee, T.W. Lim, I.-H. Oh, J. Power Sources 106 (2002) 295.

[84] Y. Shao, G. Yin, Y. Gao, J. Power Sources 171 (2007) 558.

[85] S.D. Knights, K.M. Colbow, J. St-Pierre, D.P. Wilkinson, J. Power Sources 127 (2004) 127.

[86] L.M. Roen, C.H. Paik, T.D. Jarvi, Electrochem. Solid-State Lett. 7 (2004) A19.

[87] P.T. Yu, W. Gu, R. Makharia, F.T. Wagner, and H.A. Gasteiger, ECS Trans. 3 (2006) 797.

[88] A. Ofstad, J. Davey, S. Sunde, and R.L. Borup, ECS Trans. 16 (2008) 1301.

[89] A. Taniguchi, T. Akita, K. Yasuda, Y. Miyazaki, J. Power Sources 130 (2004) 42.

[90] X. Cheng, Z. Shi, N. Glass, L. Zhang, J. Zhang, D. Song, Z.-S. Liu, H. Wang, J. Shen, J. Power Sources 165 (2007) 739.

[91] S.T. Briskeby, M. Tsypkin, R. Tunold, S. Sunde, J. Power Sources 251 (2014) 1.

[92] Z. Siroma, K. Ishii, K. Yasuda, Y. Miyazaki, M. Inaba, A. Tasaka, Electrochem. Commun. 7 (2005) 1153.

[93] L. Li, Y. Xing, J. Electrochem. Soc. 153 (2006) A1823.

[94] B.G. Pollet, Int. J. Hydrogen Energy 35 (2010) 11986.

[95] J.H. Liu, M.K. Jeon, S.I. Woo, Appl. Surf. Sci. 252 (2006) 2580.

[96] A. Luengnaruemitchai, S. Osuwan, E. Gulari, Int. J. Hydrogen Energy 29 (2004) 429.

[97] E.S. Smotkin, R.R. Díaz-Morales, Annu. Rev. Mater. Res. 33 (2003) 557.

[98] R.G. González-Huerta, J. a. Chávez-Carvayar, O. Solorza-Feria, J. Power Sources 153 (2006) 11.

[99] S.P. Jiang, Mater. Sci. Eng. A 418 (2006) 199.

[100] Z. Zhou, S. Wang, W. Zhou, G. Wang, L. Jiang, W. Li, S. Song, J. Liu, G. Sun, Q. Xin, Chem. Commun. (Camb). (2003) 394.

[101] Y. Wang, J. Ren, K. Deng, L. Gui, Y. Tang, Chem. Mater. (2000) 1622.

[102] V. Tzitzios, D. Niarchos, G. Margariti, J. Fidler, D. Petridis, Nanotechnology 16 (2005) 287.

[103] H. Oh, J. Oh, Y. Hong, H. Kim, Electrochim. Acta 52 (2007) 7278.

[104] C. Bock, C. Paquet, M. Couillard, G. a Botton, B.R. MacDougall, J. Am. Chem. Soc. 126 (2004) 8028.

[105] M. Darab, M. Thomassen, S. Sunde, ECS Trans. 41 (2011) 1067.

[106] M. Darab, J.L. Gomez de la Fuente, M.S. Thomassen, S. Sunde, ECS Trans. 50 (2012) 1353.

[107] D. Pletcher, R. Greff, R. Peat, L.M. Peter, Instrumental Methods in Electrochemistry, Woodhead Publishing, 2002.

[108] M.J. Watt-Smith, J.M. Friedrich, S.P. Rigby, T.R. Ralph, F.C. Walsh, J. Phys. D. Appl. Phys. 41 (2008) 174004.

[109] T. Vidaković, M. Christov, K. Sundmacher, Electrochim. Acta 52 (2007) 5606.

[110] B.M. Rush, J.A. Reimer, E.J. Cairns, J. Electrochem. Soc. 148 (2001) A137.

[111] H.L. (Editor) Jiujun Zhang (Editor), Electrocatalysis of Direct Methanol Fuel Cells, Wiley-VCH, 2009.

[112] X. Yuan, H. Wang, J. Colinsun, J. Zhang, Int. J. Hydrogen Energy 32 (2007) 4365.

[113] S. Asghari, A. Mokmeli, M. Samavati, Int. J. Hydrogen Energy 35 (2010) 9283.

[114] S. Zhang, X.-Z. Yuan, J.N.C. Hin, H. Wang, K.A. Friedrich, M. Schulze, J. Power Sources 194 (2009) 588.

[115] A.S. Arico', A. Stassi, E. Modica, R. Ornelas, I. Gatto, E. Passalacqua, V. Antonucci, ECS Trans. 3 (2006) 765.

[116] J. Xie, D.L. Wood, D.M. Wayne, T. a. Zawodzinski, P. Atanassov, R.L. Borup, J. Electrochem. Soc. 152 (2005) A104.

[117] M. Ciureanu, S.D. Mikhailenko, S. Kaliaguine, Catal. Today 82 (2003) 195.

[118] Y. Tang, J. Zhang, C. Song, H. Liu, J. Zhang, H. Wang, S. Mackinnon, T. Peckham, J. Li, S. McDermid, P. Kozak, J. Electrochem. Soc. 153 (2006) A2036.

[119] F. Jaouen, G. Lindbergh, K. Wiezell, J. Electrochem. Soc. 150 (2003) A1711.

[120] R.L. Sacci, D.A. Harrington, ECS Trans. 19 (2009) 31.

[121] J. Marie, R. Chenitz, M. Chatenet, S. Berthon-Fabry, N. Cornet, P. Achard, J. Power Sources 190 (2009) 423.

[122] M. Chatenet, L. Dubau, N. Job, F. Maillard, Catal. Today 156 (2010) 76.

[123] N. Job, M. Chatenet, S. Berthon-Fabry, S. Hermans, F. Maillard, J. Power Sources 240 (2013) 294.

[124] G. Hoogers, ed., Fuel Cell Technology Handbook, 6th ed., CRC Press, Washington, D.C., 2003.

[125] J. Zhang, PEM Fuel Cell Electrocatalysts and Catalyst Layers Fundamentals and Applications, Springer, London, 2008.

[126] V. Lordi, N. Yao, J. Wei, Chem. Mater. 13 (2001) 733.

[127] J. Guo, G. Sun, S. Shiguo, Y. Shiyou, Y. Weiqian, Q. Jing, Y. Yushan, X. Qin, J. Power Sources 168 (2007) 299.

[128] H.R.K. K. R. Cooper, Vijay Ramani, James M. Fenton, Experimental Methods and Data Analyses for Polymer Electrolyte Fuel Cells, Scribner Associates Inc., North Carolina, 2005.

[129] EG&G Technical Services Inc., Fuel Cell Handbook, 7th editio, U.S. Department of Energy, Morgantown, West Virginia, 2004.

[130] B.J. Greeley, J. Rossmeisl, A. Hellman, J.K. Nørskov, Zeitschrift Für Phys. Chemie 221 (2007) 1209.

[131] K.J.J. Mayrhofer, B.B. Blizanac, M. Arenz, V.R. Stamenkovic, P.N. Ross, N.M. Markovic, J. Phys. Chem. B 109 (2005) 14433.

[132] J.A. Ticianelli, C.R. Derouin, Engineering 251 (1988) 275.

[133] F.J. Vidal-Iglesias, R.M. Arán-Ais, J. Solla-Gullón, E. Herrero, J.M. Feliu, ACS Catal. 2 (2012) 901.

[134] A. López-Cudero, J. Solla-Gullón, E. Herrero, A. Aldaz, J.M. Feliu, J Electroanal. Chem. 644 (2010) 117.

[135] H.P. Bonzel, R. Ku, Surf. Sci. 33 (1972) 91.

[136] A. Dolev, J. Catal. 214 (2003) 146.

[137] J. Vacek, L. Havran, M. Fojta, Electroanalysis 21 (2009) 2139.

[138] J. Solla-Gullón, F.J. Vidal-Iglesias, E. Herrero, J.M. Feliu, A. Aldaz, Electrochem. Commun. 8 (2006) 189.

[139] L. Dsouza, L. Jiao, J. Regalbuto, J. Miller, a Kropf, J. Catal. 248 (2007) 165.

[140] J. Regalbuto, Preparation of Supported Metal Catalysts by Strong Electrostatic Adsorption (SEA), Handbook of Catalyst Preparation, Taylor & Francis, London, 2006.

[141] B.H. Liu, Z.P. Li, J. Power Sources 187 (2009) 527.

[142] N. Lakshmi, N. Rajalakshmi, K.S. Dhathathreyan, J. Phys. D. Appl. Phys. 39 (2006) 2785.

[143] J. Qi, L. Jiang, M. Jing, Q. Tang, G. Sun, Int. J. Hydrogen Energy 36 (2011) 10490.

[144] S.T. Briskeby, M. Tsypkin, S. Sunde, RSC Adv. (2014).

[145] V. Mehta, J.S. Cooper, J. Power Sources 114 (2003) 32.

[146] I. Bar-On, R. Kirchain, R. Roth, J. Power Sources 109 (2002) 71.

[147] S.K. Kamarudin, W.R.W. Daud, A. Md.Som, M.S. Takriff, A.W. Mohammad, J. Power Sources 157 (2006) 641.

[148] N. V. Aieta, P.K. Das, A. Perdue, G. Bender, A.M. Herring, A.Z. Weber, M.J. Ulsh, J. Power Sources 211 (2012) 4.

[149] A.J. Steinbach, M.K. Debe, J. Wong, M.J. Kurkowski, A.T. Haug, D.M. Peppin, S.K. Deppe, S.M. Hendricks, E.M. Fischer, ECS Trans. 33 (2010) 1179.

[150] A.J. Steinbach, M.K. Debe, M.J. Pejsa, D.M. Peppin, A.T. Haug, M.J. Kurkowski, S.M. Maier-Hendricks, ECS Trans. 41 (2011) 449.

[151] M. Pestrak, Y. Li, S.W. Case, D.A. Dillard, M.W. Ellis, Y.-H. Lai, C.S. Gittleman, J. Fuel Cell Sci. Technol. 7 (2010) 041009.

[152] S. Kundu, M.W. Fowler, L.C. Simon, S. Grot, J. Power Sources 157 (2006) 650.

[153] A.Z. Weber, J. Newman, J. Electrochem. Soc. 154 (2007) B405.

[154] A. Ohma, T. Mashio, K. Sato, H. Iden, Y. Ono, K. Sakai, K. Akizuki, S. Takaichi, K. Shinohara, Electrochim. Acta 56 (2011) 10832.

[155] M.S. Wilson, S. Gottesfeld, J. Appl. Electrochem. 22 (1992) 1.

[156] M.S. Wilson, J. Electrochem. Soc. 139 (1992) L28.

[157] D. Song, Q. Wang, Z. Liu, M. Eikerling, Z. Xie, T. Navessin, S. Holdcroft, Electrochim. Acta 50 (2005) 3347.

[158] M. Eikerling, A.A. Kornyshev, J. Electroanal. Chem. 453 (1998) 89.

[159] H. Dohle, K. Wippermann, J. Power Sources 135 (2004) 152.

[160] A. Abedini, B. Dabir, M. Kalbasi, Int. J. Hydrogen Energy 37 (2012) 8439.

[161] N. Khajeh-Hosseini-Dalasm, M.J. Kermani, D.G. Moghaddam, J.M. Stockie, Int. J. Hydrogen Energy 35 (2010) 2417.

[162] D. Song, Q. Wang, Z. Liu, T. Navessin, M. Eikerling, S. Holdcroft, J. Power Sources 126 (2004) 104.

[163] S. Obut, E. Alper, J. Power Sources 196 (2011) 1920.

[164] R.R. Passos, V.A. Paganin, E.A. Ticianelli, Electrochim. Acta 51 (2006) 5239.

[165] R.A. Silva, T. Hashimoto, G.E. Thompson, C.M. Rangel, Int. J. Hydrogen Energy 37 (2012) 7299.

[166] K. Kinoshita, Carbon: Electrochemical and Physicochemical Properties, Wiley-Blackwell, 1998.

[167] M.F. Mathias, R. Makharia, H.A. Gasteiger, J.J. Conley, T.J. Fuller, C.J. Gittleman, S.S. Kocha, D.P. Miller, C.K. Mittelsteadt, T. Xie, S.G. Yan, P.T. Yu, Electrochem. Soc. Interface 14 (2005) 24.

[168] J. Newman, C.W. Tobias, J. Electrochem. Soc. 109 (1962) 1183.

[169] J. Jiang, B. Yi, J. Electroanal. Chem. 577 (2005) 107.

[170] G. Cao, Y. Wang, Nanostructures and Nanomaterials: Synthesis, Properties and Applications, Imperial College Press, London, 2004.

[171] Z. Yang, S. Ball, D. Condit, M. Gummalla, J. Electrochem. Soc. 158 (2011) B1439.

[172] A. Lundblad, J. New Mater. Electrochem. Syst. 28 (2004) 21.

[173] W.S. Rasband, (n.d.).

[174] P. Ferreira-Aparicio, M.A. Folgado, L. Daza, J. Power Sources 192 (2009) 57.

[175] M. Watanabe, H. Sei, P. Stonehart, J. Electroanal. Chem. 261 (1989) 375.

[176] J. Newman, K.E. Thomas-Alyea, Electrochemical Systems, John Wiley & Sons, 2004.

[177] G.Ø. Lauvstad, R. Tunold, S. Sunde, J. Electrochem. Soc. 149 (2002) E497.

[178] A.M. Svensson, H. Weydahl, S. Sunde, Electrochim. Acta 53 (2008) 7483.

[179] M.L. Perry, J. Newman, E.J. Carins, J. Electrochem. Soc. 145 (1998) 5.

[180] L. Cindrella, A.M. Kannan, J.F. Lin, K. Saminathan, Y. Ho, C.W. Lin, J. Wertz, J. Power Sources 194 (2009) 146.

[181] J.P. Feser, A.K. Prasad, S.G. Advani, J. Power Sources 162 (2006) 1226.

[182] P.M. Wilde, M. Mändle, M. Murata, N. Berg, Fuel Cells 4 (2004) 180.

[183] A. Parthasarathy, S. Srinivasan, J.A. Appleby, C.R. Martin, J. Electrochem. Soc. 139 (1992) 2856.

[184] O.J. Murphy, S. Srinivasan, B.E. Conway, Electrochemistry in Transition, Plenum Press, 1992.

[185] A. Damjanovic, V. Brusic, Electrochim. Acta 12 (1967) 615.

[186] R. Makharia, M.F. Mathias, D.R. Baker, J. Electrochem. Soc. 152 (2005) A970.

[187] E.B. Easton, P.G. Pickup, Electrochim. Acta 50 (2005) 2469.

[188] a. P. Young, J. Stumper, E. Gyenge, J. Electrochem. Soc. 156 (2009) B913.

[189] S. Ge, X. Li, B. Yi, I.-M. Hsing, J. Electrochem. Soc. 152 (2005) A1149.

[190] J.H. Kim, Y. Yeon Jo, E.A. Cho, J.H. Jang, H.J. Kim, T.-H. Lim, I.-H. Oh, J.J. Ko, I.J. Son, J. Electrochem. Soc. 157 (2010) B633.

[191] R.L. Borup, J.R. Davey, F.H. Garzon, D.L. Wood, M. a. Inbody, J. Power Sources 163 (2006) 76.

[192] E. Santos, W. Schmickler, Catalysis in Electrochemistry: From Fundamental Aspects to Strategies for Fuel Cell Development, John Wiley and Sons, New Jersey, 2011.

[193] A. Wieckowski, J.K. Nørskov, Fuel Cell Science: Theory, Fundamentals, and Biocatalysis, John Wiley and Sons, New Jersey, 2010.

[194] W. Zhu, J.P. Zheng, R. Liang, B. Wang, C. Zhang, G. Au, E.J. Plichta, J. Electrochem. Soc. 156 (2009) B1099.

[195] J. Wang, G. Yin, Y. Shao, S. Zhang, Z. Wang, Y. Gao, J. Power Sources 171 (2007) 331.

[196] Z.-M. Zhou, Z.-G. Shao, X.-P. Qin, X.-G. Chen, Z.-D. Wei, B.-L. Yi, Int. J. Hydrogen Energy 35 (2010) 1719.

[197] F. Maillard, M. Eikerling, O. V. Cherstiouk, S. Schreier, E. Savinova, U. Stimming, Faraday Discuss. 125 (2004) 357.

[198] H. Chizawa, Y. Ogami, H. Naka, A. Matsunaga, N. Aoki, T. Aoki, ECS Trans. 3 (2006) 645.

[199] M. Cai, M.S. Ruthkosky, B. Merzougui, S. Swathirajan, M.P. Balogh, S.H. Oh, J. Power Sources 160 (2006) 977.

[200] F. Xu, R. Xu, S. Mu, Electrochim. Acta 112 (2013) 304.

[201] S.J. Andreasen, J.R. Vang, S.K. Kær, Int. J. Hydrogen Energy 36 (2011) 9815.

[202] H.S. Chu, C.P. Wang, W.C. Liao, W.M. Yan, J. Power Sources 159 (2006) 1071.

[203] H. Oetjen, V.M. Schmidt, U. Stimming, F. Trila, J. Electrochem. Soc. 143 (1996) 3838.

[204] J. Zhang, R. Datta, J. Electrochem. Soc. 149 (2002) A1423.

[205] J. Zhang, J.D. Fehribach, R. Datta, J. Electrochem. Soc. 151 (2004) A689.

[206] Z. Liu, L. Ma, J. Zhang, K. Hongsirikarn, J.G. Goodwin, Catal. Rev. 55 (2013) 255.

[207] H. Zhang, D. Yang, B. Li, Z. Qian, J. Ma, Int. J. Energy Res. 10 (2014) 277.

[208] H. Igarashi, T. Fujino, Y. Zhu, H. Uchida, M. Watanabe, Phys. Chem. Chem. Phys. 3 (2001) 306.

[209] P. Ochal, J.L. Gomez de la Fuente, M. Tsypkin, F. Seland, S. Sunde, N. Muthuswamy, M. Rønning, D. Chen, S. Garcia, S. Alayoglu, B. Eichhorn, J. Electroanal. Chem. 655 (2011) 140.

[210] Y.-J. Leng, X. Wang, I.-M. Hsing, J. Electroanal. Chem. 528 (2002) 145.

[211] M. Laurent-Brocq, N. Job, D. Eskenazi, J.-J. Pireaux, Appl. Catal. B Environ. 147 (2014) 453.

[212] H.A. Gasteiger, N.M. Markovic, P.N. Ross, J. Phys. Chem. 99 (1995) 8290.

[213] H.A. Gasteiger, N.M. Markovic, P.N. Ross, J. Phys. Chem. 99 (1995) 16757.

[214] T.E. Springer, T. Rockward, T. a. Zawodzinski, S. Gottesfeld, J. Electrochem. Soc. 148 (2001) A11.

[215] Y. Barshad, X. Zhou, E. Gulari, J. Catal. 94 (1985) 128.

[216] W. Vielstich, A. Lamm, H.A. Gasteiger, Handbook of Fuel Cells: Fundamentals, Technology, and Applications, Volume 2: Fuel Cell Electrocatalysis, Wiley, New Jersey, 2003.

[217] J. Healy, C. Hayden, T. Xie, K. Olson, R. Waldo, M. Brundage, H. Gasteiger, J. Abbott, Fuel Cells 5 (2005) 302.

[218] J. Zhang, G.J. Offer, Platin. Met. Rev. 53 (2009) 219.

[219] Z. Nagy, H. You, Electrochim. Acta 47 (2002) 3037.

[220] H.L. Lin, Y.S. Hsieh, C.W. Chiu, T.L. Yu, L.C. Chen, J. Power Sources 193 (2009) 170.

[221] X. Yuan, C. Song, H. Wang, J. Zhang, Electrochemical Impedance Spectroscopy in PEM Fuel Cells, Springer, New York, 2011.

[222] M.E. Orazem, B. Tribollet, Electrochemical Impedance Spectroscopy, John Wiley and Sons, New Jersey, 2008.

[223] J.R. Macdonald, Impedance Spectroscopy: Emphasizing Solid Materials and Systems, John Wiley and Sons, New York, 1987.

[224] G.Ø. Lauvstad, R. Tunold, S. Sunde, J. Electrochem. Soc. 149 (2002) E506.

[225] J.T. Müller, P.M. Urban, W.F. Hölderich, J. Power Sources 84 (1999) 157.

[226] J.T. Müller, P.M. Urban, J. Power Sources 75 (1998) 139.

[227] F.S. Saleh, E.B. Easton, J. Electrochem. Soc. 159 (2012) B546.

[228] J. Kang, J. Kim, Int. J. Hydrogen Energy 35 (2010) 13125.

[229] R. Lin, B. Li, Y.P. Hou, J.M. Ma, Int. J. Hydrogen Energy 34 (2009) 2369.

[230] R. Escudero-Cid, P. Hernández-Fernández, J.C. Pérez-Flores, S. Rojas, S. Garcia-Rodríguez, E. Fatás, P. Ocón, Int. J. Hydrogen Energy 37 (2012) 7119.

[231] M.K. Jeon, J.Y. Won, K.S. Oh, K.R. Lee, S.I. Woo, Electrochim. Acta 53 (2007) 447.

[232] J. Hu, H. Zhang, Y. Zhai, G. Liu, B. Yi, Int. J. Hydrogen Energy 31 (2006) 1855.

[233] A. Marcu, G. Toth, S. Kundu, L.C. Colmenares, R.J. Behm, J. Power Sources 215 (2012) 266.

[234] H.N. Dinh, X. Ren, F.H. Garzon, S. Gottesfeld, J. Electroanal. Chem. 491 (2000) 222.

[235] E. Barsoukov, J.R. Macdonald, Impedance Spectroscopy: Theory, Experiment, and Applications, Wiley-Interscience, Hoboken, New Jersey, 2005.

[236] Z. Nagy, H. You, Phys. B 198 (1994) 187.

[237] J.M. Feliu, E. Herrero, V. Climent, Electrocatalytic Properties of Stepped Surfaces, in Catalysis in Electrochemistry: From Fundamentals to Strategies for Fuel Cell Development, John Wiley & Sons, Hoboken, New Jersey, 2011.

[238] K. Kinoshita, Electrochemical Oxygen Technology, The Electrochemical Society Series, John Wiley & Sons, New York, 1992.